

# Automotive exhaust gas conversion : reaction kinetics, reactor modelling and control

**Citation for published version (APA):**

Nievergeld, A. J. L. (1998). *Automotive exhaust gas conversion : reaction kinetics, reactor modelling and control*. [Phd Thesis 1 (Research TU/e / Graduation TU/e), Chemical Engineering and Chemistry]. Technische Universiteit Eindhoven. <https://doi.org/10.6100/IR506187>

**DOI:**

[10.6100/IR506187](https://doi.org/10.6100/IR506187)

**Document status and date:**

Published: 01/01/1998

**Document Version:**

Publisher's PDF, also known as Version of Record (includes final page, issue and volume numbers)

**Please check the document version of this publication:**

- A submitted manuscript is the version of the article upon submission and before peer-review. There can be important differences between the submitted version and the official published version of record. People interested in the research are advised to contact the author for the final version of the publication, or visit the DOI to the publisher's website.
- The final author version and the galley proof are versions of the publication after peer review.
- The final published version features the final layout of the paper including the volume, issue and page numbers.

[Link to publication](#)

**General rights**

Copyright and moral rights for the publications made accessible in the public portal are retained by the authors and/or other copyright owners and it is a condition of accessing publications that users recognise and abide by the legal requirements associated with these rights.

- Users may download and print one copy of any publication from the public portal for the purpose of private study or research.
- You may not further distribute the material or use it for any profit-making activity or commercial gain
- You may freely distribute the URL identifying the publication in the public portal.

If the publication is distributed under the terms of Article 25fa of the Dutch Copyright Act, indicated by the "Taverne" license above, please follow below link for the End User Agreement:

[www.tue.nl/taverne](http://www.tue.nl/taverne)

**Take down policy**

If you believe that this document breaches copyright please contact us at:

[openaccess@tue.nl](mailto:openaccess@tue.nl)

providing details and we will investigate your claim.



# **Automotive Exhaust Gas Conversion:**

**Reaction Kinetics, Reactor  
Modelling and Control**

**Arthur Nievergeld**

# **Automotive Exhaust Gas Conversion: Reaction Kinetics, Reactor Modelling and Control**

**PROEFSCHRIFT**

ter verkrijging van de graad van doctor aan de  
Technische Universiteit Eindhoven, op gezag van  
de Rector Magnificus, prof.dr. M. Rem, voor een  
commissie aangewezen door het College voor  
Promoties in het openbaar te verdedigen op  
vrijdag 13 februari 1998 om 16.00 uur

door

**Arthur Josephus Laurentius Nievergeld**

geboren te Kelpen

Dit proefschrift is goedgekeurd door de promotoren:

prof.dr.ir. G.B. Marin

en

prof.dr.ir. A.C.P.M. Backx

Copromotor:

dr.ir. J.H.B.J. Hoebink

**CIP-DATA LIBRARY TECHNISCHE UNIVERSITEIT EINDHOVEN**

Nievergeld, Arthur J.L.

Automotive exhaust gas conversion: Reaction kinetics, reactor modelling  
and control / by Arthur J.L. Nievergeld. -

Eindhoven: Technische Universiteit Eindhoven, 1998.

Proefschrift. -

ISBN 90-386-0728-8

NUGI 813

Trefw.: uitlaatgassen; reductie / chemische reactoren / procesregeling

Subject headings: three-way catalysts / reaction kinetics / process control

Druk: Universiteitsdrukkerij

Technische Universiteit Eindhoven

---

## SUMMARY

To reduce the emissions of automotive engines, usually a so-called monolith converter, *i.e.* a ceramic block with several thousands of parallel channels, is mounted in the exhaust pipe of a car. The walls of the channels are coated with the washcoat: a thin layer of alumina which serves as support for the noble metal particles, *e.g.* platinum and rhodium, being the active catalyst phase. To allow high conversions of all harmful components simultaneously, the exhaust gas composition is kept close to the stoichiometric point by a feedback control system. The delay time in the feedback loop of the controller results in an oscillating feed composition. The effects of these oscillations on the time-average conversions can be either positive, neutral or negative.

The application of a so-called frequency response analysis aimed at the determination of kinetic parameters in continuous flow reactors has been investigated. A frequency response analysis determines the dynamic behaviour of the reactor as a function of the oscillating frequency and extracts information from the responses about the kinetic parameters to be estimated. From the analysis it is clear that dynamic operation reveals more information about the reaction mechanism and the kinetic parameters than steady state operation. Applying the frequency response analysis to a reaction described by a three-step mechanism consisting of adsorption/desorption and surface reaction in a plug flow reactor results in kinetic information about all kinetic parameters, whereas the responses of a CSTR contain information about the rate determining step and the sorption equilibrium coefficient only. Compared with the plug flow reactor, the dynamic behaviour of the CSTR is a result of both mixing in the fluid phase and the kinetics. When mixing has an important contribution to the dynamic behaviour of the CSTR the responses will contain less kinetic information than the responses of the plug flow reactor.

The CO oxidation by oxygen over both a Pt/ $\gamma$ -Al<sub>2</sub>O<sub>3</sub> and a commercial Pt/Rh/CeO<sub>2</sub>/ $\gamma$ -Al<sub>2</sub>O<sub>3</sub> catalyst was studied in a laboratory fixed-bed reactor with cycling of the feed under typical exhaust gas conditions below the light-off temperature. An elementary step reaction mechanism for the CO oxidation over Pt/ $\gamma$ -Al<sub>2</sub>O<sub>3</sub> was developed to describe the responses resulted from switching between a CO containing

and an oxygen containing feed stream. The kinetic parameters of the mechanism were estimated by means of nonlinear regression. Experiments over  $\text{Pt/Rh/CeO}_2/\gamma\text{-Al}_2\text{O}_3$  were performed to clarify the role of ceria during cyclic feeding of CO and  $\text{O}_2$ . The effects of steam and  $\text{CO}_2$  on the CO oxidation in the presence of ceria have also been addressed.

The cyclic feeding experiments over the  $\text{Pt}/\gamma\text{-Al}_2\text{O}_3$  catalyst showed a strong temperature dependence of the oxygen adsorption and that adsorption is inhibited by adsorbed CO. In contrast, CO adsorption is independent of the temperature and takes place on a catalytic surface completely covered with oxygen adatoms. Furthermore,  $\text{CO}_2$  adsorbs significantly on the  $\gamma\text{-Al}_2\text{O}_3$  support. The experimental responses can be adequately described by an elementary step reaction mechanism consisting of adsorption and desorption of CO, and molecular oxygen adsorption followed by instantaneous dissociation and subsequent reaction with CO. To account for CO adsorption on an oxygen covered surface it is assumed that CO and oxygen can share the same catalytic site, whereas the reaction between CO and oxygen adatoms sharing the same site leads to a second route for  $\text{CO}_2$  formation. Interaction of gas phase  $\text{CO}_2$  and the support is assumed to proceed via reversible adsorption of  $\text{CO}_2$ .

Cyclic feeding experiments over a  $\text{Pt/Rh/CeO}_2/\gamma\text{-Al}_2\text{O}_3$  catalyst showed the existence of a reaction path leading to  $\text{CO}_2$  apart from the monofunctional paths over  $\text{Pt}/\gamma\text{-Al}_2\text{O}_3$ . This so-called bifunctional path describes the reaction of CO adsorbed on the noble metal with oxygen on the ceria surface. From the experiments it is clear that oxygen from the gas phase adsorbs on ceria and diffuses to the noble metal interface where reaction with adsorbed CO takes place. The relative importance of each reaction path to the total  $\text{CO}_2$  production depends on the temperature. At elevated temperatures ( $T > 453\text{ K}$ ) oxygen in the bulk of ceria participates in the reaction with adsorbed CO. During the CO containing feed stream oxygen in the bulk of ceria diffuses to the ceria surface where it reacts with CO at the metal-ceria interface, whereas the reduced bulk is oxidized when the feed stream contains  $\text{O}_2$  only. Ceria acts then as a storage component that releases oxygen under net reducing conditions and is filled up with oxygen under net oxidizing conditions. Steam was found to enhance the  $\text{CO}_2$  formation rate, while the presence of  $\text{CO}_2$  in the feed stream leads to lower reaction rates by blocking adsorption sites for oxygen on ceria. The latter leads to a less pronounced effect of ceria on the  $\text{CO}_2$  production rate. The contribution of the bifunctional path to the  $\text{CO}_2$  formation results in higher time average conversions during cyclic feeding of CO and  $\text{O}_2$ .

An adiabatic, one-dimensional model of a catalytic converter of automotive exhaust gas based on first principles was developed in order to simulate the behaviour of monolithic converters under cycling and start-up conditions. Accumulation of mass in the bulk gas phase, the gas phase in the pores of the washcoat and on the catalyst surface, as well as accumulation of energy in both the gas phase and the solid phase are taken into account. Both the oxidation of CO, of ethene and ethyne and the

reduction of NO have been considered in the modelling. Steady state simulations showed that the pollutants in exhaust gas are converted in the reactor in a fixed sequence and that the light-off temperature of individual pollutants is rather irrelevant for the behaviour of real exhaust gas because of mutual interactions in a mixture. First ethyne is converted, then carbon monoxide, and finally nitrogen oxide and ethene simultaneously. Forced concentration cycling can either improve or deteriorate the performance of the converter when compared to steady state operation, and the effects are strongly influenced by the conditions. Below the light-off temperature the conversion improvement of CO, C<sub>2</sub>H<sub>4</sub> and C<sub>2</sub>H<sub>2</sub> increases with increasing temperature. Above the light-off temperature time-average conversions are lower than steady state ones. Steady state reactor operation at the stoichiometric point leads then to the highest performance. Light-off calculations with a time independent feed composition showed that it takes more than 100 seconds to warm-up the reactor completely, but after 50 seconds conversion of all components is already completed. The warming-up period of the reactor is mainly determined by convective heat transfer.

A combustion engine model, based on literature data, and the model of the converter were used in designing a so-called model predictive control strategy for exhaust gas converter. Therefore, a black box model of the converter in combination with the engine was developed using identification techniques. The controller uses the black box model to predict the emissions over a given time horizon which allows a very tight control of the air-to-fuel ratio fed to the engine. This in contrast to the currently applied controller which causes the air-to-fuel ratio to oscillate around the stoichiometric point. The black-box model was also used to calculate the optimal setpoints of the controller during a cold-start. Switching the air-to-fuel ratio to lean for a short period of time leads to a reduction of the emissions of the pollutants due to a simultaneous ignition of the oxidation reactions.





---

## SAMENVATTING

De uitstoot van schadelijke stoffen in het uitlaatgas van Otto motoren wordt tegenwoordig beperkt door de toepassing van een driewegkatalysator. Een driewegkatalysator is gemonteerd in de uitlaatpijp van de auto en bestaat uit keramisch materiaal met verschillende duizenden parallelle kanalen, de zogenaamde monoliet. De wanden van deze kanalen zijn bedekt met een zogenaamde 'washcoat', een dun laagje alumina dat dient als drager voor het edelmetaal, zoals platina en rhodium. Een hoge conversie van alle schadelijke componenten wordt bereikt wanneer de uitlaatgassamenstelling stoichiometrisch is. Daartoe is de motor uitgerust met een regelsysteem dat de samenstelling dicht bij de optimale waarde probeert te houden. Echter, een dode tijd in de terugkoppellus van de regelaar zorgt voor oscillaties in de uitlaatgassamenstelling. Het is alom bekend dat deze oscillaties de prestatie van de reactor kunnen beïnvloeden.

Het bewust opwekken van een oscillerende gassamenstelling kan ook voordelig zijn bij het schatten van kinetische parameters. In dit kader is de toepasbaarheid van een zogenaamde frequentie responsie analyse bij het schatten van kinetische parameters in continue doorstroomde reactoren onderzocht. Tijdens zo'n analyse worden de amplitude en fase van de concentraties stroomafwaarts van de reactor gemeten als functie van de frequentie terwijl de voedingsconcentraties harmonisch oscilleren. Het frequentiegedrag van de amplitude en fase hangt af van de procescondities, en van de kinetische parameters en het reactiemechanisme. Om de voordelen van dynamisch bedrijven van reactoren vergeleken met stationair bedrijf tijdens kinetisch onderzoek duidelijk te maken is het dynamisch gedrag van een propstroomreactor en een continue doorstroomde reactor (CSTR) bepaald voor een reactie die kan worden beschreven door een driestappenmechanisme. In de CSTR kan alleen de evenwichtsconstante en de snelheidscoëfficiënt van de snelheidsbepalende stap worden geschat, terwijl in de propstroomreactor alle coëfficiënten kunnen worden bepaald. De kinetische informatie die beschikbaar is aan de uitlaat van de CSTR wordt gemaskeerd door menging in de gasfase. Wanneer de tijdconstante van menging veel groter is dan de karakteristieke tijdschaal van de elementaire stappen dan bevatten de responsies weinig kinetische

informatie.

De reactie tussen CO en zuurstof over een Pt/ $\gamma$ - $\text{Al}_2\text{O}_3$  en een commercieel verkrijgbare Pt/Rh/ $\text{CeO}_2$ / $\gamma$ - $\text{Al}_2\text{O}_3$  katalysator is bestudeerd in een laboratorium vast-bedreactor door gebruik te maken van een oscillerende voedingssamenstelling. De condities waren zodanig gekozen dat het reactorbedrijf vergelijkbaar was met uitlaatgascondities gedurende een koude start. Aan de hand van de responsies als gevolg van het schakelen tussen een voedingsstroom die alleen CO in helium bevat en een die  $\text{O}_2$  in helium bevat is een reactiemechanisme voor de CO oxidatie over de Pt/ $\gamma$ - $\text{Al}_2\text{O}_3$  katalysator opgesteld. De snelheidscoëfficiënten in het mechanisme zijn geschat met behulp van niet-lineaire regressietechnieken. Belangrijkste doel van de experimenten met de commerciële Pt/Rh/ $\text{CeO}_2$ / $\gamma$ - $\text{Al}_2\text{O}_3$  katalysator was het onderzoeken van de rol van ceria tijdens oscillerende condities en de invloed van stoom en  $\text{CO}_2$  in de voeding op de CO oxidatie.

Experimenten met de Pt/ $\gamma$ - $\text{Al}_2\text{O}_3$  katalysator tonen dat zuurstofadsorptie sterk afhankelijk is van de temperatuur en wordt geïnhibeed door geadsorbeerd CO, terwijl CO adsorbeert op een met zuurstof bedekt katalysatoroppervlak en temperatuur onafhankelijk is. Uit de  $\text{CO}_2$  responsie kan worden afgeleid dat er significante  $\text{CO}_2$  adsorptie op de alumina drager plaatsvindt. De responsies kunnen worden beschreven door een elementair stappenmodel bestaande uit adsorptie en desorptie van CO, moleculaire zuurstofadsorptie die wordt gevolgd door instantane dissociatie en oppervlakreactie die leidt tot  $\text{CO}_2$  vorming. De adsorptie van CO op een door zuurstof bedekt katalysatoroppervlak kan worden beschreven door aan te nemen dat zuurstof en CO hetzelfde actieve centrum kunnen bezetten. De reactie tussen deze twee species vormt een tweede reactiepad voor de  $\text{CO}_2$  vorming. De interactie tussen  $\text{CO}_2$  en de alumina drager is gemodelleerd door reversibele adsorptie.

De experimenten met de commercieel verkrijgbare Pt/Rh/ $\text{CeO}_2$ / $\gamma$ - $\text{Al}_2\text{O}_3$  katalysator maken duidelijk dat naast de twee reactiepaden over het edelmetaal, de zogenaamde monofunctionele paden, ook nog een zogenaamd bifunctioneel pad bestaat voor de  $\text{CO}_2$  productie. Dit laatste pad wordt gevormd door de reactie tussen op het edelmetaal geadsorbeerd CO en zuurstofspecies op het ceriaoppervlak. Zuurstof uit de gasfase adsorbeert op het ceriaoppervlak en diffundeert naar het edelmetaal-ceria grensvlak waar reactie met CO species plaatsvindt. Bij een lage temperatuur vindt de aanvoer van zuurstof voornamelijk plaats via oppervlakdiffusie, terwijl bij hogere temperaturen diffusie vanuit de bulk van het ceria een steeds belangrijkere rol gaat spelen. Het ceriaoppervlak en de ceriabulk gedragen zich als zuurstofcapaciteiten die kunnen worden aangesproken tijdens reducerende omstandigheden terwijl zij gedurende oxiderende procescondities worden gevuld. Dit resulteert in een  $\text{CO}_2$  productie tijdens het gedeelte van de periode dat er alleen CO wordt gevoed. Stoom in de voeding bleek de productiesnelheid van  $\text{CO}_2$  te verhogen, terwijl een voeding met 10 vol%  $\text{CO}_2$  leidt tot een verlaging van de productiesnelheid. Doordat  $\text{CO}_2$  op het ceria adsorbeert wordt de bijdrage van het bifunctionele pad in de  $\text{CO}_2$  productie kleiner en

het gedrag van de  $\text{Pt}/\gamma\text{-Al}_2\text{O}_3$  katalysator benaderd. De aanwezigheid van het bifunctionele pad leidt tot een hogere tijdsgemiddelde prestatie van de commerciële katalysator vergeleken met de  $\text{Pt}/\gamma\text{-Al}_2\text{O}_3$  katalysator.

Om de effecten van een oscillerende voedingssamenstelling op de prestatie van een industriële uitlaatgaskatalysator te bestuderen is een dynamisch model van de katalysator opgesteld. Dit model bestond uit continuïteitsvergelijkingen voor de componenten in de bulkgasfase, de poriën van de 'washcoat' en species op het edelmetaaloppervlak. Verder bestond het model ook nog uit energievergelijkingen voor de gasfase en voor de vaste fase. De oxidatie van de CO, etheen en ethyn en de reductie van NO werden in de modellering in beschouwing genomen. Simulaties toonden dat tijdens stationair bedrijf de schadelijke componenten in een vaste volgorde als functie van de reactorcoördinaat worden omgezet: eerst reageert ethyn, dan CO en daarna NO en etheen tegelijk. Het is duidelijk dat door de wederzijdse beïnvloeding van de componenten het gedrag van een monolietreactor onder echte condities alleen kan worden benaderd indien tijdens de simulaties het uitlaatgas een realistische samenstelling heeft. De effecten van een oscillerende voedingssamenstelling op de prestatie van de reactor zijn afhankelijk van de temperatuur. Beneden de zogenaamde 'light-off' temperatuur leidt oscillerend voeden tot een verhoging van de conversies van CO, etheen en ethyn vergeleken met stationair bedrijf. Boven de 'light-off' temperatuur leidt een constante stoichiometrische voedingssamenstelling tot de hoogste prestatie. Simulatie van een koude start maakte duidelijk dat het ongeveer 100 seconden duurt voordat de reactor helemaal is opgewarmd, maar na 50 seconden is de omzetting van alle componenten volledig. Uit de berekeningen bleek ook dat de opwarming van de monolietreactor voornamelijk plaatsvindt door convectie.

Het model van de monolietreactor is samen met een model voor de motor uit de literatuur gebruikt om een zogenaamde modelgebaseerde regelaar te ontwikkelen. Het interne model van de regelaar is bepaald met behulp van identificatietechnieken. Door gebruik te maken van transformaties kan ondanks het niet-lineaire procesgedrag toch een lineaire regelaar worden gebruikt. Met behulp van het interne model kan de regelaar het gedrag van de motor en reactor voorspellen en de optimale voedingssamenstelling van de motor berekenen zodat de concentraties stroomafwaarts van de reactor de gewenste waarden aannemen. Dit in tegenstelling tot de huidige toegepaste regelaar die oscillaties in de uitlaatgassamenstelling rond de gewenste waarde veroorzaakt. Het model van de regelaar is ook gebruikt om de optimale stationaire waarde van de lucht-brandstofverhouding te berekenen gedurende een koude start. Uit de berekende lucht-brandstofverhouding volgde dat een oxiderende voedingssamenstelling van de reactor op het juiste moment en gedurende korte tijd leidt tot een verlaging van de uitstoot van schadelijke stoffen.



---

## **CONTENTS**

<b>SUMMARY/SAMENVATTING</b>	<b>3</b>
<b>NOTATION</b>	<b>15</b>
<b>1 INTRODUCTION</b>	<b>19</b>
<b>2 EXPERIMENTAL SET-UP AND PROCEDURES</b>	
2.1 Introduction	25
2.2 Experimental set-up	26
2.2.1 Feed section	26
2.2.2 Reactor section	27
2.2.3 Analysis section	28
2.3 Catalyst preparation and characterization	29
2.4 Experimental procedures	30
2.4.1 Catalyst pretreatment and stabilization	30
2.4.2 Calibration of the mass spectrometer	32
2.4.3 Cycling of argon concentrations	33
2.4.4 Inlet concentrations	34
2.4.5 Smoothing of the experimental data	34
<b>3 FREQUENCY RESPONSE ANALYSIS AIMED AT DETERMINATION OF KINETIC PARAMETERS</b>	
3.1 Introduction	37
3.2 Definitions	39
3.3 Adsorption and desorption in continuous flow reactors	41
3.3.1 Introduction	41
3.3.2 Adsorption-desorption in a CSTR	42

3.3.3 Adsorption-desorption in a plug flow reactor	44
3.3.4 Dynamics of a CSTR versus a plug flow reactor	45
3.3.5 Parameter sensitivity analysis	47
3.4 Three-step mechanism in continuous flow reactors	48
3.4.1 Kinetic model	48
3.4.2 Three-step mechanism in a CSTR	50
3.4.3 Three-step mechanism in a plug flow reactor	53
3.4.4 Parameter sensitivity analysis	56
3.5 Conclusions	59
Appendix 3A Derivation of the frequency response equations for adsorption and desorption in continuous flow reactors	62
Appendix 3B Derivation of the frequency response equations for the three step mechanism in continuous flow reactors	66
4 TRANSIENT KINETICS OF THE CO OXIDATION OVER Pt/ $\gamma$ -Al <sub>2</sub> O <sub>3</sub>	
4.1 Introduction	69
4.2 Model equations and data analysis	71
4.2.1 Reactor modelling	71
4.2.2 Estimation of kinetic parameters	73
4.3 Experimental results	75
4.3.1 Experimental conditions	75
4.3.2 Cyclic feeding	76
4.3.3 Effect of frequency and temperature on the time-average conversion	79
4.4 Kinetic model	81
4.4.1 Reaction mechanism	81
4.4.2 Rate expressions	86
4.5 Regression results	87
4.5.1 Parameter estimates	87
4.5.2 Simulations	88
4.6 Steady state simulations	90
4.7 Conclusions	91
5 TRANSIENT KINETICS OF THE CO OXIDATION OVER Pt/Rh/CeO <sub>2</sub> / $\gamma$ -Al <sub>2</sub> O <sub>3</sub>	
5.1 Introduction	95
5.2 Experimental results and discussion	96
5.2.1 Experimental conditions	96
5.2.2 Cyclic feeding experiments with CO and O <sub>2</sub>	97

## CONTENTS

	13
5.2.3 Effect of CO <sub>2</sub> and H <sub>2</sub> O	104
5.2.4 Effects of cerium oxide on the time-average conversion	106
5.3 Reaction mechanism	109
5.4 Conclusions	110
 6 SIMULATION OF AN AUTOMOTIVE EXHAUST GAS CONVERTER	
6.1 Introduction	113
6.2 Kinetic model	114
6.2.1 Reaction mechanism	114
6.2.2 Rate equations	116
6.3 Reactor model	118
6.3.1 Assumptions	118
6.3.2 Continuity equations	120
6.4 Results and discussion	123
6.4.1 Steady state	123
6.4.2 Light-off behaviour	125
6.4.3 Cyclic feeding	126
6.4.4 Effects of cyclic feeding on the time-average conversions	128
6.5 Conclusions	131
 Appendix 6A      Calculation of physical coefficients	135
 7 MODEL PREDICTIVE CONTROL OF THE AUTOMOTIVE EXHAUST GAS CONVERTER	
7.1 Introduction	137
7.2 Model predictive control	138
7.3 Identification procedure	142
7.4 Description of the process	143
7.5 Identification results	145
7.5.1 Preliminary analysis	145
7.5.2 Nonlinear transformations	149
7.5.3 Model estimation and validation	154
7.6 Controller design and performance	154
7.6.1 PI controller	155
7.6.2 Model predictive controller	156
7.6.3 Comparison between the PI controller and the MPC	157
7.6.4 Effects of model error on the performance of the MPC	158
7.7 Steady state optimizer	159

7.8 Conclusions	160
8 GENERAL CONCLUSIONS	163



## NOTATION

$a_{cat}$	specific catalytic surface	$m_{NM}^2 m_R^{-3}$
$a_s$	specific surface area	$m_c^2 kg_c^{-1}$
$a_v$	specific surface area per volume	$m_i^2 m_R^{-3}$
$A$	pre-exponential factor	$s^{-1}$
$A_s$	cross sectional surface area	$m_R^2$
$b$	catalyst dilution degree	$m_{inert}^3 m_{inert+c}^{-3}$
$\mathbf{b}$	vector of parameter estimates	-
$B$	fractional amplitude	-
$c_p$	specific heat	$J kg^{-1} K^{-1}$
$C$	concentration	$mol m^{-3}$
$d$	diameter	$m$
$d_b$	diameter monolith channel	$m_R$
$d_w$	washcoat thickness	$m_R$
$D$	diffusion coefficient	$m_g^3 m_g^{-1} s^{-1}$
$e$	error	situation dependent
$E$	activation energy	$kJ mol^{-1}$
$f$	frequency	Hz
$\mathbf{f}$	vector with model equations	
$F$	molar flow rate	$mol s^{-1}$
$FE$	fraction of exposed metal atoms	$mol_s mol^{-1}$
$G$	mass flow	$kg s^{-1}$
$\Delta_r H$	reaction enthalpy	$J mol^{-1}$
$k$	rate coefficient	situation dependent
$k_i$	mass transfer coefficient	$m_i^3 m_i^{-2} s^{-1}$
$K_p$	proportional gain	situation dependent
$L_R$	reactor length	$m_R$
$L_i$	total concentration of surface sites	$mol m_{NM}^{-2}$
$m$	number of parameters	-
$m$	number or control moves	-

$M$	molar mass	$\text{kg mol}^{-1}$
$n$	number of observations	-
$N$	turnover frequency	$\text{s}^{-1}$
$Nu$	Nusselt number	-
$p$	pressure	Pa
$p$	prediction horizon	-
$q$	number of observed responses	-
$r$	reaction rate	$\text{mol m}^{-2}_{\text{NM}} \text{s}^{-1}$
$R$	gas constant	$\text{J mol}^{-1} \text{K}^{-1}$
$R$	production rate	$\text{mol m}^{-2}_{\text{NM}} \text{s}^{-1}$
$S$	objective function	-
$Sh$	Sherwood number	-
$s^0$	sticking probability on clean surface	-
$t$	time	s
$T$	temperature	K
$T_s$	sampling period	s
$u$	manipulated variable	situation dependent
$w$	catalyst metal loading	$\text{kg}_{\text{metal}} \text{kg}^{-1}_c$
$w$	weights	-
$W$	catalyst mass	$\text{kg}_c$
$x$	axial reactor coordinate	$m_R$
$x$	vector of independent variables	-
$y$	vector with observations	-
$y$	output	situation dependent
*	vacant noble metal surface site	-
‡	vacant site on support	-
□	vacant site on ceria	-

### Greek symbols

$\alpha$	heat transfer coefficient	$\text{W m}^{-2} \text{K}^{-1}$
$\beta$	coefficient of surface dependency	$\text{J mol}^{-1}$
$\beta$	vector of parameters	-
$\varepsilon$	monolith converter void fraction	$\text{m}^3_t \text{m}^{-3}_R$
$\varepsilon_b$	catalyst bed void fraction	$\text{m}^3_t \text{m}^{-3}_R$
$\varepsilon_w$	washcoat porosity	$\text{m}^3_t \text{m}^{-3}_w$
$\theta$	fractional surface coverage	-
$\lambda$	thermal conductivity	$\text{W m}^{-1} \text{K}^{-1}$
$\lambda$	equivalence ratio $(A/F)/(A/F)_{\text{stoch}}$	-

$\nu$	stoichiometric coefficient	-
$\xi$	fractional surface coverage	-
$\rho$	density	$\text{kg m}^{-3}$
$\sigma$	stoichiometric coefficient	-
$\tau$	characteristic time	s
$\tau_i$	integration time	s
$\phi$	phase	rad
$\phi_m^{\text{sup}}$	superficial mass flow	$\text{kg m}^{-2} \text{ s}^{-1}$
$\omega$	angular frequency	$\text{rad s}^{-1}$

### Subscripts

a	adsorption
b	bulk; catalyst bed
c	catalyst, characteristic
d	desorption
diss	dissociation
f	bulk gas phase; feed
i	with respect to component i; inner
LH	Langmuir-Hinshelwood
m	modulation; model
NM	noble metal
R	reactor
s	surface; solid; superficial; setpoint
stoich	stoichiometric
tot	total
w	specific; reactor wall

### Superscripts

0	static; standard; under reference conditions
in	inlet; input
out	output; outlet
ss	steady-state



# 1

---

## INTRODUCTION

The catalytic treatment of automotive exhaust gas was introduced in the seventies in the USA and has become an important industrial process today. During the last two decades the more stringent emission standards resulted in a 90% reduction of the emissions of hydrocarbons, CO and NO<sub>x</sub> by passenger cars. However, the latest Clean Air Act provisions, leading via the Transitional Low Emission Vehicles (TLEV) to Ultra Low Emissions Vehicles (ULEV), force car and catalyst manufactures towards new technologies (Ball and Jacque, 1994). Much effort has been put in the search for alternative fuels such as methanol and propane, and the development of new engine technologies. Hybrid drive systems, *i.e.* a combination of a combustion engine and an electric machine, are becoming an important field of attention in the challenge to approach Zero Emission Vehicles (ZEV) (Tagliaferri *et al.*, 1994).

Until 1975, the emissions of CO and hydrocarbons were reduced by slightly lean operation of the engine. To meet the emission standards of NO<sub>x</sub> the combustion temperature was reduced by exhaust gas recirculation (EGR) but this measure lead to higher fuel consumption and was abandoned after the oil crisis. The more stringent standards for CO and hydrocarbons introduced in 1975, see Figure 1.1, lead to the application of the oxidation catalyst. In 1979, Volvo was the first to introduce cars with a fuel control system in combination with a three-way catalyst, and this is nowadays the only system to be applied for automotive exhaust gas treatment.

To meet the future stricter vehicle emission regulations, see Figure 1.1, car manufacturers evaluate various strategies to significantly reduce the emissions, especially those of hydrocarbon and NO<sub>x</sub>. One of the main goals of these new technologies is to reduce the time to reach the so-called light-off temperature, which is the temperature required for 50% conversion of the pollutants, as most of the emissions

occur before the catalyst has reached the light-off temperature (Rijkeboer, 1991). It takes about one minute after a cold start of the engine to reach this temperature (Kirchner and Eigenberg, 1996). A strategy to reduce the light-off period is fitting cars with electrically heated pre-converters (Oh *et al.*, 1993; Kirchner and Eigenberg, 1996; Kirchner *et al.*, 1997). The drawbacks of this system are the high costs and the high weight, as the battery to store the energy required for heating the pre-converter is very large. A second option is the installation of a small properly designed pre-converter located upstream of the three-way catalyst typically 0.6 m from the exhaust manifold (Gulati *et al.*, 1994). Major drawback of this system is the long-term thermal degradation of the pre-converter due to the high exhaust gas temperature close to the engine.

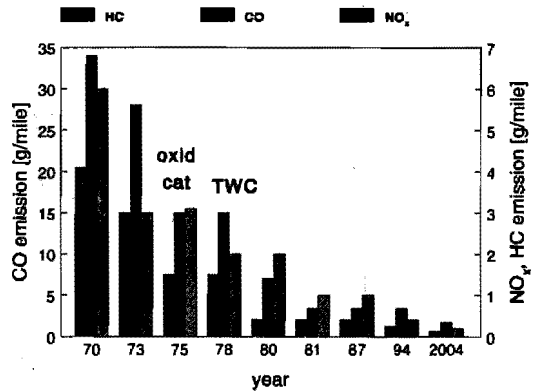


**Figure 1.1**  
**Federal emission standards for passenger cars in the US (adapted from Andersson, 1995).**

Lean burn engine operations *i.e.* engine operations with excess oxygen, see Figure 1.2, may lead to promising opportunities in meeting the future NO<sub>x</sub> standards. The lean air-fuel mixture fed to the engine reduces the combustion temperature resulting in lower NO<sub>x</sub> emissions. Furthermore, lean burn engines have a higher efficiency and hence a lower fuel consumption. Drawbacks are the reduced engine performance and the need for new catalysts which allow NO<sub>x</sub> reduction under net oxidizing conditions. The use of copper exchanged zeolite catalyst is investigated thoroughly in this respect (Ciambelli, *et al.*, 1994; Florera *et al.*, 1994).

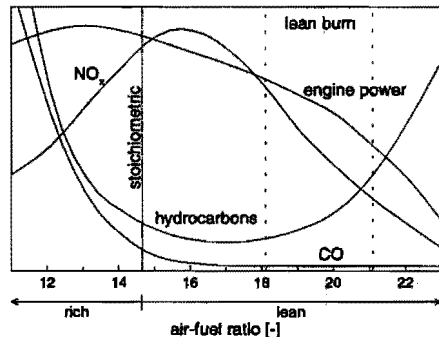


**Figure 1.2**  
**Effect of air-fuel ratio on the emissions of CO, NO<sub>x</sub> and hydrocarbons, and the engine power (not to scale) (Tamaru and Milis, 1994).**

An important driving force to evaluate the use of other metals than usually

applied platinum and rhodium is both technologically and economically. As new catalyst developments require improved thermal stability of both noble metal and support the use of palladium in three-way catalysts has been considered again. Using palladium instead of rhodium leads to better light-off performance (Beck and Sommers, 1994) and better thermal stability, but only in combination with tight air-to-fuel ratio control (Taylor, 1994). At present, rhodium is necessary for  $\text{NO}_x$  reduction resulting in catalyst dependence on the rhodium market. In 1994, 91% of the world rhodium demand was spent for three-way catalysts, while 35% of the platinum was used in automotive catalysts (Cowley, 1994). As the rhodium to platinum ratio in automotive catalysts exceeds by far the mining ratio (1/5 and 1/17, respectively) the rhodium may be short in supply regardless of the known reserves.

### Scope of this thesis

In order to meet the future emission standards it is necessary to optimize the applied catalytic converter for a broad range of process conditions. A thorough understanding of the underlying reaction kinetics is needed in that respect and, therefore, reliable kinetic models have to be acquired to account for the composition and temperature dependence of the reaction rates. As the converter is operated with an oscillating feed composition (Taylor and Sinkevitch, 1983) transient kinetic models based on elementary steps have to be developed whereas accumulation effects in the gas phase and on the catalytic surface have to be taken into account to describe the behaviour under realistic conditions. However, in the literature hardly any transient kinetic model has been published. Since the CO oxidation by oxygen is one of the most important reactions occurring in three-way catalysis, the kinetics of this reaction was studied under cyclic feeding conditions. The experiments using a  $\text{Pt}/\gamma\text{-Al}_2\text{O}_3$  catalyst were carried out below the light-off temperature as emissions after a cold engine start are a major problem. An elementary step kinetic model was developed which describes the experimental responses.

The role of ceria in commercial three-way catalyst is still not clarified. Therefore, the reaction between CO and  $\text{O}_2$  over a Degussa  $\text{Pt}/\text{Rh}/\text{CeO}_2/\gamma\text{-Al}_2\text{O}_3$  catalyst during forced concentration cycling was studied. The effects of ceria on the time-average conversion were also addressed. Moreover, as real exhaust gas contains steam and  $\text{CO}_2$  the influence of these components on the reaction rate was also investigated.

A transient model of an industrial monolith converter was developed to simulate the behaviour under dynamic conditions. Forced concentration cycling may lead to higher time-average reactor performance depending on the operating conditions (Lie *et al.*, 1993; Nievergeld, 1994; Nievergeld, *et al.*, 1994). The effects on the time-average conversions of CO, NO and hydrocarbons as a function of the feed

temperature, the feed composition and the cycling frequency were calculated.

New catalyst technologies demand tight control of the air-to-fuel ratio and hence more sophisticated control schemes have to be developed. Controllers based on models of both the engine and the converter can be used to meet this requirement. To demonstrate the benefits of such a controller compared to a conventional controller the converter model was used in the design of a model based controller.

## References

- Andersson L., Mathematical modelling in catalytic automotive pollution control, Ph.D. Thesis, Chalmers University of Technology, Göteborg, 1995.
- Ball D.J., Jacque E., A palladium front brick study, *Preprints of the Third International Congress on Catalysis and Automotive Pollution Control (CaPoC3)*, 137-146, 1994.
- Beck D.D., Sommers J.W., Impact of sulfur on three-way catalysts: comparison of commercially produced Pd and Pt-Rh monoliths, *Preprints of the Third International Congress on Catalysis and Automotive Pollution Control (CaPoC3)*, 147-159, 1994.
- Ciambelli P., Corbo P., Gambino M., Indovina V., Moretti G., Campa M.C., Lean NO<sub>x</sub> reduction on Cu-NaY and Cu-HZSM-5 zeolites at the spark ignition engine exhaust, *Preprints of the Third International Congress on Catalysis and Automotive Pollution Control (CaPoC3)*, 377-386
- Cowley, A., Platinum 1994 Interim Review, Johnson-Matthey PLC., 1994
- Florea D., Georgescu L., Constantinescu F., Mănoiu D., Gaber D., Comănescu M., Zeolite catalysts for the purification of automotive exhaust gases, *Preprints of the Third International Congress on Catalysis and Automotive Pollution Control (CaPoC3)*, 441-450
- Gulati S.T., Socha L.S., Then P.M., Design and performance of a ceramic pre-converter system, *Preprints of the Third International Congress on Catalysis and Automotive Pollution Control (CaPoC3)*, 93-109, 1994.
- Kirchner T., Eigenberger G., Optimization of the cold-start behaviour of automotive catalysts using an electrically heated pre-catalyst, *Chem. Eng. Sci.*, **10**, 2409-2418, 1996
- Kirchner, T., Donnerstag A., König A., Eigenberger G., Influence of catalyst deactivation on the automotive emissions using different cold-start concepts, *Preprints of the Fourth International Congress on Catalysis and Automotive Pollution Control (CaPoC4)*, 39-48, 1997
- Lie A.B.K., Hoebink J.H.B.J., Marin G.B., The effects of oscillatory feeding of CO and O<sub>2</sub> on the performance of a monolithic catalytic converter of automobile exhaust



gas: a modelling study, *Chem. Eng. J.*, **53**, 47-54, 1993.

- Nievergeld A.J.L., Simulation and design of a catalytic monolith reactor for automobile exhaust gas conversion, Institute for Continuing Education, Eindhoven University of Technology, ISBN 90-5282-340-5, 1994.
- Nievergeld A.J.L., Hoebink J.H.B.J., Marin G.B., The performance of a monolithic catalytic converter of automotive exhaust gas with oscillatory feeding of CO, NO and O<sub>2</sub>: a modelling study, *Preprints of the Fourth International Congress on Catalysis and Automotive Pollution Control (CaPoC4)*, 189-198, 1994
- Oh S.H., Bissett E.J., Battison P.A., Mathematical modeling of electrically heated monolith converters: Model formulation, numerical methods, and experimental verification, *Ind. Eng. Chem. Res.*, **32**, 1560-1567, 1993
- Rijkeboer R.C., Catalysts on cars - practical experience, *Catal. Today* **11**(1), 141-150, 1991.
- Tagliaferri S., Padeste L., Baiker A., Behaviour of three-way catalysts in hybrid drive systems. Dynamic measurements and kinetic modelling, *Preprints of the Third International Congress on Catalysis and Automotive Pollution Control (CaPoC3)*, 81-92, 1994.
- Tamaru K., Mills G.A., Catalysts for control of exhaust emissions, *Cat. Today*, **22**, 349-360, 1994
- Taylor, K.C., Sinkevitch, R.M., Behaviour of automotive exhaust catalyst with cyclic feed streams, *Ind. Eng. Chem. Prod. Res. Dev.*, **22**, 45-51, 1983.
- Taylor K.C., Nitric oxide catalysis in automotive exhaust systems, *Catal. Rev.-Sci. Eng.* **35**(4), 457-481, 1994.



# 2

---

## EXPERIMENTAL SET-UP AND PROCEDURES

### 2.1 Introduction

The experimental set-up to carry out kinetic experiments concerning automotive exhaust gas catalysis has been designed by Campman (1996). The equipment allows to perform experiments under both steady-state and cycling conditions. Cyclic feeding experiments can be carried out to study the effects of the oscillations on the time-average conversions (Matros, 1989). Furthermore, using data of dynamic experiments in kinetic studies is beneficial as they provide much more information about the reaction mechanism and the parameters than steady state experiments (Bailey, 1977). In designing the set-up special attention has been given to impose a well defined concentration square wave form on the catalyst bed. A special valve arrangement upstream of the packed bed reactor minimises the influences of back-mixing of reactants and products on the concentration cycles and, hence, allows experiments to be carried out at a relatively high frequency. The gas analysis has been designed to allow monitoring of concentrations at high sample frequencies. Furthermore, the set-up has been designed to perform experiments under operating conditions typical for automotive exhaust gas conversion.

In section 2.2 the experimental equipment is discussed in more detail. Some properties of the catalysts used during the transient experiments are presented in section 2.3. Section 2.4 deals with the pretreatment and stabilisation procedure before carrying out experiments and shows the results of some experiments with an oscillating feed between two Ar in He gas mixtures. These are carried out to get an indication of the upper limit of the oscillation frequency that can be obtained with the current set-up.

## 2.2 Experimental set-up

The experimental set-up used for the CO oxidation by oxygen with cycling of the feed composition is described in detail by Campman (1996). Some aspects of the equipment will be discussed in this section which are relevant for the work presented in this thesis. The complete set-up is schematically shown in Figure 2.1 and consists of a feed section A, a reactor section B and an analysis section C. The different sections will now be discussed.

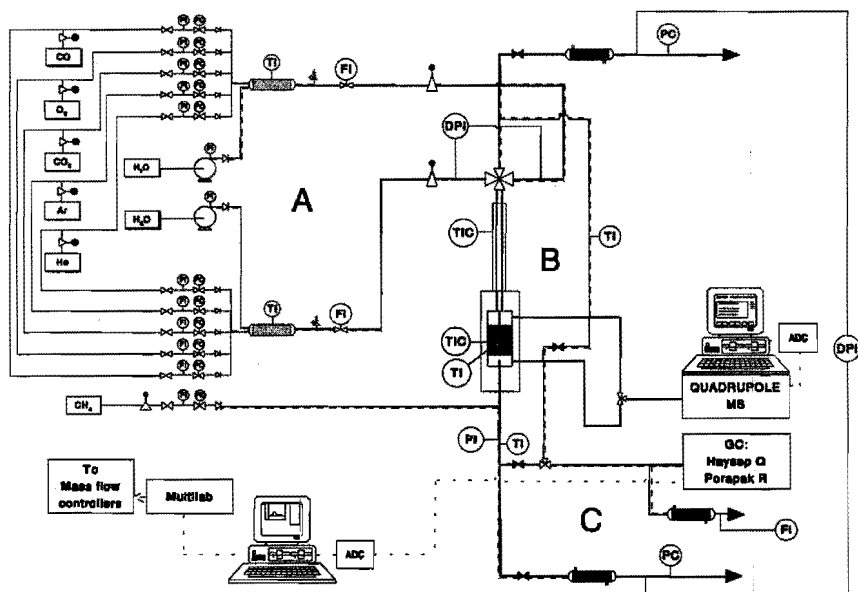


**Figure 2.1**  
*Schematic presentation of the experimental set-up.*

### 2.2.1 Feed section

The feed section contains two duplicate gas blending systems to allow the generation of two different feed streams necessary for cyclic operation of the reactor. In steady state experiments only one gas blended system is used. Whereas the total

molar flow rates of both feed streams will be kept equal during forced concentration cycling experiments, the compositions of the two feed streams will be different. A series of thermal gas mass flow controllers and a HPLC pump determine the composition of the feed stream. The pump is used to feed water to an evaporator located downstream of the mass flow controllers when experiments with a feed containing steam are carried out. In the simulation of real exhaust gas compositions this is an important requirement. The water evaporators are designed to feed a constant and reproducible steam flow.

Four magnetic valves (time to open or close: 3-5 ms) see Figure 2.1, are used to generate square wave concentration cycles. By opening the valves two by two one feed stream is passed to the reactor while the other is directed immediately towards the ventilation. The switching of the valves is synchronised by two timers using 1 ms increments which permits either symmetrical or asymmetrical concentration cycling with frequencies between 0.05 and 20 Hz. Pressure changes in the reactor due to switching the valves are minimised by carefully adjusting the pressure controllers downstream of the reactor and in the bypass line.

Downstream of the magnetic valves two separated feed lines, one for each feed stream, lead to the reactor. Before entering the catalyst bed the feed streams are preheated by a tubular preheater. The temperature of the preheater is measured with a thermocouple and controlled by a PID-controller. A programmable logic controller (PLC) actuates the electromagnetic valves which secure the gas supply lines and controls the high speed electromagnetic valves. The PLC also watches the reactor temperature: if the reactor temperature is higher than 700 K all electromagnetic valves of the gas feed lines except the one for the balance gas He are closed.

The gases He, CO, O<sub>2</sub>, CO<sub>2</sub> and CH<sub>4</sub> (internal standard of the gas chromatograph) used in the experiments have purities of respectively 99.995 vol%, 99.997 vol%, 99.995 vol%, 99.995 vol% and 99.995 vol% and were supplied by Hoekloos.

## 2.2.2 Reactor section

The reactor section consists of a stainless steel reactor which is contained in a cylindrical oven. A cross-section of the reactor is depicted in Figure 2.2. The two feed lines end in precision-machined chambers in the top of the reactor. Sapphire beads, one for each chamber, located downstream of the reactor inlet act as one-way valves. Although Figure 2.2 shows only two beads and chambers for simplicity, six of them were present actually, distributing each feed over three parallel channels equally divided over the cross-section of the reactor. If not pressurized, each sapphire bead is lifted by a flexible metal spring thus closing the corresponding feed line. The metal spring has been constructed of Duratherm, a Ti and Al containing Co/Ni/Cr alloy which retains its

elasticity up to 1000 K. The strength of the metal spring is adjusted in such a way that the feed line which becomes pressurized is open, while the other feed line remains closed. The valve spring is retained by a sintered quartz plate which also serves to enhance the radial distribution of the inlet feed stream. By this reactor design square wave concentration cycles can be generated with a minimal extent of mixing between the two feed streams. A thermocouple in the thermocouple tube is used to measure the axial temperature profile in the catalyst bed. The reactor pressure is controlled by a spring loaded back pressure controller and measured using a pressure transducer in combination with a digital indicating device. The catalyst bed itself is 10 mm high with a diameter of 13 mm. Immediately upstream and downstream of the catalyst bed mass spectrometer capillaries are inserted into the sample chambers to allow the real time analysis of the feed stream entering the bed and the composition effluent respectively. The residence time in the sample chambers is very small compared with the period of the oscillation under the experimental conditions applied meaning that the chambers do not affect the shape of the inlet and outlet concentration wave form.

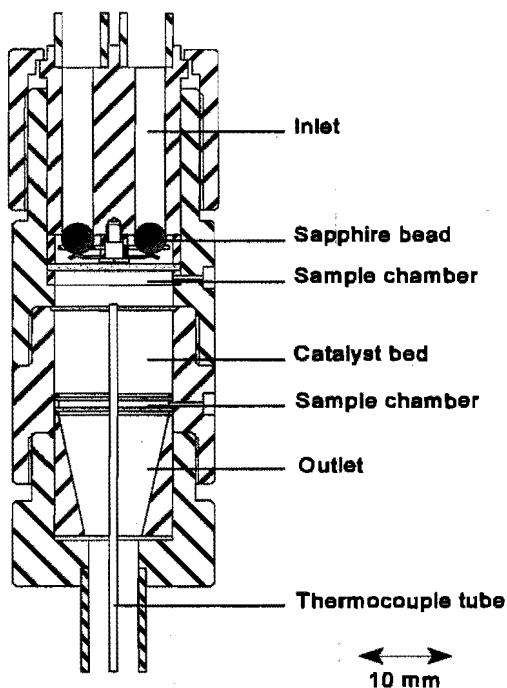


**Figure 2.2**  
*Detailed view of the fixed bed reactor used in the cyclic feeding experiments.*

### 2.2.3 Analysis section

The analysis section contains a gas chromatograph (Carlo Erba Instruments GC 8340) and a quadrupole mass spectrometer (VG Sensor lab 200D). The gas chromatograph is used in catalyst line-out experiments as the catalyst activity changes on a time scale of hours. It has been designed to enable online quantitative analysis of  $H_2$ ,  $N_2$ ,  $CO$ ,  $NO$ ,  $O_2$ ,  $CO_2$  and  $N_2O$ . Methane serves as internal standard component and is added to the reactor effluent directly downstream of the reactor; 99.999% pure helium is used as carrier gas. Remote control of the gas chromatographic analysis as well as

data acquisition and data analysis are performed using HP Chemstation software (Hewlett Packard) installed on a personal computer.

The online analysis of the composition at the reactor inlet and the outlet during experiments with a cycling of the feed is performed using the mass spectrometer. Two stainless steel capillary ( $L = 1.8$  m,  $d_i = 0.3$  mm) are connected to the sample chambers located directly upstream and downstream of the catalyst bed, see Figure 2.2, and to a zero volume three-way valve which leads to the mass spectrometer inlet. By switching the three-way valve, either the reactor feed or the reactor effluent can be sampled. The time resolution of the mass spectrometer was enhanced by application of software and hardware originating from mass spectrometer systems used in breath analysis in a medical environment. Mass spectrometer control and data acquisition are performed by VG Medical software running on a dedicated personal computer. This arrangement allows gas composition analysis at a sample frequency of typically  $120/n$  Hz, where  $n$  denotes the number of atomic mass units to be measured, meaning that a mixture containing He, CO, O<sub>2</sub> and CO<sub>2</sub> can be analysed thirty times per second.

To obtain quantitative measurements the mass spectrometer is calibrated daily, before starting the cyclic feeding experiments by passing known gas mixtures through the reactor. The calibration procedure is discussed in section 2.4.2.

### 2.3 Catalyst preparation and characterisation

The catalysts were supplied as a powder by Degussa A.G. with a mean particle diameter of 12  $\mu\text{m}$  which is too small for the experiments in the micro-fixed bed reactor as using this powder would result in a significant pressure drop over the catalyst bed. Therefore, the powder was pressed into small pellets at a pressure of GPa for 1 minute. The pellets were crushed and sieved afterwards and the desired fraction was collected. Some properties of the Pt/ $\gamma$ -Al<sub>2</sub>O<sub>3</sub> and the Pt/Rh/CeO<sub>2</sub>/ $\gamma$ -Al<sub>2</sub>O<sub>3</sub> catalyst after pressing, crushing and sieving are presented in Table 2.1.

The catalyst texture properties shown in Table 2.1 have been derived from static CO and O<sub>2</sub> chemisorption measurements and from literature (Campman, 1996). Both the CO and the O<sub>2</sub> chemisorption procedure were the same as Campman (1996) used for CO chemisorption measurements. The catalyst pretreatment during the chemisorption procedure was similar to pretreatment of the samples used for the cyclic feeding experiments. From the CO chemisorption capacities of the catalyst the fractions exposed noble metal were calculated using 1 CO per Pt atom and 2 CO atoms per Rh atom. The O<sub>2</sub> chemisorption measurements with the Pt/ $\gamma$ -Al<sub>2</sub>O<sub>3</sub> catalyst were performed to determine the oxygen adsorption capacity using one oxygen adatom per Pt atom.

**Table 2.1**  
**Physico-chemical catalyst properties.**

Catalyst		Pt/ $\gamma$ -Al <sub>2</sub> O <sub>3</sub>	Pt/Rh/CeO <sub>2</sub> / $\gamma$ -Al <sub>2</sub> O <sub>3</sub>
<b>Texture properties</b>			
$\bar{r}$	/nm	5	10
$a_s$	/m <sup>2</sup> kg <sup>-1</sup>	225 10 <sup>3</sup>	125 10 <sup>3</sup>
$v_{\text{pore}}$ (BET)	/m <sup>3</sup> kg <sup>-1</sup>	0.54 10 <sup>-3</sup>	0.35 10 <sup>-3</sup>
$d_p$	/m	0.25-0.30 10 <sup>-3</sup>	0.15-0.20 10 <sup>-3</sup>
$\rho$	/kg m <sup>-3</sup>	1230	2280
$\varepsilon_p$	/m <sup>3</sup> <sub>g</sub> m <sup>-3</sup> <sub>p</sub>	0.67	0.67
<b>CO Chemisorption capacities</b>			
$n_{\text{chem}}$	/mol kg <sub>c</sub> <sup>-1</sup>	1 10 <sup>-2</sup> (5 10 <sup>-3</sup> O <sub>2</sub> )	1.6 10 <sup>-2</sup>
FE	/mol <sub>s</sub> mol <sup>-1</sup>	0.49	0.45
$L_{\text{NM}}$	/mol kg <sub>c</sub> <sup>-1</sup>	1 10 <sup>-2</sup>	1.3 10 <sup>-2</sup>
<b>Weight fraction</b>			
$w_{\text{Pt}}$	/kg kg <sub>c</sub> <sup>-1</sup>	3.98 10 <sup>-3</sup>	3.98 10 <sup>-3</sup>
$w_{\text{Rh}}$	/kg kg <sub>c</sub> <sup>-1</sup>	-	0.79 10 <sup>-3</sup>
$w_{\text{CeO}_2}$	/kg kg <sub>c</sub> <sup>-1</sup>	-	0.3

## 2.4 Experimental procedures

### 2.4.1 Catalyst pretreatment and stabilisation

In order to enable reproducible kinetic experiments an appropriate catalyst pretreatment procedure is important. The pretreatment procedure carried out prior to the experiments described in this thesis is the same procedure as was used by Campman (1996). At first the catalyst is heated to 773 K in a flow of He. Then the



**Table 2.2****Experimental conditions during catalyst pretreatment ( $p = 110$  kPa).**

pretreatment phase	inlet flow rate /mol s <sup>-1</sup>			T /K	t /min
	He	O <sub>2</sub>	H <sub>2</sub>		
heating	$1.7 \cdot 10^{-3}$	0	0	293– 773	30
oxidation	$5.6 \cdot 10^{-4}$	$1.4 \cdot 10^{-4}$	0	773	60
purge	$1.7 \cdot 10^{-3}$	0	0	773	30
reduction	$8.4 \cdot 10^{-4}$	0	$4.4 \cdot 10^{-5}$	773	120
cooling	$1.7 \cdot 10^{-3}$	0	0	773→ T <sub>reaction</sub>	60

catalyst is kept under a pure He flow at 773 K for 30 minutes in order to purge reversibly adsorbed oxygen, followed by reduction in a He flow containing 5 vol% H<sub>2</sub> at 773 K for 120 minutes. Finally the catalyst is cooled down under a He stream to the reaction temperature. The catalyst pretreatment procedure is summarised in Table 2.2.

**Table 2.3****Experimental conditions during the line-out procedure.**

		Pt/γ-Al <sub>2</sub> O <sub>3</sub>	Pt/Rh/CeO <sub>2</sub> /γ-Al <sub>2</sub> O <sub>3</sub>
P <sub>CO</sub>	/kPa	2.2	0.55
P <sub>O<sub>2</sub></sub>	/kPa	2.2	0.55
P <sub>H<sub>2</sub>O</sub>	/kPa	0	0/11 <sup>*)</sup>
P <sub>CO<sub>2</sub></sub>	/kPa	0	0/11 <sup>*)</sup>
T	/K	423	393
F <sub>tot</sub>	/mol s <sup>-1</sup>	$6.4 \cdot 10^{-4}$	$5.6 \cdot 10^{-3}$

<sup>\*)</sup> Experiments with CO<sub>2</sub> and H<sub>2</sub>O

From introductory experiments it was found that both the Pt/γ-Al<sub>2</sub>O<sub>3</sub> and the Pt/Rh/CeO<sub>2</sub>/γ-Al<sub>2</sub>O<sub>3</sub> catalyst exhibited a higher initial activity after daily start-up as compared to the activity the day before. In order to minimise the influence of these reversible start-up effects on experimental results, a line-out procedure had to be carried out. After the catalyst pretreatment and before the experiments with cycling of the feed the catalyst activity was followed in time. The activity of the catalyst was assumed to be stable as the decay was less than 1% per hour. By comparing the

activity to the activity measured after the previous line-out the reproducibility of the experiments was ensured. Initially a He flow, containing also steam and CO<sub>2</sub> when applicable, was directed over the catalyst bed. Then CO was added to the flow followed by O<sub>2</sub> after one minute. The reason for this sequence is that when oxygen was fed prior to CO the catalyst bed sustained a transient temperature rise after adding CO, which caused a considerable delay in establishing a steady state. In Table 2.3 the experimental conditions during the line-out procedure are listed.

### 2.4.2 Calibration of the mass spectrometer

For a quantitative analysis of the reactor effluent the mass spectrometer was calibrated daily before the cyclic feeding experiments were started using four known gas mixtures containing He, CO, O<sub>2</sub> and CO<sub>2</sub>, see Table 2.4. The total flow and the total pressure were selected to be the same as during the cyclic feeding experiments since it turned out that they influence the measured intensities. After a stabilization period of 5 minutes the composition of the reactor feed was determined for each mixture by the mass spectrometer. The signals were used to deduct the calibration curves for each

**Table 2.4**

**Calibration mixtures 1 - 4 ( $F_{\text{tot}} \approx 5.6 \cdot 10^3 \text{ mol s}^{-1}$ )**

component		1	2	3	4
He	/vol%	100 (80)	99.4 (79)	98.8 (78)	97.6 (76)
CO	/vol%	0	0.2	0.5	1
O <sub>2</sub>	/vol%	0	0.3	0.5	1
CO <sub>2</sub>	/vol%	0 (10)	0.1 (10.5)	0.2 (11)	0.4 (12)
H <sub>2</sub> O	/vol%	0 (10)	0 (10)	0 (10)	0 (10)

Values between brackets are used during the cyclic feeding experiments with a feed also containing CO<sub>2</sub> and H<sub>2</sub>O.

component. For He a linear calibration curve was used as the mass spectrometer signal is proportional to high concentrations. For the other components second order polynomials were used as calibration curves. The coefficients of the curves were obtained by regression of the measured mass spectrometer intensities with the calibration curves.

### 2.4.3 Cycling of argon concentrations

To determine whether the effects of back mixing of reactants and products can be neglected in this study, cyclic feeding experiments with a feed containing argon have been carried out.

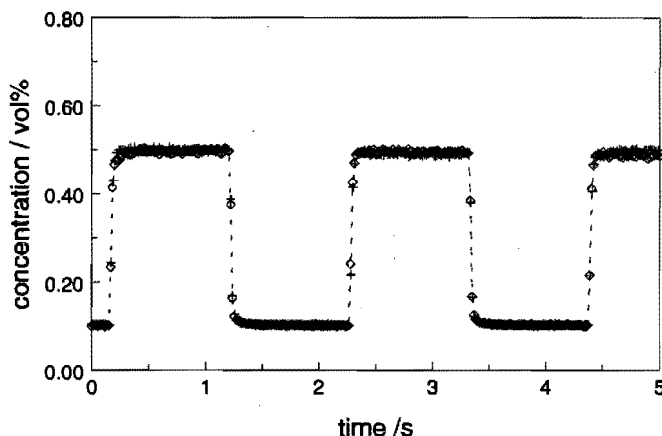


**Figure 2.3**

**Ar Inlet and outlet concentrations versus time during forced cycling.  $\diamond$  = inlet; + = outlet.  $f = 0.5$  Hz.**

In Figure 2.3 the outlet and the inlet concentrations of the reactor are given at an oscillation frequency of 0.5 Hz. As can be seen from this figure, the inlet signal is not distorted by the flow through the reactor and clearly the effects of back mixing can be neglected. Hence, the reactor can be regarded as an ideal plug flow reactor. The sample frequency of the mass spectrometer is also high enough as several samples are taken at the steep ascents and descents of the curves. Both the rise time and fall time amount to about 0.06 s which means that the highest frequency which can be applied without distortion of the amplitude is about 8 Hz. At higher frequencies the shape of inlet concentration tends to approach a harmonic function, but as long as both the reactor inlet and outlet compositions can be analysed with sufficient high time resolution the deviation from a square wave is rather irrelevant in kinetic studies.

### 2.4.4 Inlet concentrations

In Figure 2.4 the inlet concentrations during the cyclic feeding experiments are shown. Both the experiments with the Pt/ $\gamma$ -Al<sub>2</sub>O<sub>3</sub> and the Pt/Rh/CeO<sub>2</sub>/ $\gamma$ -Al<sub>2</sub>O<sub>3</sub> catalyst discussed in this thesis were carried out with feed concentrations as depicted in this figure. The feed stream was switched from 0.5 vol% CO to 0.5 vol% O<sub>2</sub> and vice versa. As the concentrations vary between zero and 0.5 vol% the surface coverages will also change over a very broad range and therefore much kinetic information will be available at the outlet of the reactor. Although the inlet concentration wave was the same for all experiments, both the reactor inlet and outlet compositions were measured during the cyclic feeding experiments. The measured inlet and outlet concentrations were used in the modelling.

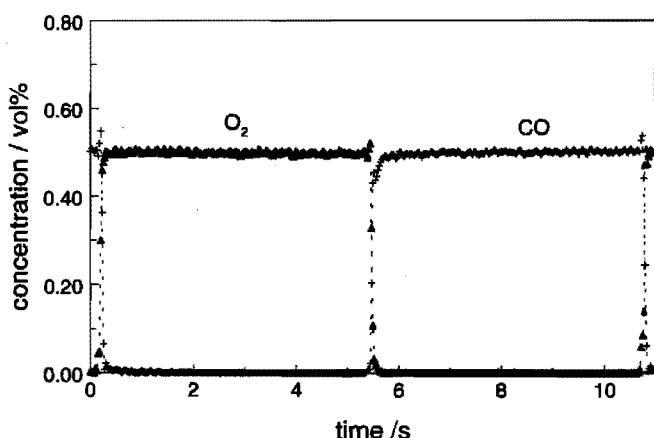


**Figure 2.4**  
*CO and O<sub>2</sub> inlet concentrations versus time during forced concentration cycling. + = CO; ▲ = O<sub>2</sub>;  $f = 0.1$  Hz.*

### 2.4.5 Smoothing of the experimental data

When carrying out preliminary experiments with a feed containing 10 vol% CO<sub>2</sub> and 10 vol% H<sub>2</sub>O it appeared that the signal-to-noise ratio of the CO<sub>2</sub> mass spectrometer measurement was rather low. A typical example of such an experiment is shown in Figure 2.5. Extracting kinetic information from the noisy CO<sub>2</sub> signal is difficult

and therefore a smoothing technique was applied to the original mass spectrometer data. The smoothed response is also shown in Figure 2.5 and the result is quite satisfactory. The smoothed and the original response were always compared to make sure no valuable information was lost by the applied smoothing method.

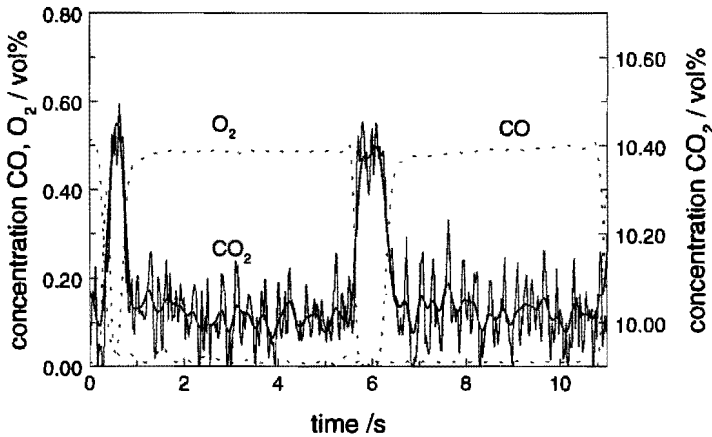


**Figure 2.5**

**Original (thin line) and smoothed (thick line)  $\text{CO}_2$  outlet concentration versus time during cyclic feeding of CO and  $\text{O}_2$ . Inlet concentrations see Figure 2.4. Feed stream also contains 10 vol%  $\text{H}_2\text{O}$  and 10 vol%  $\text{CO}_2$ ;  $f = 0.1$  Hz.**

The signal-to-noise ratio was increased by smoothing the data with cubic splines (NAG, 1995). The spline coefficients  $a_i$  are estimated by nonlinear regression of the original data with the object function given by:

$$S(a) = \min_a \sum_{i=1}^n w_i (y_i - f(a, x_i))^2 + \rho \int_{-\infty}^{\infty} (f''(a, x_i))^2 dx \quad (2.1)$$

where  $w_i$  is the (optional) weight for the  $i$ th observation and  $\rho$  the smoothing parameter. This object function consists of two parts: the first part measures the fit of the curve and the second part measures the smoothness of the curve. The value of the smoothing parameter,  $\rho$ , weights these two aspects: larger values of  $\rho$  give a smoother fitted curve (because the second order derivative of  $f(x)$  is then forced to be smaller), but in general a poorer fit. Smaller values of  $\rho$  give a less smoother curve but in general a better fit

and representation of the characteristics of the original observations. The unweighted smoothing presented in Figure 2.5 was performed with  $p$  amounting to 100.

### **References**

- Bailey, J.E., Periodic phenomena, in: Chemical reactor theory: A review, Lapidus L., and Amundson N.R., Eds., 758-813, Prentice-Hall, Englewood, NJ, 1977
- Campman, M.A.J., Kinetics of carbon monoxide oxidation over supported platinum catalysts, The role of steam in the presence of ceria, Ph.D. Thesis, Eindhoven University of Technology, 1996
- Matros, Y.S., Catalytic processes under unsteady-state conditions, Studies in surface science and catalysis, **43**, Elsevier, Amsterdam, 1989
- NAG Fortran Library Manual, mark 16, volume 1, 1995

# 3

---

## FREQUENCY RESPONSE ANALYSIS AIMED AT DETERMINATION OF KINETIC PARAMETERS

### 3.1 Introduction

Chemical reactors are usually operated in steady state, but periodic operation may be beneficial in some cases. From a practical point of view, dynamic reactor operation can result in a higher time-average performance (Bailey, 1977; Renken, 1984). When a reactor is operated dynamically, the instantaneous rates will usually be different from those obtainable at steady state resulting in a time-average performance of the reactor, which can change significantly as a function of the frequency of the applied oscillation. Usually, this phenomenon results from the nonlinear behaviour of the kinetics (Matros, 1989). From a more fundamental point of view, periodic reactor operation can be used to study the processes occurring in a reactor, such as transport phenomena and the reaction mechanism, and to estimate the corresponding rate coefficients. Compared to steady state operation, dynamic operation gives much more insight into the processes taking place.

A drawback of conducting transient experiments is the experimentally more complex equipment needed to generate the time-dependent input signals and to measure the resulting responses. Three types of input forcing functions are commonly applied to obtain more insight in the processes to be studied. Step changes and pulses are often used since they are easy to realize experimentally. The shape of the responses caused by the dynamic behaviour of the reactor system contains information about the rates of the individual steps of the occurring global processes. A drawback of step and pulse experiments is the difficulty to extract information about all individual

steps from the measured response. The shape of the observed response is mainly determined by the rate determining step, and therefore it is hard to obtain information about the other steps. Harmonic perturbations are the third type of forcing function. The information about the dynamics of the individual steps of the global processes is available in the amplitude of the output oscillation and the phase shift of the output with respect to the input. The frequency is adapted to highlight the dynamics of a particular step of the processes and therefore to obtain information about this step only. By applying a range of frequencies the rates and the corresponding coefficients of all steps can be determined. This in contrast to both step and pulse experiments, where the observed response contains information about all processes simultaneously.

The frequency response method uses harmonic functions as input wave form. Since this analysis is only applicable to linear systems straightforwardly, small amplitudes have to be applied when dealing with nonlinear systems. When estimating parameters of the steps by means of regression of the experimental data, the governing nonlinear model equations have to be linearized around the steady state to be able to derive the frequency response equations. Lynch and Walters (1990) showed that due to this linearization no valuable information about the dynamics of the processes is lost and linearization is, therefore, often allowed. One of the most promising features of the technique is its ability to discriminate between rivaling models due to the high sensitivity of the frequency response to the nature of the governing equations, as shown by several studies (Naphtali and Polinski, 1969; Marcelin *et al.*, 1986; Schrieffer and Sinfelt, 1990; Yasuda *et al.*, 1991).

One first application of the frequency response analysis was the determination of the distribution of residence times in a continuous flow system (Kramers and Alberda, 1953). Lynch and Walters (1990) used the frequency response analysis to characterize an external recycle reactor. However, the most important usage of this technique reported in literature is the studying of the adsorption of gases in bidisperse sorbents (Jordi and Do, 1993, 1994; Sun and Bourdin, 1993; Sun *et al.*, 1994; Yasuda, 1994). Applications of the frequency response techniques in kinetic studies are in the minority. Naphtali and Polinski (1969) were the first to apply this technique in determining the adsorption rates on heterogeneous surfaces in a batch reactor. Several investigators showed that the technique is very suitable for the identification of different adsorption sites and determination of the corresponding rate constants in a batch reactor (Marcelin *et al.*, 1986; Yasuda, 1978, 1982, 1984, 1985, 1991). Li *et al.* (1989) and Lynch and Walters (1990) used the frequency response method to study the adsorption-desorption kinetics in continuous flow reactors. Madix and Schwarz (1971a), Madix *et al.* (1971b) and Schwarz and Madix (1974) applied the frequency response analysis to data obtained from a Modulated Beam Relaxation Spectrometry experiment. Schwartz *et al.* (1986) adapted the classical frequency response analysis to make its application possible to nonlinear systems without linearization of the equations and used it to study



adsorption and desorption in combination with surface diffusion. Using nonlinear model equations in the regression of the experimental data may lead to kinetic parameters which are valid over a wider range of conditions.

The purpose of this chapter is to study the frequency response method aimed at the determination of kinetic parameters in both a continuous stirred tank reactor and a plug flow reactor. Not only adsorption and desorption but also surface reaction will be considered in this study. The derived frequency response equations will be used to examine the dynamic behaviour of both reactors and the results of a parameter sensitivity analysis will show which reactor type is most suitable for in this respect.

### 3.2 Definitions

Before discussing the application of a frequency response analysis in kinetic studies, some definitions will be given. Usually, this analysis is applied to linear systems only. When dealing with nonlinear systems, *i.e.* systems characterized by a Jacobian which depends on the dependent variables, the experimentally applied perturbations should be small to allow the assumption of linearity. The latter means that the superposition principle holds and Laplace transforms are applicable in the analysis leading to easier-to-perform mathematics.

The dynamic behaviour of a linear system is described by the gain and the phase shift of the output with respect to the input. For input  $x(t)$  described by:

$$x(t) = A_{in} \sin(\omega t) \quad (3.1)$$

the output of the system is given by:

$$y(t) = A_{out}(\omega) \sin(\omega t + \phi(\omega)) \quad (3.2)$$

The gain of this system is defined by the ratio of the output amplitude and the input amplitude,  $A_{out}(\omega)/A_{in}$ , while the phase shift is given by  $\phi(\omega)$ . Both the gain and phase shift are functions of the frequency  $\omega$  and of the parameters one wants to estimate. When applying a frequency response analysis, the gain and the phase shift are the quantities to be measured and they are used in the regression process that determines the values of the kinetic parameters.

A system with more than one input and more than one output is called a MIMO-system (Multiple-Input, Multiple-Output). The dynamic behaviour of such a system is described by a number of gains and of phase shifts (number of input  $\times$  number of outputs), each with its own frequency dependency.

The characteristic response time  $\tau_c$  is defined by the time scale of the observed

output assuming a first order system, *i.e.* a system described by one first order differential equation and, therefore, having only one time constant. When dealing with a higher order system, the characteristic response time approximates the largest time scale involved. Based on the period  $T_m$  of the forced oscillation and the characteristic response time of the system, three different regimes of periodic operation can be distinguished (Bailey, 1977; Matros, 1989). In the classification of the regimes it is assumed that the system acts mainly as a first order system.

The first regime is the quasi-steady state regime ( $T_m \gg \tau_c$ ). In this case, the input varies rather slowly compared with the dynamics of the system and the system can be considered as always in a steady state.

When the period of the oscillation is of the same order as the characteristic response time ( $T_m \approx \tau_c$ ), the reactor is in the intermediate or dynamic regime. The transient behaviour has to be determined to predict the effects of the periodic operation. The frequency range corresponding to the quasi-steady state regime plus the dynamic regime is also called the bandwidth of the system.

The third one is the sliding regime, also called relaxed steady state regime. When the input variable varies rapidly relative to the characteristic response time ( $T_m \ll \tau_c$ ), the outlet oscillation will show a very small amplitude. The quasi-steady state approximation can be applied to determine the behaviour using the time-average value of the input variable.

It is also possible to study the dynamic behaviour of a system in the Laplace or in the frequency domain. Analyses in the Laplace domain are beneficial compared with studies in the time domain, since the time derivatives are transformed into corresponding polynomials in the Laplace variable and therefore the mathematics is easier. The output-input behaviour of a system in the Laplace domain is characterized by its transfer function. The output of the system is then given by:

$$Y(s) = H(s)X(s) \quad (3.3)$$

where  $H(s)$  is the transfer function which can belong to the complex domain.  $Y(s)$  and  $X(s)$  are Laplace transforms of the outlet and inlet signal, respectively. The gain is given by the absolute value of  $H(s)$ , while the phase shift is defined by its argument. Transformation from the Laplace domain to the frequency domain is done by the substitution of  $s=i\omega$ , where  $i=\sqrt{-1}$ .

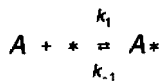
The kinetic parameter estimates are obtained by regression of the experimentally gathered amplitudes and/or phase shifts and the equations for the gain and phase shift in the frequency domain.

### 3.3 Adsorption and desorption in continuous flow reactors

#### 3.3.1 Introduction

To show the benefits of a frequency response analysis in the assessment of kinetic parameters, the simple example of adsorption and desorption on a catalyst surface is considered. The expressions of the gain and the phase shift were derived analytically and used to show the effects of parameter changes on the dynamic behaviour of the reactor. The parameter dependence of the calculated gain and phase shift is very important during the estimation process since it eventually determines the statistical significance of the parameter estimates.

The following example is considered:



A being the species to be adsorbed from the gas phase, \* a vacant site and A\* the adsorbed species. This process is studied in two reactor types: a continuous stirred tank reactor (CSTR) and a plug flow reactor (PFR). The inlet concentration is considered as input variable, while the outlet concentration serves as output. Although the frequency response analysis is often used to study adsorption-desorption in combination with transport phenomena, intrinsic kinetics are considered only in this example, as the purpose of this section is to show the application of this technique in the determination of kinetic parameters. During a frequency response analysis the gain and phase shift of the outlet concentration are measured as a function of the frequency when the inlet concentration oscillates harmonically around the steady state value with a fixed amplitude. The kinetic parameters can be obtained by regression of the measured data with the expressions for the gain and the phase shift derived from solving the continuity equations.

The continuity equation for adsorbed species A for both the CSTR and the PFR is given by:

$$\frac{d\theta_A}{dt} = k_1 C_A \theta_* - k_{-1} \theta_A \quad (3.4)$$

and the balance of the active sites is given by:

$$\theta_* + \theta_A = 1 \quad (3.5)$$

where  $\theta_A$  and  $\theta_*$  are the fractional surface coverage of A and the fraction of vacant sites,

respectively. In the next two sections the expressions for the gain and the phase shift will be derived for both the CSTR and the plug flow reactor.

### 3.3.2 Adsorption-desorption in a CSTR

The continuity equation for A in the gas phase of the CSTR is given by:

$$\frac{dC_A}{dt} = \frac{1}{\tau_R} (C_A^{\text{in}} - C_A) - C_{\text{NM}} (k_1 C_A \theta_A - k_{-1} \theta_A) \quad (3.6)$$

where the residence time  $\tau_R$  is defined by

$$\tau_R = \frac{V_R}{F_V} \quad (3.7)$$

and assumed to be constant.  $C_{\text{NM}}$  denotes the ratio of the capacity of the catalyst surface and the capacity of the gas phase in  $\text{mol}_{\text{NM}}/\text{m}_g^3$ .

When applying the frequency response method, the nonlinear differential equations 3.4 and 3.6 are linearized around the steady state. Therefore, the system is assumed to be at steady state before the oscillation is started. The initial conditions for the gas phase concentration and the surface coverage are then given by the time-average inlet concentration and the steady state surface coverage:

$$\theta_A(0) = \theta_A^{\text{ss}} \wedge C_A(0) = C_A^{\text{ss}} \quad (3.8)$$

As no reaction takes place the outlet concentration equals the inlet concentration in steady state and the surface coverage is determined by the inlet concentration only.

Both the inlet and outlet concentrations and the surface coverage oscillate harmonically around the steady state, which can be expressed as:

$$C_A^{\text{in}}(t) = C_A^{\text{ss}} + \Delta C_A^{\text{in}}(t), C_A(t) = C_A^{\text{ss}} + \Delta C_A(t), \theta_A(t) = \theta_A^{\text{ss}} + \Delta \theta_A(t) \quad (3.9)$$

After substitution of the expressions given in Equation 3.9 into Equations 3.4 to 3.6 and neglecting second order terms of  $\Delta$ , a set of linear differential equations in  $\Delta$  is obtained, which is transformed to the frequency domain. The expression for the gain is given by:

$$|H(\omega)| = \frac{1}{\tau_R} \sqrt{\frac{(1 + \omega^2 \tau_1^2) \tau_2^2}{\tau_2^2 \tau_1^2 \omega^4 + (2C_{NM} \tau_2^2 k_1 k_{-1} \tau_1^2 + \tau_1^2 + \tau_2^2) \omega^2 + (1 - C_{NM} \tau_2 k_1 k_{-1} \tau_1)^2}} \quad (3.10)$$

and for the phase shift:

$$\phi = - \arctan \left( \frac{\omega \tau_2 (1 + C_{NM} k_1 k_{-1} \tau_1^2 + \omega^2 \tau_1^2)}{1 + C_{NM} k_1 k_{-1} \tau_1 \tau_2 + \omega^2 \tau_1^2} \right) \quad (3.11)$$

where  $\tau_1$  and  $\tau_2$  are given by:

$$\tau_1 = \frac{1}{k_1 C_A^{ss} + k_{-1}} \quad (3.12)$$

$$\tau_2 = \frac{1}{\frac{1}{\tau_R} + C_{NM} k_1 k_{-1} \tau_1}$$

The complete derivation of Equations 3.10 and 3.11 is given in appendix 3A. Both  $\tau_1$  and  $\tau_2$  can be considered as time scales assuming the surface and the gas phase are decoupled, *i.e.*  $\Delta C_A$  is an independent input variable in the equation corresponding to the balance for the surface species A. This is the case when the gas phase capacity is much larger than the capacity of the surface, *i.e.*  $C_{NM}$  is small.  $\tau_1$  expresses then the time scale of relaxation to the steady state of adsorbed A as a result of a changes of  $\Delta C_A$  or  $\Delta C_A^{in}$ . When  $C_{NM}$  is rather large, the expressions of the time-scales have to be derived from Equation 3.10 resulting in rather complex equations without giving more insight into the dynamic behaviour of the reactor. Hence, they are not shown in this section.

Due to the complexity of Equations 3.10 and 3.11, the dynamic behaviour is not immediately clear. However, limiting values for the gain and the phase shift in the sliding regime are 0 and  $-\pi/2$  respectively, and therefore no kinetic information is available at the outlet of the reactor for high frequencies. More properties related to Equations 3.10 and 3.11 will be shown in section 3.3.4, where the dynamic behaviour of CSTR and plug flow reactor are compared. From Equations 3.10 and 3.11 it is clear that the dynamic behaviour of the CSTR not only depends on the kinetic parameters but also on the ratio of the gas phase capacity and the surface capacity  $C_{NM}$ , and on the residence time  $\tau_R$ . Hence, by carefully selecting the appropriate experimental conditions as much as possible information about the kinetic parameters can be extracted from the outlet

concentration within the range of allowed operating conditions.

### 3.3.3 Adsorption-desorption in a plug flow reactor

The example given in section 3.3.1 is now considered in a plug flow reactor. The continuity equation for A in the gas phase is expressed as:

$$\frac{\partial C_A}{\partial t} = -v \frac{\partial C_A}{\partial x} - C_{NM}(k_1 C_A \theta_s - k_{-1} \theta_A) \quad (3.13)$$

The continuity equations for the surface species, Equations 3.4 and 3.5, hold also for the plug flow reactor. Initial conditions are given by the steady state concentration and surface coverage profiles:

$$C_A(x,0) = C_A^{ss}, \theta_A(x,0) = \theta_A^{ss} \quad (3.14)$$

and the boundary condition by the time-dependent inlet concentration:

$$C_A(0,t) = C_A^{in}(t) \quad (3.15)$$

The expressions are linearized around the steady state using:

$$C_A(x,t) = C_A^{ss} + \Delta C_A(x,t), \theta_A(x,t) = \theta_A^{ss} + \Delta \theta_A(x,t) \quad (3.16)$$

Equation 3.16 is substituted into Equations 3.4, 3.5 and 3.13 and second order terms in  $\Delta$  are neglected. Application of the Laplace operator in time to the linearized equations results in an ordinary differential equation for the continuity equation of A in the gas phase and in an algebraic equation for the species on the catalyst surface. The Laplace transformed surface coverage is eliminated from the continuity equation for A in the gas phase and the governing differential equation is integrated in the x-direction. After transformation to the frequency domain equations for the gain and the phase shift are obtained. In appendix 3A the complete derivation is shown.

The gain is expressed by

$$|H(\omega)| = \exp \left( - \frac{T_R T_1^3 C_{NM} k_{-1} k_1 \omega^2}{1 + \omega^2 T_1^2} \right) \quad (3.17)$$

and the phase shift by:

$$\phi = - \frac{\tau_R \omega (1 + C_{NM} k_{-1} k_1 \tau_1^2 + \omega^2 \tau_1^2)}{1 + \omega^2 \tau_1^2} \quad (3.18)$$

where  $\tau_1$  is given by Equation 3.12.

Equations 3.17 and 3.18 show that both the gain and the phase shift are not only dependent on the kinetic parameters to be estimated but also on the reactor parameters  $\tau_R$  and  $C_{NM}$ . Higher values of  $\tau_R$  and  $C_{NM}$  lead to a faster decreasing gain as a function of the frequency and consequently a smaller bandwidth. Hence, their values can be selecting according to the limitations of the experimental setup. From Equation 3.18 it is clear that  $C_{NM}$  should be large enough in order to estimate kinetic parameters since the phase shift is a function of the residence time only for small values of  $C_{NM}$  and no kinetic information can be extracted from the outlet concentration. In contrast to the CSTR, the gain is still a function of the kinetic parameters in the sliding regime whereas the phase shift becomes proportional to the frequency for very high frequencies and, hence, contains no kinetic information.

### 3.3.4 Dynamics of a CSTR versus a plug flow reactor

To demonstrate which reactor type is preferably used for the identification of kinetic parameters, the gain and the phase shift are calculated using the parameters shown in Table 3.1. The parameters are chosen to simulate the behaviour of potentially fast adsorbing species on a catalyst surface such as sorption of CO on platinum. It is assumed that the dynamic regime is entered when the deviation from the gain at very low frequencies amounts to 10%, whereas the sliding regime starts at a 90% reduction of the gain.

As shown in Figure 3.1, the dynamic regime of the CSTR is entered at a frequency of 0.25 Hz and ends at 5 Hz. The gain of the CSTR decreases initially faster than the gain of the plug flow reactor with increasing frequency, but remains almost constant in the sliding regime ( $f > 5$  Hz). In this regime the gain is strongly dependent on the frequency.

**Table 3.1**

**Parameters used to calculate the gain and the phase shift of the CSTR, using Equations 3.10 and 3.11, and the plug flow reactor, Equations 3.17 and 3.18.**

$k_1$	/mol <sup>-1</sup> m <sub>g</sub> <sup>3</sup> s <sup>-1</sup>	1000
$k_{-1}$	/s <sup>-1</sup>	10
$\tau_R$	/s	0.1
$C_A^{ss}$	/mol m <sub>g</sub> <sup>-3</sup>	0.2
$C_{NM}$	/mol <sub>s</sub> m <sub>g</sub> <sup>-3</sup>	10
$\tau_1$	/s	$4.8 \cdot 10^{-3}$
$\tau_2$	/s	$2.1 \cdot 10^{-3}$

The dynamic regime of the PFR starts at about 2 Hz and ends at 8 Hz; the sliding regime is not entered. Apparently, the broader bandwidth of the plug flow reactor compared to the bandwidth of the CSTR can be explained by the absence of mixing in the gas phase. This also means that mixing plays an important role in the dynamic behaviour of the CSTR and probably less detailed kinetic information will be available at the outlet of the reactor.  $\tau_1$  and  $\tau_2$  cannot be considered as time-scales as they suggest a bandwidth of one order of magnitude larger than the one shown in Figure 3.1.

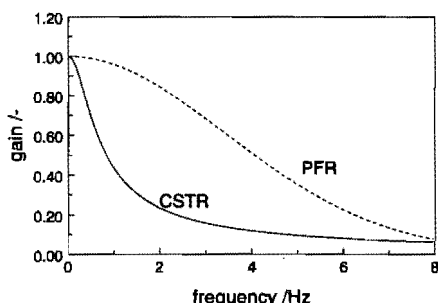


**Figure 3.1**

*The gain of the CSTR and the plug flow reactor versus the frequency calculated using Equations 3.10 and 3.15. Parameters: Table 3.1, (---) = plug flow reactor; (—) = CSTR.*

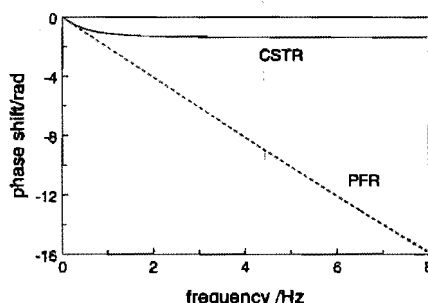


**Figure 3.2**

*The phase shift of the CSTR and the plug flow reactor versus the frequency calculated using Equations 3.11 and 3.16. Parameters: Table 3.1, (---) = plug flow reactor; (—) = CSTR.*

Figure 3.2 shows that the frequency dependence of the phase shift of the CSTR is less pronounced than the frequency dependence of the gain. However, it is not clear whether the gain or the phase shift should be used in the determination of kinetic parameters. The phase shift of the plug flow reactor decreases linearly as a function of the frequency. It should however be noted that the phase shift is not only caused by the residence time but also by the interaction with the catalyst surface since the phase shift due to the gas flow through the reactor only amounts to  $-2\pi f\tau_R$  which is not in line with Figure 3.2.

As mixing in the gas phase also determines the dynamic behaviour of the CSTR, the observability of the parameters will probably be better in the plug flow reactor than in the CSTR. In the next section a parameter sensitivity analysis will show if this is the case.



### 3.3.5 Parameter sensitivity analysis

When applying the frequency response method, the kinetic parameters are adapted in such a way that the measured gain and phase shift as a function of the frequency can be described by the model. Usually the kinetic parameters are estimated by means of nonlinear regression and the sensitivity of the calculated gain and the phase shift to parameter variations is very important in obtaining statistically significant parameter estimates. To investigate this parameter sensitivity in a CSTR and a plug flow reactor both parameters  $k_1$  and  $k_{-1}$  were changed simultaneously with + and - 10% of the values given in Table 3.1. The equilibrium coefficient  $k_1/k_{-1}$  remains constant in this way. When comparing the effects of the parameter variations on the gain and the phase shift of the CSTR and the plug flow reactor it will become clear which reactor type is preferably used in the determination of kinetic parameters. The deviations of the gain and phase shift depicted in Figures 3.1 and 3.2, are given in Figures 3.3 and 3.4.

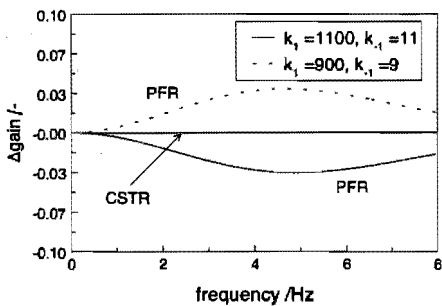


**Figure 3.3**  
**Deviation of the gain of both the CSTR and the plug flow reactor versus the frequency due to a 10% change of parameters given in Table 3.1. (---) = -10%; (—) = +10%.**

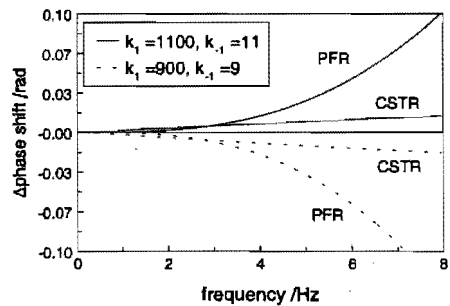


**Figure 3.4**  
**Deviation of the phase shift of both the CSTR and the plug flow reactor versus the frequency due to a 10% change of parameters given in Table 3.1. (---) = -10%; (—) = +10%.**

As shown in Figure 3.3, changing the values of both parameters simultaneously does not affect the gain of the CSTR which means that adsorption and desorption are in equilibrium with the gas phase and no information about the individual parameters is obtainable from the output. However, the gain is affected when one parameter only is changed, but the effects of the individual parameter variations cancel out when both parameters are changed simultaneously. As shown in the same figure, the gain of the PFR depends on the values of the individual parameters. Both parameters can be estimated and the optimal frequency range is between 2 and 8 Hz. For frequencies

higher than the ones shown in Figure 3.3, the deviation of the gain goes to zero. It is therefore not beneficial in this case to apply higher frequencies when estimating the kinetic parameters by means of the frequency response method.

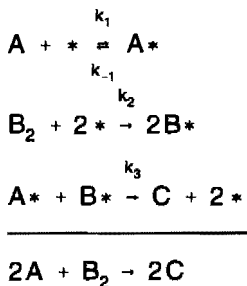
As shown in Figure 3.4, the behaviour of the phase shift is similar to that of the gain. The deviation of the phase shift of the CSTR changes only slightly as a function of the parameters. At frequencies above 4 Hz the phase shift of the PFR is strongly affected by the parameters variations. Clearly when using the phase shift of the PFR in the regression process the frequency should be relatively high.

Summarizing, the plug flow reactor is more suitable for the determination of kinetic parameters using the frequency response method than the CSTR. Both the measured gain and the measured phase shift can be used in the regression, and it is not necessary to apply very high frequencies for all practical purposes. When the frequency response method is applied to reactions with different behaviour, the frequency dependence of the gain and the phase shift will differ from those shown in Figures 3.1 and 3.2. Hence, a parameter sensitivity analysis has to be carried out for all individual cases. However, quasi-steady state operation will always reveal similar kinetic information as steady state operation. The dynamic behaviour of the CSTR will always be determined by both the reaction kinetics and mixing in the gas phase and, hence, experiments with a plug flow reactor will result in more detailed kinetic models of the occurring reactions.

### 3.4 Three-step mechanism in continuous flow reactors

#### 3.4.1 Kinetic model

The examples discussed in section 3.3 are extended to a three-step reaction mechanism. Not only adsorption and desorption of A is considered but the dissociative adsorption of another component B<sub>2</sub> followed by surface reaction between the adsorbed species is also taken into account. The reaction mechanism used in the examples of the CSTR and the plug flow reactor is given by:



The surface coverages are calculated by solving the continuity equations for the species on the catalyst surface which are given by:

$$\frac{\partial \theta_A}{\partial t} = k_1 C_A \theta_* - k_{-1} \theta_A - k_3 \theta_A \theta_B \quad (3.19)$$

$$\frac{\partial \theta_B}{\partial t} = 2k_2 C_B \theta_*^2 - k_3 \theta_A \theta_B \quad (3.20)$$

and the balance of the active sites by:

$$\theta_* + \theta_A + \theta_B = 1 \quad (3.21)$$

In Table 3.2 the kinetic parameter values are given. The values are chosen to approximate the behaviour of the CO oxidation by O<sub>2</sub> over a supported platinum catalyst. This means that at the conditions shown in Table 3.2 adsorption of B<sub>2</sub> is inhibited by adsorbed A. By setting the accumulation terms of Equations 3.19 and 3.20 to zero and solving the resulting set of nonlinear equations, an expression for the steady state reaction rate is obtained. Since multiple complex solutions arise from the nonlinear equations, the expression of the reaction rate is not just one simple expression. But, under the given conditions it is reasonable to assume CO adsorption equilibrium. With the adsorption of B<sub>2</sub> being the rate determining step, implying  $\theta_B \ll \theta_A$ , the steady state reaction rate is given by:

$$R = 2 \frac{k_2 C_{B_2}}{K_1^2 C_A^2} \quad (3.22)$$

**Table 3.2**

**Parameters used to calculate the gain and phase shift of the outlet concentrations of both the CSTR and the plug flow reactor.**

$k_1$	/mol <sup>-1</sup> m <sub>g</sub> <sup>3</sup> s <sup>-1</sup>	1000
$k_{-1}$	/s <sup>-1</sup>	10
$k_2$	/mol <sup>-1</sup> m <sub>g</sub> <sup>3</sup> s <sup>-1</sup>	100
$k_3$	/s <sup>-1</sup>	10
$T_R$	/s	0.1
$C_A^{in}$	/mol m <sub>g</sub> <sup>-3</sup>	0.2
$C_{B_2}^{in}$	/mol m <sub>g</sub> <sup>-3</sup>	0.1
$C_{NM}$	/mol m <sub>g</sub> <sup>-3</sup>	10

From Equation 3.22 it is clear that conducting steady state experiments at the conditions

given in Table 3.2, the values of the individual parameters cannot be estimated. Information about a lumped parameter, consisting of the ratio of the adsorption coefficient of  $B_2$  and the equilibrium constant  $K_1$  of A, can be extracted only from the measured data.

In the next two sections the gain and the phase shift for both the CSTR and the plug flow reactor are calculated numerically, since analytical solutions cannot be obtained. In section 3.4.4 a parameter sensitivity analysis is conducted to show which reactor is most suited for the determination of termination of kinetic parameters when applying a frequency response analysis.

### 3.4.2 Three-step mechanism in a CSTR

The model of the CSTR consists of the components in the gas phase and the species on the catalyst surface. The continuity equations for the species on the catalyst surface are given in section 3.4.1, while for components A,  $B_2$  and C in the gas phase they are given by:

$$\frac{dC_A}{dt} = \frac{1}{\tau_R} (C_A^{in} - C_A) - C_{NM} (k_1 C_A \theta_* - k_{-1} \theta_A) \quad (3.23)$$

$$\frac{dC_B}{dt} = \frac{1}{\tau_R} (C_B^{in} - C_B) - C_{NM} k_2 C_B \theta_*^2 \quad (3.24)$$

$$\frac{dC_C}{dt} = \frac{1}{\tau_R} (C_C^{in} - C_C) + C_{NM} k_3 \theta_A \theta_B \quad (3.25)$$

The initial conditions are given by the steady state solution:

$$\begin{aligned} C_i(0) &= C_i^{ss}, \quad i = A, B_2, C \\ \theta_j(0) &= \theta_j^{ss}, \quad j = A, B, C \end{aligned} \quad (3.26)$$

Equations 3.19 to 3.21 and 3.23 to 3.25 have to be linearized around the steady state in order to allow the application of the frequency response method. The steady state is calculated by setting the accumulations terms to zero and solving the set of

algebraic equations numerically using a modified Newton-Raphson algorithm, implemented in NAG routine C05NBF (NAG, 1995). The expressions of the linearized equations and the methods used to solve them are given in appendix 3B. The results of the calculations using the parameters given in Table 3.2 when the concentration of A at the inlet is oscillating only will be discussed first. Next the gain and the phase shift will be presented when  $B_2$  is oscillating only. Since the model is linearized, the superposition principle holds and the results may be added to describe the behaviour when the inlet concentrations of A and  $B_2$  are oscillating simultaneously.

### Oscillating the inlet concentration of A only

In Figure 3.5 the gain of the gas phase concentrations is shown when  $C_A$  is used as input. The oscillation of the gas phase concentrations of both  $B_2$  and C is a result of the oscillating surface reaction rate. The dynamic regime starts at 0.1 Hz and ends at 2 Hz meaning that for the determination of the parameters applying frequencies as high as 2 Hz is sufficient. Due to mixing in the gas phase only the sliding regime would start at 10 Hz since the residence time can then be considered as the characteristic response time of the reactor. Clearly the catalyst surface plays an important role in the dynamics of the reactor since the sliding regime is already entered at 2 Hz. It should be noticed that the bandwidth not only depends on the kinetic parameters but also on  $\tau_R$  and  $C_{NM}$ . Hence, these parameters should be selected properly in order to avoid mixing in the gas

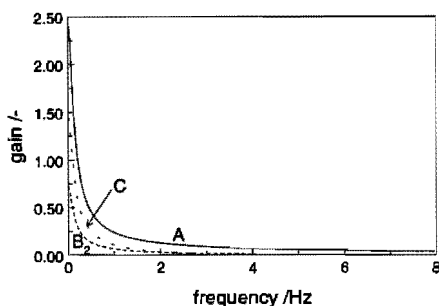


**Figure 3.5**  
The gain of the outlet concentrations of the CSTR versus the frequency. Parameters: Table 3.2; input = A; output: (—) = A; (···) =  $B_2$ ; (---) = C.

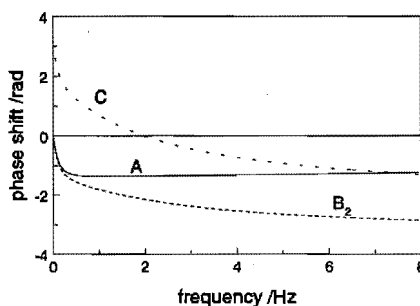


**Figure 3.6**  
The phase shift of the outlet concentrations of the CSTR versus the frequency. Parameters: Table 3.2; input = A; output: (—) = A; (···) =  $B_2$ ; (---) = C.

phase becoming the slowest mechanism and therefore the main determining factor for the dynamic behaviour. This means that  $\tau_R$  should be small compared to the characteristic response time of the occurring reaction and  $C_{NM}$  should be large compared to the time average outlet concentration of A.

In the quasi-steady regime, the system can be considered as being in steady state and consequently the ratio of  $k_2$  and  $K_1^2$  can be determined only (see Equation 3.22). In the sliding regime the small amplitude of A leads to almost time independent adsorbed species and consequently constant concentrations of C and  $B_2$ . Although the kinetic parameters shown in Table 3.2 suggest a much higher frequency needed to enter the sliding regime, such a high frequency is not necessary because of the properly selected values of  $\tau_R$  and  $C_{NM}$ .

As shown in Figure 3.6,  $B_2$  oscillates at low frequencies in phase with A whereas the phase shift of C starts at  $\pi$ . This is caused by the out-of-phase oscillation of the surface reaction due to negative order of the overall rate in the concentration of A, see Equation 3.22. Higher concentrations of A lead to lower reaction rates and consequently higher concentrations of  $B_2$  and lower concentrations of C. In the dynamic regime, above 0.5 Hz, the phase shift of A becomes independent of the frequency, whereas the phase lead of C turns into a phase lag for frequencies above 3 Hz. At even higher frequencies, transition from the dynamic to the sliding regime occurs and the phase shift of all concentrations becomes negative with respect to the inlet concentration. The limit values of the phase shift amount to  $\pi$  for both  $B_2$  and C, and to  $-\pi/2$  for A. The behaviour of the phase shift phase is not only determined by mixing in the gas phase but also by the reaction kinetics, as in case of mixing in the gas being the main dynamic process the dependency of the frequency would be similar for all three components.

### Oscillating the inlet concentration of $B_2$ only

The results when the inlet concentration of  $B_2$  is oscillating only, are shown in Figures 3.7 and 3.8. Compared to the previously discussed situation, *i.e.* oscillating the input concentration of A only, the frequency dependence of the gain of  $B_2$ , see Figure 3.7, differs from that of A, see Figure 3.5. The gain of  $B_2$  exhibits resonance at 0.5 Hz whereas the gain of A decreases monotonously. Apparently the irreversible dissociative adsorption of  $B_2$  leads to this behaviour. The broader bandwidth of  $B_2$  can be explained assuming less interaction between the gas phase and the catalyst surface (see parameters in Table 3.2). For frequencies above 4 Hz, the amplitudes of both A and C approach zero meaning that the adsorbed species oscillate with a very small amplitude. As there is no time dependent interaction with the surface anymore mixing in the gas phase becomes the most important dynamic mechanism and, hence, no kinetic information is available at the outlet.

The oscillation of A is initially out-of-phase with respect to the inlet, as shown in Figure 3.8, while the gas phase concentration of C is always behind in phase. In the quasi-steady state regime the in-phase oscillation of the reaction rate leads to an out-of-phase oscillation of A and an in-phase oscillation of C. The phase shift of  $B_2$  starts at zero and increases very rapidly as a function of the frequency. After passing the maximum, the effects of mixing in the gas on the dynamic behaviour becomes more important and the phase lead turns into phase lag.

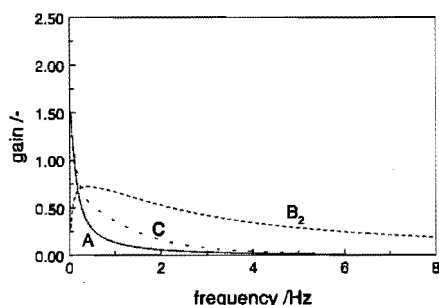


**Figure 3.7**

**The gain of the outlet concentrations of the CSTR versus the frequency.** Parameters: Table 3.2; input =  $B_2$ ; output: (—) = A; (---) =  $B_2$ ; (···) = C.

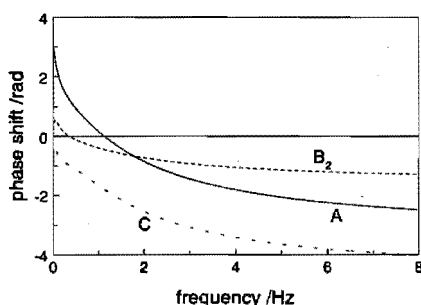


**Figure 3.8**

**The phase shift of the outlet concentrations of the CSTR versus the frequency.** Parameters: Table 3.2; input =  $B_2$ ; output: (—) = A; (---) =  $B_2$ ; (···) = C.

### 3.4.3 Three-step mechanism in a plug flow reactor

The model for the plug flow reactor consists of continuity equations for the species on the catalyst surface, which are the same as in the example of the CSTR Equations 3.19 to 3.21, and continuity equations for the components in the gas phase given by:

$$\frac{\partial C_A}{\partial t} = -v \frac{\partial C_A}{\partial x} - C_{NM}(k_1 C_A \theta_s - k_{-1} \theta_A) \quad (3.27)$$

$$\frac{\partial C_{B_2}}{\partial t} = -v \frac{\partial C_{B_2}}{\partial x} - C_{NM} k_2 C_{B_2} \theta_s^2 \quad (3.28)$$

$$\frac{\partial C_C}{\partial t} = -v \frac{\partial C_C}{\partial x} + C_{NM} k_3 \theta_A \theta_B \quad (3.29)$$

The initial conditions are now given by the steady state profiles:

$$\begin{aligned} C_i(x,0) &= C_i^{ss}(x), \quad i = A, B_2, C \\ \theta_j(x,0) &= \theta_j^{ss}(x), \quad j = A, B, C \end{aligned} \quad (3.30)$$

They are calculated setting the accumulation terms to zero and solving the coupled set of ordinary differential and algebraic equations numerically using NAG routine D02NHF (NAG, 1995). The boundary conditions are given by the inlet concentrations:

$$C_i(0,t) = C_i^{in}(t), \quad i = A, B_2, C \quad (3.31)$$

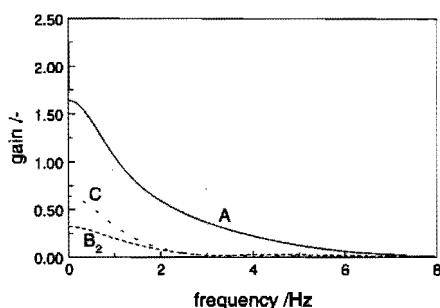
After linearization of the model equations they are transferred to the frequency domain. Due to the complexity of the equations, the gain and the phase shift are determined numerically. The linearization process itself and the numerical methods applied to calculate the gain and the phase shift are described in more detail in appendix 3B.

### Oscillating the inlet concentration of A only

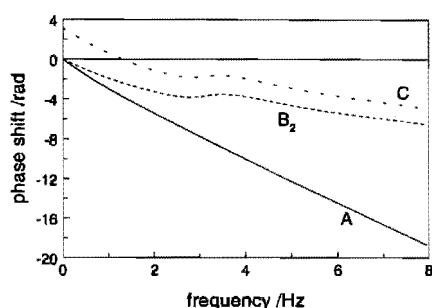
In Figures 3.9 and 3.10, the gain and the phase shift are shown respectively, when the inlet concentration of A is oscillating only. The behaviour depicted in Figure 3.9 is in line with the results of the CSTR. The oscillation of both  $B_2$  and C is a result of the oscillating reaction rate due to the time dependent surface coverages. Compared to the CSTR, Figure 3.5, the bandwidth of the system is larger as the dynamic behaviour is determined by the kinetics only. Although there is no mixing in the gas phase, the amplitude of A becomes very small in the sliding regime.

Figure 3.10 shows that the phase shift of C initially amounts to  $\pi$ , but decreases rapidly as a function of the frequency. This phase lead is caused by a global reaction rate being proportional to the reciprocal of the concentration of A, as already mentioned in section 3.4.2. The frequency dependence of the phase shift of A is not only a result of the residence time but also of the interaction between the gas phase and the catalyst surface. The frequency dependence of the phase shift of both  $B_2$  and C differs from that of A and contains kinetic information since it is not proportional to the frequency.





**Figure 3.9**  
**Gain of the outlet concentrations of the plug flow reactor versus frequency.** Parameters: Table 3.2; input: A; output: (—) = A; (---) =  $B_2$ ; (···) = C.



**Figure 3.10**  
**Phase shift of the outlet concentrations of the plug flow reactor versus frequency.** Parameters: Table 3.2; input: A; output: (—) = A; (---) =  $B_2$ ; (···) = C.

### Oscillating the inlet concentration of $B_2$

As shown in Figure 3.11, the amplitude of  $B_2$  increases during the transition from the quasi-steady regime to the dynamic regime and remains constant for frequencies above 4 Hz. Initially the behaviour is similar to the behaviour of the CSTR, see Figure 3.7, but the amplitude does not decrease for higher frequencies due to the absence of the mixing in the gas phase. The behaviour of the gain of both A and C as a function of the frequency is more pronounced and contains more information about the reaction mechanism than that of  $B_2$ .

In Figure 3.12 the phase shift is depicted as a function of the frequency. A oscillates out-of-phase with respect to both  $B_2$  and C in the quasi-steady state regime. The frequency dependence of the phase shift of  $B_2$  is almost completely determined by the residence time and contains hardly kinetic information. Above 6 Hz the phase shift of all components is a result of the gas flow through the reactor only. The fast decreasing phase shift of A before entering the sliding regime is mainly caused by the interaction between the gas phase and the catalyst surface.

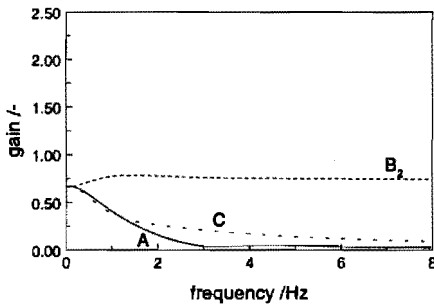


**Figure 3.11**

**Gain of the outlet concentrations of the plug flow reactor versus frequency.** Parameters: Table 3.2; input:  $B_2$ ; output: (—) = A; (---) =  $B_2$ ; (···) = C

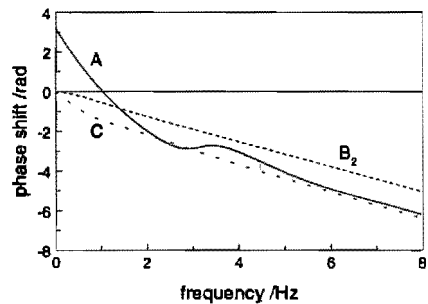


**Figure 3.12**

**Phase shift of the outlet concentrations of the plug flow reactor vs frequency.** Parameters: Table 3.2; input:  $B_2$ ; output: (—) = A; (---) =  $B_2$ ; (···) = C

### 3.4.4 Parameter sensitivity analysis

When applying a frequency response analysis, the kinetic parameters are estimated by regression of the measured gain and phase shift with the corresponding mathematical expressions. To determine the accessibility of the parameters, the values of the kinetic parameter given in Table 3.2 are increased 10%.  $k_1$  and  $k_2$  are changed simultaneously, hence keeping a constant sorption coefficient, whereas the other parameters are changed one at the time. The frequency response equations are solved using these new parameters and the deviation from the gain and the phase shift of both the CSTR and the plug flow reactor are compared as a function of the frequency. The changes are defined by the difference of the gain and phase shift calculated with the parameters given in Table 3.2 and the gain and phase shift calculated with the adapted parameters.

The process considered in the examples is a MIMO system since there are two input variables and three output variables, and therefore the dynamic behaviour is described by six transfer functions. This implies that the parameters can be determined by regression of six measured gains and six measured phase shifts with the corresponding expressions. Hence, another purpose of the parameter sensitivity analysis is to show which of these expressions reveal most information about the parameters. The figures shown in this section depict a selection of all possible gains and

phase shifts. The selection criterion was that all parameters must be accessible, i.e. the gain and the phase shift must be affected by the parameters significantly and the effects of the individual parameter changes must not cancel out when all parameters are varied simultaneously. For small adaptations of the kinetic parameters, the gain and phase are affected linearly and the superposition principle holds. Therefore, the effects as a result of changing all parameters simultaneously are the summation of the effects when one parameter only is changed. The deviations of the gain and the phase shift are calculated for increasing parameter values only, since decreasing the parameters leads to the opposite effects.

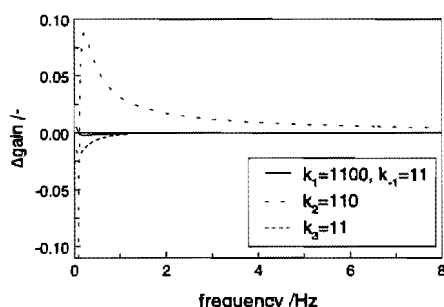


**Figure 3.13**

**Deviation of the gain of the outlet concentrations of the CSTR versus the frequency due to a 10% increase of the parameters given in Table 3.2. Input = A; output = A. Parameter variation: (—) =  $k_1$ ,  $k_{-1}$ ; (---) =  $k_2$ ; (···) =  $k_3$ .**

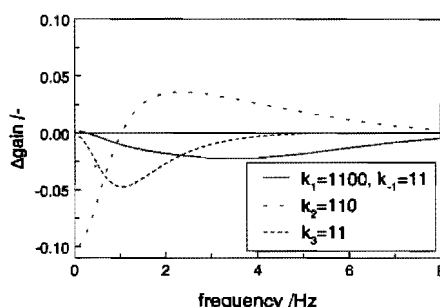


**Figure 3.14**

**Deviation of the gain of the outlet concentrations of the plug flow reactor versus the frequency due to a 10% increase of the parameters given in Table 3.2. Input = A; output = A. Parameter variation: (—) =  $k_1$ ,  $k_{-1}$ ; (···) =  $k_2$ ; (---) =  $k_3$ .**

As shown in Figure 3.13, the gain of the CSTR is strongly dependent on the value of  $k_2$ . However, the gain is rather independent of the value of the sorption equilibrium coefficient  $k_1/k_{-1}$ , meaning that adsorption of A is almost in equilibrium with the gas phase, and independent of the value of  $k_3$ . This is confirmed by calculations performed with different values of  $k_1/k_{-1}$  showing that the gain is affected by the individual parameter variations. The other gains are all less affected by the parameter variations and therefore it is not necessary to include them in the regression. This is also an indication that the outlet variables are coupled meaning that the gains are dependent on each other.

The amplitude at the outlet of the plug flow reactor depends more strongly on the kinetic parameters, as depicted in Figure 3.14. The accessibility of the parameters in the

quasi-steady state regime is comparable with the CSTR, but during dynamic operation the benefits of the plug flow reactor become clear. In the quasi-steady state regime parameter  $k_2$  can be estimated while at a frequency of 1 Hz much information about  $k_3$  is available at the outlet of the reactor. In contrast to the CSTR the value of  $k_1$  and  $k_4$  can be estimated separately and almost the complete frequency range is usable. Figure 3.14 is a good example of the benefits of performing dynamic experiments over a broad range of frequencies. As a function of the applied frequency, the contribution of one distinct parameter to the dynamic behaviour becomes more important than that of the other parameters. Therefore the effects do not cancel out and all parameters can be estimated.

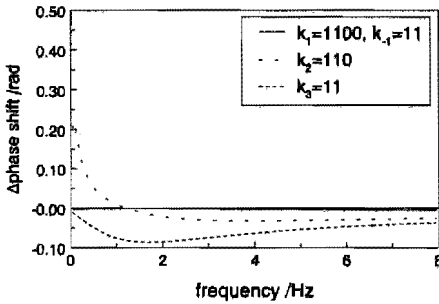


**Figure 3.15**

**Deviation of the phase shift of the outlet concentrations of the CSTR versus the frequency due to a 10% increase of the parameters given in Table 3.2. Input =  $B_2$ ; output = A. Parameter variation: (—) =  $k_1$ ,  $k_4$ ; (---) =  $k_2$ ; (- -) =  $k_3$ .**

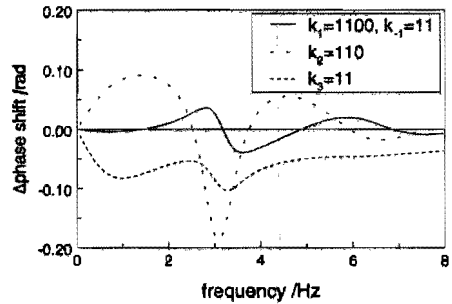


**Figure 3.16**

**Deviation of the phase shift of the outlet concentrations of the plug flow reactor versus the frequency due to a 10% increase of the parameters given in Table 3.2. Input =  $B_2$ ; output = A. Parameter variation: (—) =  $k_1$ ,  $k_4$ ; (---) =  $k_2$ ; (- -) =  $k_3$ .**

The deviation of the phase shift between  $B_2$  and A due to the variation of the parameters is shown in Figure 3.15. Notice that the input and output are different from those in Figures 3.13 and 3.14. In the quasi-steady state regime the dependency of  $k_2$  on the phase shift is very distinct. The contribution of  $k_3$  to the phase shift becomes significant at a frequency of about 2 Hz. By modifying the values of both  $k_1$  and  $k_4$  simultaneously the phase shift is not changed. The trends depicted in this figure are in line with the ones shown in Figure 3.13.

Compared to the results of the CSTR, the phase shift of the plug flow reactor reveals much more kinetic information, as shown in Figure 3.16. The effects of the individual parameter variations do not cancel out and the values of all parameters can

be estimated.

### 3.5 Conclusions

In this chapter the application of the frequency response analysis for the determination of kinetic parameters has been studied. Two examples in both a CSTR and a plug flow reactor have been used to demonstrate the benefits of dynamic reactor operation compared to steady state operation when estimating kinetic parameters. The results of the two reactor types are compared to each other using a parameter sensitivity analysis. The examples showed that a frequency response analysis is applicable in the determination of kinetic parameters in continuous flow reactors. The analysis also showed that a plug flow reactor is more suitable for the estimation of the parameters due to the absence of mixing in the gas phase.

The examples, taking into account adsorption and desorption only, show that in the CSTR the sorption equilibrium coefficient can be estimated only, while in the plug flow reactor the parameter values of adsorption and desorption rate are accessible.

Application of the frequency response analysis to a reaction mechanism taking into account adsorption, desorption and surface shows that the same kinetic information is available at the outlet of the CSTR as during steady state reactor operation. The parameter of the rate determining step and the equilibrium constant can be estimated only. When the reaction is studied in a plug flow reactor, all parameters can be estimated. Both the gain and the phase shift contain detailed information about the kinetic parameters.

It is also beneficial to apply the frequency response method in case of reactions with a different behaviour. In order to determine the optimal experimental conditions a parameter sensitivity analysis has to be performed for all separate cases. However, the dynamics of the CSTR will always be determined by both mixing in the gas phase and the kinetics of the reaction to be studied and, hence, a plug flow reactor is preferably used in estimating kinetic parameters.

### References

- Bailey, J.E., Periodic phenomena, in: Chemical reactor theory: a review, by Lapidus, L and Amundson, N.R., Prentice-Hall, Englewood Cliffs, New York, 758-813, 1971
- Jordi, R.G., Do, D.G., Analysis of the frequency response method for sorption kinetics in bidispersed structured sorbents, *Chem.Eng.Sci.*, **48**, 1103-1130, 1993
- Jordi, R.G., Do, D.G., Analysis of the frequency response method applied to non-

- isothermal sorption studies , *Chem.Eng.Sci.*, **49**, 957-979, 1994
- Kramers, H., Alberda, G., Frequency response analysis of continuous flow systems, *Chem.Eng.Sci.*, **2** 173-181, 1953
  - Li, Y-E, Willcox, D., Gonzalez, R.D., Determination of rate constants by the frequency response method: CO on Pt/SiO<sub>2</sub>, *AIChE*, **35**, 423-428, 1989
  - Lynch, D.T., Walters, N.P., frequency response characterization of reaction systems: external recycle reactor with a solid adsorbent, *Chem.Eng.Sci.*, **45**, 1089-1096, 1990
  - Madix, R.J., Schwarz, J.A., Chemical relaxation molecular beam studies of reactive gas-solid scattering: I. reaction of silicon and germanium with molecular chlorine, *Surf.Sci.*, **24**, 264-287, 1971a
  - Madix, R.J., Parks, R., Susu, A.A., Schwarz, J.A., Chemical relaxation molecular beam studies of reactive gas-solid scattering: II. reaction of ozone with heated germanium surfaces, *Surf.Sci.*, **24**, 288-301, 1971b
  - Marcelin, G., Lester, J.E., Mitchell, S.F., Frequency response study of the effect of alkali promotion on Rh/TiO<sub>2</sub> catalysts: evidence for kinetically distinct H<sub>2</sub>-sorbing sites, *J.Catal.*, **102**, 240-248, 1986
  - Matros, Y.S., Catalytic processes under unsteady-state conditions, *Studies in surface science and catalysis*, **43**, Elsevier, Amsterdam, 1989
  - NAG Fortran Library Manual, mark 16, volume 1, 1995
  - Naphtali, L., Polinski, L., Dynamic methods for characterization of adsorption properties of solid catalysts, *Adv.Catal.*, **19**, 241-291, 1969
  - Renken, A., Unsteady state operation of continuous reactors, *Int.Chem.Eng.*, **24**, 202-213, 1984
  - Schrieffer, J.R., Sinfelt, J.H., Frequency response analysis of surface reactions in flow systems, *J.Phys.Chem.*, **94**, 1047-1050, 1990
  - Schwarz, J.A., Madix, review paper: Modulated beam relaxation spectrometry: its application to the study of heterogeneous kinetics, *Surf.Sci.*, **46**, 317-341, 1974
  - Schwartz, J.P., Sawin, H.H., Hatton, A.T., Frequency response analysis of nonsuperimposable systems using a pseudo-transferfunction: application to systems with coverage-dependent adsorption, *Chem.Eng.Sci.*, **41**, 495-510, 1986
  - Sun, L.M., Bourdin, V., Measurement of intracrystalline diffusion by the frequency response method: analysis and interpretation of bimodal response curves, *Chem.Eng.Sci.*, **48**, 3783-3793, 1993
  - Sun, L.M., Meunier, F., Grenier, Ph., Ruthven, D.M., Frequency response for nonisothermal adsorption in biporous pellets, *Chem.Eng.Sci.*, **49**, 373-381, 1994
  - Yasuda, Y., Saeki, M., Kinetic details of a gas-surface system by the frequency response method, *J.Phys.Chem.*, **82**, 74-80, 1978
  - Yasuda, Y., Determination of vapor diffusion coefficients in zeolite by the frequency response method, *J.Phys.Chem.*, **86**, 1913-1917, 1982

- Yasuda, Y., A frequency response technique to study zeolitic diffusion of gases, *J.Catal.*, **88**, 530-534, 1984
- Yasuda, Y., Yamamoto, A., Zeolitic diffusivities of hydrocarbons by the frequency response method, *J.Catal.*, **93**, 176-181, 1985
- Yasuda, Y, Suzuki, Y., Fukada, H., Kinetic details of a gas/porous adsorbent system by the frequency response method, *J.Phys.Chem.*, **95**, 2486-2492, 1991
- Yasuda, Y., Frequency response method for investigation of gas/surface dynamic phenomena, *Heter.Chem.Rev.*, **1**, 103-134, 1994

## APPENDIX 3A

---

### Derivation of the frequency response equations for adsorption and desorption in continuous flow reactors

#### Frequency response equations for the CSTR

The continuity equation for component A in the gas phase is given by:

$$\frac{dC_A}{dt} = \frac{1}{\tau_R} (C_A^{in} - C_A) - C_{NM} (k_1 C_A \theta_* - k_{-1} \theta_A) \quad (3A.1)$$

and the for species A\* on the catalyst surface by:

$$\frac{d\theta_A}{dt} = k_1 C_A \theta_* - k_{-1} \theta_A \quad (3A.2)$$

where the balance of the active sites is given by:

$$1 = \theta_A + \theta_* \quad (3A.3)$$

The steady state surface coverage is calculated by setting the accumulation term of Equation 3A.2 to zero and eliminating  $\theta_*$  using Equation 3A.3:

$$\theta_A^{ss} = \frac{k_1 C_A^{ss}}{k_1 C_A^{ss} + k_{-1}} \quad (3A.4)$$

The expressions are linearized around the steady state using:

$$C_A(t) = C_A^{ss} + \Delta C_A(t), \quad \theta_A(t) = \theta_A^{ss} + \Delta \theta_A(t) \quad (3A.5)$$

After substitution of the expressions given in Equation 3A.5 into Equations 3A.1 to 3A.3 and using Equations 3A.4 to eliminate  $\theta_A^{ss}$  the following differential equations are obtained:



$$\begin{aligned} \frac{d(C_A^{ss} + \Delta C_A)}{dt} = & \frac{1}{\tau_R} (C_A^{ss,in} - C_A^{ss}) - C_{NM} [k_1 C_A^{ss} \theta_A^{ss} - k_{-1} \theta_A^{ss}] + \\ & \frac{1}{\tau_R} (\Delta C_A^{in} - \Delta C_A) - C_{NM} [k_1 (\Delta C_A \theta_A^{ss} - C_A^{ss} \Delta \theta_A) - k_{-1} \Delta \theta_A] + \\ & C_{NM} k_1 \Delta C_A \Delta \theta_A \end{aligned} \quad (3A.6)$$

$$\begin{aligned} \frac{d(\theta_A^{ss} + \Delta \theta_A)}{dt} = & k_1 C_A^{ss} \theta_A^{ss} - k_{-1} \theta_A^{ss} + \\ & k_1 (\Delta C_A \theta_A^{ss} - C_A^{ss} \Delta \theta_A) - k_{-1} \Delta \theta_A - \\ & k_1 \Delta C_A \Delta \theta_A \end{aligned} \quad (3A.7)$$

The first part of the right hand sites of Equations 3A.6 and 3A.7 is the steady state expression and equals zero. After some rearrangements the following set of linear differential equations is obtained:

$$\frac{d\Delta C_A}{dt} = \frac{1}{\tau_R} \Delta C_A^{in} - \frac{1}{\tau_2} \Delta C_A + \frac{C_{NM}}{\tau_1} \Delta \theta_A + O(\Delta^2) \quad (3A.8)$$

$$\frac{d\Delta \theta_A}{dt} = k_1 k_{-1} \tau_1 \Delta C_A - \frac{1}{\tau_1} \Delta \theta_A + O(\Delta^2) \quad (3A.9)$$

where  $\tau_1$  and  $\tau_2$  are given by:

$$\begin{aligned} \tau_1 &= \frac{1}{k_1 C_A^{ss} + k_{-1}} \\ \tau_2 &= \frac{1}{\frac{1}{\tau_R} + C_{NM} k_1 k_{-1} \tau_1} \end{aligned} \quad (3A.10)$$

Application of the Laplace operator results in a set algebraic equations for both the gas phase and the catalyst surface which are solved with respect to the Laplace transform of  $\Delta C_A$  and  $\Delta \theta_A$ . After transformation to the frequency domain using  $s = i\omega$ , where  $i = \sqrt{-1}$ , the following expressions for the gain and the phase shift are obtained:

$$|H(\omega)| = \frac{1}{\tau_R} \sqrt{\frac{(1 + \omega^2 \tau_1^2) \tau_2^2}{\tau_2^2 \tau_1^2 \omega^4 + (2C_{NM} \tau_2^2 k_1 k_{-1} \tau_1^2 + \tau_1^2 + \tau_2^2) \omega^2 + (1 - C_{NM} \tau_2^2 k_1 k_{-1} \tau_1)^2}} \quad (3A.11)$$

$$\phi = \arctan \left( \frac{\omega \tau_2 (1 + C_{NM} k_1 k_{-1} \tau_1^2 + \omega^2 \tau_1^2)}{C_{NM} k_1 k_{-1} \tau_1 \tau_2 - \omega^2 \tau_1^2 - 1} \right) \quad (3A.12)$$

### Frequency response equations for the PFR

The continuity equations for component A in the gas phase and species on the catalyst surface are given by:

$$\frac{\partial C_A}{\partial t} = -v \frac{\partial C_A}{\partial x} - C_{NM} (k_1 C_A \theta_* - k_{-1} \theta_A) \quad (3A.13)$$

$$\frac{\partial \theta_A}{\partial t} = k_1 C_A \theta_* - k_{-1} \theta_A \quad (3A.14)$$

where the expression for  $\theta_*$  is be obtained from Equation 3A.3.

The expressions are linearized around the steady state using:

$$C_A(x,t) = C_A^{ss} + \Delta C_A(x,t), \quad \theta_A(x,t) = \theta_A^{ss} + \Delta \theta_A(x,t) \quad (3A.15)$$

After substitution of the expressions given in Equation 3A.15 into the continuity equations and elimination of second terms in  $\Delta$  the frequency response equations are given by:

$$\frac{\partial \Delta C_A}{\partial t} = -v \frac{\partial \Delta C_A}{\partial x} - C_{NM} k_1 \theta_*^{ss} \Delta C_A + \frac{C_{NM}}{\tau_1} \Delta \theta_A + O(\Delta^2) \quad (3A.16)$$

$$\frac{\partial \Delta \theta_A}{\partial t} = k_1 \theta_*^{ss} \Delta C_A - \frac{1}{\tau_1} \Delta \theta_A + O(\Delta^2) \quad (3A.17)$$

where  $\tau_1$  is given by Equation 3A.10.

The differential Equations 3A.16 and 3A.17 are transformed to the Laplace domain and  $\theta^{ss}$  and  $\Delta\theta_A$  are eliminated from Equations 3A.16. The resulting ordinary differential equation is solved and expressions for the gain and the phase shift are derived by the transformation to the frequency domain.

## APPENDIX 3B

---

### Derivation of the frequency response equations for the three-step mechanism in continuous flow reactors

#### CSTR

The model consists of balances for the components in the gas phase and the catalyst surface. The continuity equations of components A, B<sub>2</sub> and C in the gas phase are:

$$\frac{dC_A}{dt} = \frac{1}{\tau_R} (C_A^{in} - C_A) - C_{NM} (k_1 C_A \theta_A - k_{-1} \theta_A) \quad (3B.1)$$

$$\frac{dC_B}{dt} = \frac{1}{\tau_R} (C_B^{in} - C_B) - C_{NM} k_2 C_B \theta_A^2 \quad (3B.2)$$

$$\frac{dC_C}{dt} = \frac{1}{\tau_R} (C_C^{in} - C_C) + C_{NM} k_3 \theta_A \theta_B \quad (3B.3)$$

The surface coverages are calculated solving the balances of the species on the catalyst surface given by:

$$\frac{\partial \theta_A}{\partial t} = k_1 C_A \theta_A - k_{-1} \theta_A - k_3 \theta_A \theta_B \quad (3B.4)$$

$$\frac{\partial \theta_B}{\partial t} = 2k_2 C_B \theta_A^2 - k_3 \theta_A \theta_B \quad (3B.5)$$

where  $\theta_*$  is defined by:

$$\theta_* = 1 - \theta_A - \theta_B \quad (3B.6)$$

The equations are linearized around the steady state and transformed to the Laplace domain and the resulting set of algebraic equations as a function of the Laplace operator  $s$  are solved with respect to the depend variables using Maple V<sup>1</sup>. The transformation to the frequency domain as well as the derivation of the expressions for the gain and the phase shift is also performed by Maple V. These expressions are not presented since they are too complicated without giving more insight in the dynamic behaviour of the reactor.

### Plug flow reactor

The model consists of balances for the catalyst surface, which are the same as in the example of the CSTR Equations 3B.4 and 3B.5 and continuity equations for the gas phase, given by:

$$\frac{\partial C_A}{\partial t} = -v \frac{\partial C_A}{\partial x} - C_{NM}(k_1 C_A \theta_* - k_{-1} \theta_A) \quad (3B.7)$$

$$\frac{\partial C_{B_2}}{\partial t} = -v \frac{\partial C_{B_2}}{\partial x} - C_{NM} k_2 C_{B_2} \theta_*^2 \quad (3B.8)$$

$$\frac{\partial C_C}{\partial t} = -v \frac{\partial C_C}{\partial x} + C_{NM} k_3 \theta_A \theta_B \quad (3B.9)$$

The same approach as in the case of CSTR is used to solved the equations. After transformation to the frequency domain, the ordinary differential equations which describe the dynamic behaviour of the plug flow reactor are solved numerically. The differential equations are split into a real part and an imaginary part using Maple V. After that, the real and imaginary parts of the gas phase balances are solved simultaneously by the application of a variable order, variable step size backward differential formulae (BDF), implemented in NAG-routine D02EBF (NAG, 1995). After integration of the equations, the gain and the phase shift of the gas phase components are calculated.

---

<sup>1</sup> Maple V is computer algebra software which derives analytical solutions of mathematical expressions.



# 4

---

## TRANSIENT KINETICS OF THE CO OXIDATION OVER Pt/ $\gamma$ -Al<sub>2</sub>O<sub>3</sub>

### 4.1 Introduction

The oxidation of CO by oxygen over noble metal catalysts has been the subject of several surface science and kinetic studies during the last decades. Its importance in the automobile exhaust gas control and especially the time-average rate enhancements during periodic operation resulted in publications of a more practical approach for this reaction (Silveston, 1995). Furthermore, the great variety in the observed phenomena caused by the nonlinear behaviour, such as hysteresis associated with steady state multiplicity and autonomous oscillations (Razon and Schmitz, 1986) has drawn the attention of many researchers from a more fundamental point of view.

Most of the steady state studies have been conducted at ultra-high vacuum conditions, but the CO oxidation by oxygen over supported catalysts at atmospheric pressure was found to proceed essentially via the same elementary steps as over single crystals under low pressure (Engel and Ertl, 1979; Boudart and Rumpf 1987; Oh *et al.*, 1986). Hence, kinetic parameters obtained from ultra-high vacuum studies may be used as initial parameters estimates when modelling the experimental data at atmospheric pressure.

Above 100 K the CO chemisorption is assumed to proceed molecularly via a precursor state (Compton, 1991). Oxygen adsorption was found to proceed dissociatively at temperatures above 100 K (Engel and Ertl, 1979; Luntz *et al.*, 1989). Taking into account molecular oxygen adsorption followed by an instantaneous

dissociation (Boudart and Djéga-Mariadassou, 1984) in an elementary step mechanism has proven to be useful in modelling the CO oxidation over platinum catalysts (Oh *et al.*, 1986; Campman, 1996). Significant desorption of oxygen has not been observed at temperatures below 700 K (Engel and Ertl, 1979; Luntz *et al.*, 1989).

The CO<sub>2</sub> formation is assumed to proceed either via a Langmuir-Hinshelwood mechanism or via an Eley-Rideal mechanism between oxygen adatoms and gas phase CO or gas phase oxygen and chemisorbed CO. Although most literature before 1970 explained the observations by the Eley-Rideal mechanism, more recently the Langmuir-Hinshelwood mechanism is favoured. Several investigators used both reaction paths to CO<sub>2</sub> to explain the experimentally found behaviour. Above 450 K, it was found that the observed reaction rate decreases much less with increasing temperature than expected on basis of the Langmuir-Hinshelwood mechanism only (Engel and Ertl, 1979). The Eley-Rideal step is often used to describe this behaviour. In explaining the results of transient experiments the Eley-Rideal step is introduced to describe the CO and CO<sub>2</sub> response after switching the feed from oxygen to CO (Harold and Garske, 1991a). Exposure of an oxygen covered surface to gaseous CO causes a very fast formation of CO<sub>2</sub>, whereas this is not the case if oxygen in the gas phase is exposed to chemisorbed CO. This phenomenon can be explained assuming the CO<sub>2</sub> formation proceeds via both the Langmuir-Hinshelwood and the Eley-Rideal mechanism.

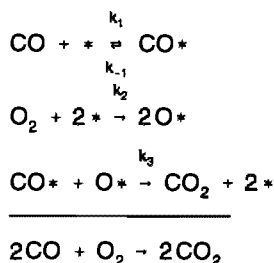
One of the goals of the transient studies conducted is the investigation of the rate enhancement during dynamic operation compared to steady state operation. Cutlip (1979) was among the first who showed that cyclic feeding of CO and oxygen increases the time-average performance of the reactor. Reaction rates up to 40 times higher than the maximum achievable steady state rates were measured by Zhou *et al.* (1984). The explanation of the observed phenomena varies from periodically comparable values of the surface coverages of CO and oxygen (Cutlip, 1979; Cho and West, 1986) to the formation of islands (Zhou *et al.*, 1984; Barshad and Gulari, 1985a) and the reduction of oxides (Zhou and Gulari, 1986). Barshad *et al.* (1985) assumed that the rate enhancement during cyclic feeding of CO is caused by surface species which are not present at steady state operation. A general conclusion of these studies is that the rate enhancement is strongly dependent on the conditions such as temperature, frequency, duty fraction and the amplitude of the oscillation.

Transient studies in combination with Fourier-Transform Infrared Transmission Spectroscopy (Barshad *et al.*, 1985; Barshad and Gulari, 1985b; Li *et al.*, 1987; Prairie *et al.*, 1988; Sant and Wolf, 1990) are often used to clarify reaction mechanisms, since they provide much more information about the reaction mechanism than steady state experiments (Bailey, 1977; Matros, 1989).

Modelling studies of dynamic experiments are rather scarce. Cutlip *et al.* (1982) and Racine and Herz (1992) used the classical three-step kinetic model based on steady state experiments to describe transient experiments. The reaction mechanism



of this classical kinetic model is given by:



One of their conclusions was that the three-step mechanism could not describe both steady state and dynamic behaviour. To model the CO oxidation under dynamic conditions, Racine and Herz (1992) introduced site heterogeneity, while Graham (1993) and Sadhankar and Graham (1994) used a CO exclusion model, *i.e.* they assumed that the maximum value of the CO surface coverage is less than unity, in combination with surface reconstruction to describe the measured responses. Lynch and Graham (1990) showed that CO<sub>2</sub> in the gas phase adsorbs significantly on the catalyst  $\gamma$ -Al<sub>2</sub>O<sub>3</sub> support. This interaction has to be accounted for in modelling dynamic experiments.

The purpose of this study is to model the CO oxidation with cycling of the feed. The conditions are corresponding to exhaust gas conversion before the light off, *i.e.* at a relatively low temperature. The experimental data is used to develop a kinetic model which can describe the measured responses and to estimate the kinetic parameters by means of nonlinear regression analysis (Froment and Hosten, 1981).

## 4.2 Model equations and data analysis

### 4.2.1 Reactor modelling

The total molar flow rate can be assumed to be constant through the bed because of the high dilution of the flow with inert gas. Dynamic experiments conducted with argon showed that the time-scale of mixing in the gas phase is much smaller than the period of the applied oscillation and can therefore be neglected. Furthermore the experimental conditions were chosen to allow the measurement of intrinsic kinetics and the reactor to be considered as isothermal. The fixed bed micro-reactor is, therefore, modelled as an isothermal plug flow reactor. The model consists of continuity equations for the components CO, O<sub>2</sub> and CO<sub>2</sub> in the gas phase, for the species on the catalyst surface and for CO<sub>2</sub> adsorbed on the support. For gas phase component *i*, the continuity equation is expressed as:

$$\frac{\partial C_i(x,t)}{\partial t} + \frac{1}{\tau} \frac{\partial C_i(x,t)}{\partial x} = \sum_k C_k R_{i,k}(x,t) \quad , \quad k = \text{NM or s} \quad (4.1)$$

where  $\tau$  is defined by  $\varepsilon_b A_R / F_{\text{tot}}$ ,  $F_{\text{tot}}$  is the total molar flow rate,  $\varepsilon_b$  the bed porosity and  $A_R$  the cross sectional surface area.  $C_k$  is the ratio of the surface capacity and the capacity of the gas phase in  $\text{mol}/\text{m}_g^3$ , given by:

$$C_k = \frac{L_k \rho_c (1 - \varepsilon_b)}{\varepsilon_b + (1 - \varepsilon_b) \varepsilon_p} \quad , \quad k = \text{NM or s} \quad (4.2)$$

where the parameters are given in Tables 2.1 and 4.1. The continuity equations for both the catalyst surface and the support consist of balances for surface species  $j$  and  $l$  respectively, and are expressed as:

$$\frac{\partial \theta_j(x,t)}{\partial t} = R_j(x,t) \quad , \quad \frac{\partial \zeta_l(x,t)}{\partial t} = R_l(x,t) \quad (4.3)$$

The balances for the active sites are given by:

$$1 = \sum_i \theta_i(x,t) \quad , \quad 1 = \sum_l \zeta_l(x,t) \quad (4.4)$$

The boundary condition of Equation 4.1 depends on time and is given by the inlet concentration:

$$C_i(0,t) = C_i^{\text{in}}(t) \quad , \quad t \geq 0 \quad (4.5)$$

The measured inlet concentrations during the experiment are used as inlet concentrations in the modelling. Using the measured inlet concentrations prevents the calculations from being not comparable with the experimental responses due to the use of different shape of the forcing functions in both the simulations and the experiments.

The initial conditions of the differential equations are given by the steady state solution. For the gas phase concentrations these are:

$$C_i(x,0) = C_i^{\text{ss}}(x) \quad , \quad 0 \leq x \leq L_R \quad (4.6)$$

And for the surface coverages:

$$\theta_j(x,0) = \theta_j^{\text{ss}}(x) \quad , \quad \zeta_l(x,0) = \zeta_l^{\text{ss}}(x) \quad , \quad 0 \leq x \leq L_R \quad (4.7)$$

The production rates  $R_{i,k}$ ,  $R_i$  and  $R_j$  are expressed as a linear combination of the rates of the individual steps of the reaction mechanism and depend on the kinetic parameters which have to be estimated. The reactor parameters are given in Table 4.1.

The model equations are solved using a first order upwind scheme to discretize the spatial derivatives, since there is convection only (Schiesser, 1993). Applying the upwind scheme to the partial differential equations results in set of ordinary differential equations. This set of equations is integrated in time using a variable order and variable step Backward Differentiation Formulae (BDF) method, implemented in NAG routine D02NCF (NAG, 1995). The initial conditions given by Equations 4.6 and 4.7 are determined by setting the accumulation terms of Equations 4.1 and 4.3 to zero and solving the coupled set of ordinary differential equations and algebraic equations by means of NAG routine D02NHF (NAG, 1995). The model equations are solved on a Silicon Graphics Power Challenge. Typical CPU time to integrate over a period of 10 seconds is about 25 seconds.

**Table 4.1**  
**Reactor parameters**

$L_R$	$/m_R$	$10^{-2}$
$A_R$	$/m_R^2$	$1.3 \cdot 10^{-4}$
$\varepsilon_b$	$/m_g^3 m_R^{-3}$	0.3
$L_{NM}^{1)}$	$/mol kg^{-1}_c$	$9.8 \cdot 10^{-3}$
$L_s^{2)}$	$/mol kg^{-1}_c$	0.27
$C_{NM}$	$/mol m^{-3}_g$	11.0
$C_s$	$/mol m^{-3}_g$	302
1) $L_{NM} = \frac{FEW}{M_{NM}}$		
2) $L_s = La_s$ , $L = 1.2 \cdot 10^{-6} mol m^{-2}$ , [Lynch and Graham, 1990].		

#### 4.2.2 Estimation of kinetic parameters

The method of least squares is used to estimate the parameters of the kinetic model. Since the model is nonlinear in its parameters  $\beta$ , the solution is found iteratively using a Marquardt-Levenberg method implemented in Odrpack (1992). The multiresponse explicit ordinary least square problem is defined by:

$$y_i = f_i(x_i; b) - \varepsilon_i \quad i = 1, \dots, n \quad (4.8)$$

where  $n$  is the number of observations per response,  $y_i$  a vector with the  $q$  observed responses which are modelled by  $f_i$ ,  $x_i$  is a vector with the  $m$  independent variables,  $\varepsilon_i$  the errors associated with  $y_i$  and  $b$  the approximated parameters  $\beta$ . The parameters are estimated from the minimization of the multiresponse objective criterion:

$$S(\beta) = \sum_{i=1}^n [f_i(x_i; \beta) - y_i]^T w_{e_i} [f_i(x_i; \beta) - y_i] \rightarrow \min \quad (4.9)$$

Overall, the weights  $w_{e_i}$  are used to eliminate observations and to compensate for unequal variances or correlations in the variable  $y_i$ .

In the regression applied the observed responses are the outlet concentrations, while the independent variables are the inlet concentrations. For the weights the elements of the inverse error covariance matrix are taken. The elements of this matrix are calculated by the regression routine following a first regression with a unity error covariance matrix. To reduce the correlation between the activation energy and the pre-exponential factor reparametrisation of the Arrhenius equation is performed (Kitrell, 1970):

$$k = A^{\#} \exp \left( - \frac{E}{R} \left( \frac{1}{T} - \frac{1}{T_{\text{avg}}} \right) + \frac{\beta \theta_{\text{CO}}}{RT} \right) \quad (4.10)$$

where:

$$A^{\#} = A \exp \left( - \frac{E}{RT_{\text{avg}}} \right) \quad (4.11)$$

and  $T_{\text{avg}}$  the average temperature amounting to 403 K. The surface coverage dependence of the activation energy accounts for the interaction of adsorbed CO molecules and will be explained in more detail in sections 4.4.1 and 4.5. The variance of the original parameters is determined according to:

$$\begin{aligned} \text{var}(A) = \exp \left( \frac{2E}{RT_{\text{avg}}} \right) \text{var}(A^{\#}) + \left( \frac{A}{RT_{\text{avg}}} \right)^2 \text{var}(E) \\ + 2 \frac{A}{RT_{\text{avg}}} \exp \left( \frac{E}{RT_{\text{avg}}} \right) \text{cov}(A^{\#}, E) \end{aligned} \quad (4.12)$$

The parameter estimates were tested for significance by means of their approximate individual t-values. These t-values are used to determine the  $1-\alpha$  confidence interval according to:

$$b_i - t(n - p, 1 - \frac{1}{2}\alpha) s(b_i) \leq \beta_i \leq b_i + t(n - p, 1 - \frac{1}{2}\alpha) s(b_i) \quad (4.13)$$

Using equation 4.12 and 4.13 the t-values and the 95% confidence intervals of the

original parameters can be constructed.

As mentioned before the outlet concentrations of  $\text{CO}$ ,  $\text{O}_2$  and  $\text{CO}_2$  are used as responses in the regression analysis. The experiments performed at a frequency of 0.1 Hz are used in the regression only as higher frequencies eventually lead to axial temperature profiles in the reactor. Final estimates are obtained from regression of data acquired at four temperatures, see Table 4.2. The outlet concentrations at 400 points in time have been used in the regression. The initial values of the parameters are chosen within the range of realistic values summarized in Table 4.4. With good starting values it takes about 14 iterations to reach the final estimates. During the regression of the data the model equations are integrated about 850 times over a period of 10 s which takes about six hours of CPU time on a Silicon Graphics Power Challenge.

## 4.3 Experimental results

### 4.3.1 Experimental conditions

Before the experiments are carried out the catalyst is pre-treated as described in section 2.4.1. After keeping the catalyst under He overnight, the initial activity is higher. Therefore, before starting the cyclic feeding experiment, the steady state activity the catalyst was followed in time and compared with the activity of the day before. After three hours the decay of the production rate was less than 1% per hour and a steady state activity was assumed. It turned out that the catalyst maintained the same activity for months. Hence, all experiments have been carried out with the same catalyst batch. The experimental conditions during the cyclic

**Table 4.2**

**Experimental conditions during the cyclic feeding experiments over  $Pt/\gamma\text{-Al}_2\text{O}_3$**

P	/kPa	110
$P_{\text{CO}}^{1)}$	/kPa	0.55
$P_{\text{O}_2}^{1)}$	/kPa	0.55
T	/K	373 - 433
W	/kg <sub>c</sub>	$1.1 \cdot 10^{-3}$
f	/Hz	0.1 - 0.5
$F_{\text{tot}}^{2)}$	/mol s <sup>-1</sup>	$5.6 \cdot 10^{-3}$

<sup>1)</sup>  $\text{CO}$  and  $\text{O}_2$  oscillate in counter phase;  $\text{CO}$  is fed one half of a period,  $\text{O}_2$  the other half  
<sup>2)</sup>  $F_{\text{tot}}$  includes balance gas He

feeding experiments are summarized in Table 4.2, whereas the steady state conditions during the stabilisation period are given in section 2.4.1.

### 4.3.2 Cyclic feeding

In Figure 4.1 both the measured and the calculated responses are depicted at a temperature of 433 K. The calculated responses result from the regression of the experimental data discussed in section 4.5. The feed stream is periodically switched from 0.5 % CO to 0.5 % O<sub>2</sub> in He with a period of 10 s, see also section 2.4.4. The shift in time between the inlet and the outlet responses due to the residence time amounts to about 100 ms and is not visible at the time resolution shown in Figure 4.1. Although a stable oscillation is reached within 10 seconds, the data recording is started one minute after initiating the oscillation. As the responses are part of a stable oscillation the oxygen and CO adsorption capacities can be calculated by integrating the CO<sub>2</sub> response in time. The amount of CO<sub>2</sub> produced during both the O<sub>2</sub> and CO feeding part of the response amounts to  $1.1 \cdot 10^{-2}$  mol/kg<sub>c</sub> indicating equal CO and O<sub>2</sub> adsorption capacities. As shown in Figure 4.1, the time scales of the responses are of the same order as the period and the reactor is therefore operated in the so-called dynamic

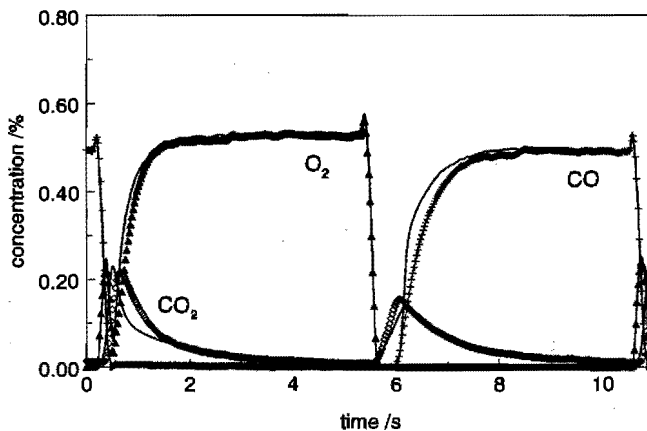


**Figure 4.1**

**Measured and calculated CO, O<sub>2</sub> and CO<sub>2</sub> outlet concentrations versus time during forced cycling of the CO and O<sub>2</sub> concentration. Lines: calculated using Equations 4.1 to 4.7 and 4.17 to 4.20, parameters: Table 4.5. Symbols: measured responses: + = CO; ▲ = O<sub>2</sub>; = CO<sub>2</sub>. Conditions: T = 433 K, f = 0.1 Hz and Table 4.2.**

regime. This is the most interesting regime in the determination of kinetic parameters since the responses contain information about the reaction mechanism which is often

not accessible during steady state operation. In chapter 3 the benefits of dynamic reactor operation compared to steady state operation were discussed with respect to parameter estimation in more detail.

The observed phenomena can be explained as follows. At zero seconds, just before switching the feed stream from CO to oxygen, a steady state is reached. Immediately after switching, a few sites only are available for the adsorption of oxygen and therefore the outlet  $\text{O}_2$  concentration tends to follow the inlet. After an induction time of about 0.2 s the surface reaction between adsorbed oxygen and adsorbed CO starts and  $\text{CO}_2$  is detected at the outlet. As a result of the surface reaction new vacant sites are created and more oxygen adsorbs on the catalyst surface. This autocatalytic effect leads to the rapid decrease of the  $\text{O}_2$  concentration, shown in Figure 4.1. When most of the adsorbed CO has reacted, the  $\text{CO}_2$  production rate decreases. The oxygen concentration starts then to increase and relaxes to the inlet concentration. When the  $\text{O}_2$  outlet concentration equals the inlet concentration the surface will be completely covered with oxygen adatoms and no  $\text{CO}_2$  formation takes place any more. The transient part of the  $\text{CO}_2$  response after the surface reaction has stopped can be explained by desorption from the support: apparently  $\text{CO}_2$  in the gas phase shows some interaction with the  $\gamma\text{-Al}_2\text{O}_3$  support. From Figure 4.1 it is clear that the time-scale of the  $\text{CO}_2$  desorption is large compared with the time-scale of the surface reaction.

After switching to the feed stream containing CO, the  $\text{CO}_2$  formation starts immediately. During the first half a second no CO is detected at the outlet of the reactor. Although the surface is completely covered with oxygen, CO from the gas phase adsorbs on the surface and reacts with adsorbed adatoms. When CO starts to break through the surface reaction rate and hence the  $\text{CO}_2$  concentration is decreasing. After about three seconds, the CO concentration reaches the steady state while the  $\text{CO}_2$  concentration still decreases. The  $\text{CO}_2$  formation stops when all adsorbed oxygen has reacted; CO adsorbed on the catalyst is then in equilibrium with the gas phase. From Figure 4.1 it can be concluded that CO adsorbs on a surface completely covered with adsorbed oxygen, while the  $\text{O}_2$  adsorption is inhibited by adsorbed CO.

### Effect of temperature

At a temperature of 373 K, the  $\text{O}_2$  concentration follows the inlet signal immediately after switching of the feed streams, as shown in Figure 4.2. Compared to Figure 4.1 the CO desorption rate has decreased due to the lower temperature. Hence, the steady state degree of CO coverage is higher at the end of the CO feeding part of the period. The  $\text{O}_2$  adsorption is even more inhibited by the adsorbed CO and therefore the outlet  $\text{O}_2$  concentration equals the inlet concentration for about half a second. The initially very low surface reaction rate increases rapidly creating more vacant sites for

oxygen starts to adsorb on. When most of adsorbed CO has reacted, the  $O_2$  concentration goes through the local minimum and relaxes to the final value without reaching the inlet concentration. Figure 4.2 shows that the  $O_2$  concentration relaxes on the same time scale to the final value as the  $CO_2$  concentration meaning that the time scale of the  $CO_2$  desorption from support is no longer the slowest step.

When switching to a feed stream containing CO, the response is similar to that shown in Figure 4.1. The  $CO_2$  production starts immediately because the CO adsorption is not inhibited by the adsorbed oxygen. Apparently the reaction path leading to the formation of  $CO_2$  after exposing the catalyst to CO is rather temperature independent. The temperature dependency of the interaction of  $CO_2$  with the support is also negligible under the experimental conditions as the relaxation behaviour in shown Figure 4.1 is similar to that shown in Figure 4.2. This is confirmed by experiments with a cyclic feed containing  $CO_2$  only.

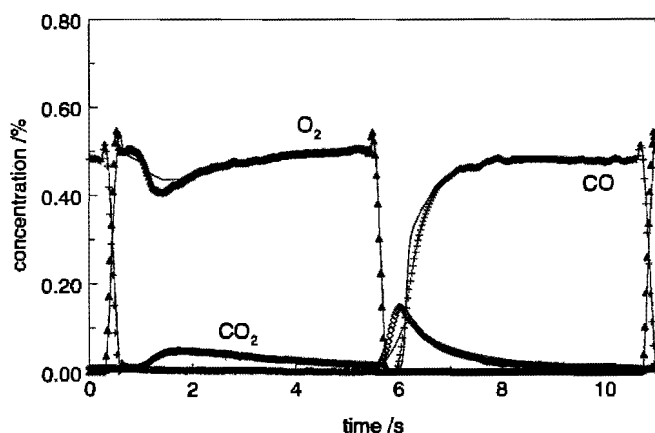


**Figure 4.2**

**Measured and calculated  $CO$ ,  $O_2$  and  $CO_2$  outlet concentrations versus time during forced cycling of the  $CO$  and  $O_2$  concentration. Lines: calculated using Equations 4.1 to 4.7 and 4.17 to 4.20, parameters: Table 4.4. Symbols: measured responses: + =  $CO$ ;  $\Delta$  =  $O_2$ ;  $\square$  =  $CO_2$ . Conditions:  $T = 373\text{ K}$ ,  $f = 0.1\text{ Hz}$  and Table 4.2.**

### Effect of the frequency

At a forcing frequency of 0.5 Hz, a steady state is never reached and  $CO_2$  formation always takes place, as depicted in Figure 4.3. The shape of the response



immediately after switching the feed stream from CO to oxygen is almost similar to the one shown in Figure 4.1. After switching the feed stream to  $\text{O}_2$  only a few vacant adsorption sites are available and the outlet concentration follows the inlet. The local maximum in the oxygen response is lower compared to that in Figure 4.1. As there is always both CO and oxygen present on the surface, the ongoing surface reaction creates extra vacant adsorption sites. Compared to Figure 4.1, these sites are available immediately after switching the feed stream, while at a frequency of 0.1 Hz they are created after some oxygen has adsorbed on the catalyst surface. Since the CO adsorption is not inhibited by adsorbed oxygen, the CO response is similar to that at a frequency of 0.1 Hz, see Figure 4.1. There is still an induction time of the  $\text{CO}_2$  concentration and the  $\text{CO}_2$  starts to increase immediately after switching the feed.

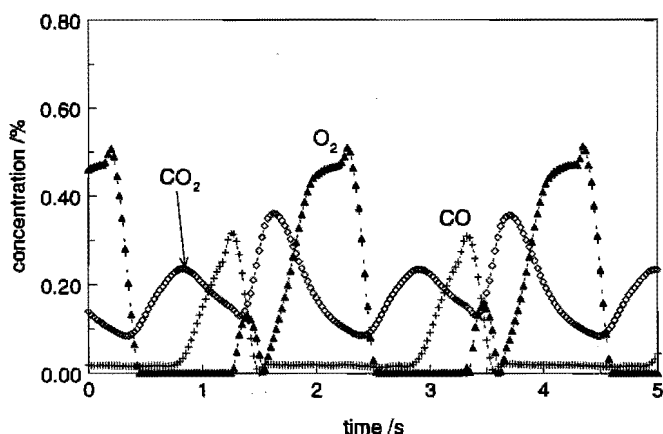


**Figure 4.3**

**Measured  $\text{CO}$ ,  $\text{O}_2$ , and  $\text{CO}_2$  outlet concentrations versus time during forced cycling of the  $\text{CO}$  and  $\text{O}_2$  concentration. Conditions:**

**$T = 433\text{ K}$ ,  $f = 0.5\text{ Hz}$  and Table 4.2.**

### 4.3.3 Effect of frequency and temperature on the time-average conversion

As often reported in literature dynamic reactor operation can result in higher time-average conversions compared to steady state operation. The effects are strongly dependent of the conditions such as the frequency and the temperature. Usually the time-average conversions differ from the steady state conversions due to the nonlinear behaviour of the reactions taking place in the reactor. In Figure 4.4 the time-average

conversions at four temperatures are depicted as a function of the frequency.

The behaviour at a temperature of 373 K is first discussed. At low frequencies, in the quasi-steady regime, the behaviour can be explained considering the amounts of  $\text{CO}_2$  produced per second during feeding oxygen and CO. The total amount of  $\text{CO}_2$  produced after switching the feed streams at low frequencies is determined by the capacity of the catalyst surface only and is independent of the frequency. Hence, the amount of  $\text{CO}_2$  produced per second increases linearly as a function of the frequency which explains the behaviour shown in Figure 4.4.

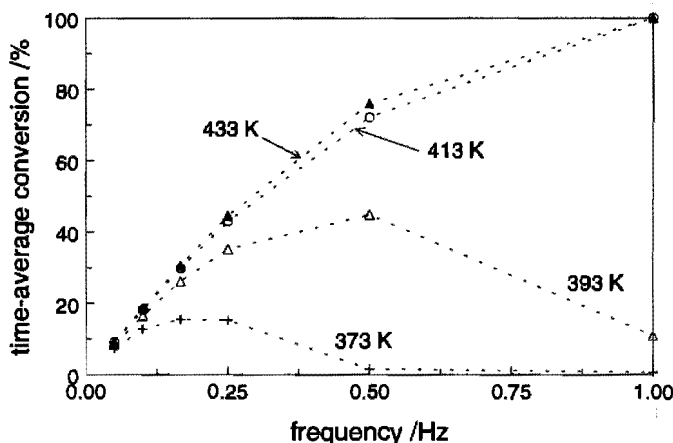


**Figure 4.4**

**Time-average conversion as a function of the frequency at four temperatures: + = 373 K;  $\Delta$  = 393 K;  $\square$  = 413 K;  $\blacktriangle$  = 433 K. Conditions Table 4.2.**

At a higher frequency, the so-called dynamic regime of operation, the reaction takes place during a substantial part of the period and the responses become dependent of the frequency. In contrast to quasi-steady operation the catalyst surface is not completely covered with either CO or oxygen adatoms just before switching the feed streams. The amount of  $\text{CO}_2$  produced during one complete period now depends on the ratio of the time-scale of  $\text{CO}_2$  formation to the period. As the CO adsorption is not inhibited by adsorbed oxygen and not all adsorbed CO reacts within the  $\text{O}_2$  feeding part of the period the surface becomes ever more CO covered with increasing frequency. The resulting lower degree of oxygen coverage leads to a nonlinear increasing time-scale of the surface reaction with increasing frequency due to the nonlinear behaviour of the surface reaction. This means that the ratio time-scale of  $\text{CO}_2$

production to period of the oscillation decreases more than proportional as a function of the frequency and consequently the time-average conversion less than proportional.

In the sliding regime, at relatively high frequencies, the time-average conversion decreases as a function of the frequency. The degree of CO coverage increases ever more while the amplitude of the oscillation decreases leading to a steady state approximation. Higher frequencies result in a surface completely covered with CO as the period is too short for oxygen adsorption to take place significantly.

The behaviour in the quasi-steady state regime is rather temperature independent since the time-average conversion is determined by the adsorption capacity of the catalyst only. As the time-scale of the surface reaction decreases as a function of the temperature the ongoing oscillation of the surface coverage of both CO and  $\text{O}_2$  leads to higher time-average conversions at a higher temperature. At an elevated temperature the higher CO desorption rate leads to more vacant adsorption sites for oxygen and the surface is always covered with both CO and oxygen adatoms. This leads to 100% conversion at high frequencies, as shown in Figure 4.4.

## 4.4 Kinetic model

### 4.4.1 Reaction mechanism

Several studies showed that the classical three-step mechanism based on steady state experiments, consisting of molecular chemisorption of CO, dissociative chemisorption of  $\text{O}_2$  and surface reaction cannot describe data obtained from transient experiments. Often the rate expressions are adapted (Racine and Herz, 1992) or new (elementary) steps are added to the mechanism (Barshad and Gulari, 1985; Harold and Garske, 1991a). The responses as a result of switching the feed stream from CO to oxygen can be described by this kinetic model to some extent, but the model fails completely to predict the responses during the CO feeding part of the period. As shown in both Figure 4.1 and 4.2, the CO chemisorption is not inhibited by chemisorbed oxygen, while the oxygen chemisorption rate is dependent of the degree of coverage by CO.

To model the observed phenomena several solutions can be thought of. Ultra-high vacuum studies show that maximum oxygen coverage is between 0.25 and 0.5 monolayers (Freel, 1972) while the maximum fractional CO coverage is unity. The introduction of *oxygen exclusion* (Herz and Marin, 1980; Lynch, 1984; Harold and Garske, 1991a) accounts for the difference in the CO and the oxygen capacity of the catalyst surface. When the surface is saturated with oxygen, there are still sites available for the CO chemisorption. However, the results of both CO and oxygen chemisorption experiments performed, see section 2.3, and the calculation of the

amount of chemisorbed CO and oxygen by integrating the measured  $\text{CO}_2$  response depicted in Figure 4.1 show that surface coverages of both CO and  $\text{O}_2$  can become unity.

Assuming the  $\text{CO}_2$  formation not only proceeds via a Langmuir-Hinshelwood surface reaction but also via an *Eley-Rideal reaction* between dissociatively chemisorbed oxygen and gas phase CO (Bonzel and Ku, 1973; Harold and Garske, 1991b) can be useful sometimes. In steady state studies the Eley-Rideal step is used to explain the dependency of the CO concentration on the reaction rate at elevated temperatures, while in transient studies it is used to account for the  $\text{CO}_2$  formation after feeding CO to a surface saturated with oxygen. Since the surface is completely covered with oxygen and no other intermediate is involved in the Eley-Rideal reaction, there will be no induction time in the  $\text{CO}_2$  formation other than the residence time after switching the feed stream to CO. As shown in Figure 4.1 and 4.2 a small but significant induction time is visible, so this step can be ruled out.

Huinink (1995) used *CO physisorption* to model the CO oxidation by oxygen over platinum at a pressure of 100 Pa. It was assumed that physisorbed CO is in equilibrium with the gas phase and is followed by CO chemisorption on vacant sites. The  $\text{CO}_2$  response predicted by this model will be the same as the one predicted by the basic Langmuir-Hinshelwood model. Since physisorption occurs on both chemisorbed CO and chemisorbed oxygen the physisorbed CO returns to the gas phase after switching off the CO in the feed. Therefore, the introduction of physisorbed CO results in an extra capacity on top of the chemisorbed species leading to a phase shift of the CO outlet concentration. Hence, taking into account CO physisorption in the kinetic model results not in a better description of the observed responses.

Another alternative to describe the dynamic responses is the *adsorption of CO on platinum oxides* (Barshad and Gulari, 1985; Herz and Shinouskis, 1984; Zhou *et al.*, 1986). Platinum oxides are formed at a time-scale of minutes (Turner and Maple, 1984). The period of the forced oscillation is about one second so the oxide formation is in the sliding regime and consequently the amount of oxides remains almost constant in time. Since no adsorption of oxygen on oxides takes place and the reduction of the oxide also proceeds at a time-scale of minutes, the oxygen adsorption capacity will be smaller than the CO adsorption capacity. As mentioned before, the amount of adsorbed CO equals the amount of adsorbed oxygen. Therefore it can be concluded that the contribution of the reduction of oxides to the  $\text{CO}_2$  formation is negligible.

Several Fourier-Transform Infrared Transmission Spectroscopy (FTIR) studies show that during cyclic feeding the formation of new surface species plays an important role in the CO oxidation (Herz and Shinouskis, 1984; Barshad *et al.*, 1985; Zhou and Gulari, 1986). Barshad *et al.* (1985) suggest that *CO can chemisorb on a catalytic site already covered by chemisorbed oxygen*. During periodic operation new peaks became visible in the time-average IR spectra compared to steady state operation. From these

IR spectra they concluded that CO adsorbs both on oxygen covered sites and platinum oxides. The amount of the latter remained constant at a switching period of about one minute, while the former oscillated with an amplitude of 30%.

Barshad *et al.* (1985) also suggested that CO sharing a site with oxygen is a very reactive intermediate leading to the rate enhancements observed during periodic operation. Based on the above discussion it is assumed in the modelling that CO can

**Table 4.3**

**Elementary steps and reaction paths used to model the cyclic feeding experiments.**

elementary reaction	N1	N2	step number
$CO + * \xrightleftharpoons[k_{-1}]{k_1} CO^*$	2	0	1
$O_2 + * \xrightleftharpoons[k_{-2}]{k_2} O_2^*$	1	1	2
$O_2^* + * \xrightleftharpoons[k_{-3}]{k_3} 2O^*$	1	1	3
$CO^* + O^* \xrightleftharpoons[k_{-4}]{k_4} CO_2 + 2^*$	2	0	4
$CO + O^* \xrightleftharpoons[k_{-5}]{k_5} OCO^*$	0	2	5
$OCO^* \xrightleftharpoons[k_{-6}]{k_6} CO_2 + ^*$	0	2	6
$CO_2 + \ddagger \xrightleftharpoons[k_{-7}]{k_7} CO_2\ddagger$	0	0	7
$2CO + O_2 \rightarrow 2CO_2$			

\* site on Pt

‡ site on  $\gamma$ -Al<sub>2</sub>O<sub>3</sub>

chemisorb on a catalytic site already covered by chemisorbed oxygen, *i.e.* chemisorbed CO and oxygen adatoms can share the same catalytic site.

The elementary steps and the reaction paths considered in the modelling are

listed in Table 4.3. They consist of the basic Langmuir-Hinshelwood kinetic model with molecular oxygen adsorption followed by an instantaneous dissociation (Campman, 1996). These steps are often used to model the observed steady state behaviour. In step 5, the CO chemisorption on a site already covered by oxygen leading to the formation of species  $\text{OCO}^*$  is taken into account. The CO adsorption rate of step 5 is assumed to be proportional to the oxygen surface coverage.  $\text{OCO}^*$  can either desorb from the catalyst surface resulting in chemisorbed oxygen and gaseous CO, or react to  $\text{CO}_2$ , shown in step 6.

As discussed in section 4.3.2,  $\text{CO}_2$  shows some interaction with the support. Therefore it is assumed that  $\text{CO}_2$  adsorbs reversibly on the  $\gamma\text{-Al}_2\text{O}_3$  support, step 7.

The expressions of the rate coefficients of the elementary steps shown in Table 4.3 used in the regression analysis are given by:

#### Chemisorption of CO and $\text{O}_2$

The rate coefficient for the chemisorption of CO and  $\text{O}_2$  are obtained from the collision theory and expressed as:

$$k_i = \frac{1}{L_i} \sqrt{\frac{RT}{2\pi M_i}} s_i^0 \quad (4.14)$$

where  $s_i^0$  refers to the sticking probability on a clean surface. The chemisorption of CO and  $\text{O}_2$  have been reported to be non-activated processes (Engel and Ertl, 1978). It is assumed that the chemisorption of  $\text{O}_2$  is followed by an instantaneous dissociation, and therefore  $k_2$  is set to infinity. This leads to a first order dependence of the chemisorption rate on the fraction of vacant sites  $\theta$ . (Oh *et al.*, 1986) and an overall steady state rate which is proportional to  $P_{\text{O}_2}/P_{\text{CO}}$  (Campman, 1996).

#### Desorption of CO

The CO desorption coefficient is obtained from:

$$k_{-1} = A_{d,\text{CO}} \exp\left(-\frac{E_{d,\text{CO}}^0 - \beta_{d,\text{CO}} \theta_{\text{CO}}}{RT}\right) \quad (4.15)$$

The desorption of CO is assumed to follow the Elovich desorption kinetics (Boudart and Djéga-Mariadassou, 1984; Herz and Marin, 1980; Oh *et al.*, 1986; Zhdanov and Kasemo, 1994). The surface non-uniformity or the interaction of the adsorbed CO molecules, is described by a linear relation between the activation energy and the CO

surface coverage.

### Surface reaction

The coefficient of the surface reaction between  $\text{CO}^*$  and  $\text{O}^*$  is described by:

$$k_4 = A_{\text{LH}} \exp \left( - \frac{E_{\text{LH}}^0 - \beta_{\text{LH}} \theta_{\text{CO}}}{RT} \right) \quad (4.16)$$

The surface non-uniformity is again described by a linear surface coverage dependence of the activation energy (Zhdanov and Kasemo, 1994).

As mentioned in section 4.3.2 the experiments showed that responses as a result of switching the feed stream from oxygen to CO are independent of the temperature. Dynamic experiments performed with feed streams containing  $\text{CO}_2$  only showed that the adsorption and desorption from the support are not significantly dependent of the temperature either. Therefore, the other rate coefficients are assumed to be parameters independent of the temperature.

**Table 4.4**  
**Kinetic parameters of the CO oxidation on Pt as reported in literature.**

parameter	value	reference
$s_{\text{CO}}^0$ /-	0.5	Herz and Marin, 1980
$s_{\text{O}_2}^0$ /-	0.014	Herz and Marin, 1980
$A_{\text{d,CO}}$ / $\text{s}^{-1}$	$10^{14}$ , $10^{17}$ , $10^{13}$	van Santen and Niemandsverdriet, 1992; Zhdanov <i>et al.</i> , 1988; Compton, 1991
$E_{\text{d,CO}}$ / $\text{kJ mol}^{-1}$	124, 130, 112	Herz and Marin, 1980; Compton, 1991, Campman, 1996
$\beta_{\text{d,CO}}$ / $\text{kJ mol}^{-1}$	27.2, 16	Herz and Marin, 1980; Zhdanov and Kasemo, 1994
$A_{\text{LH}}$ / $\text{s}^{-1}$	$10^{13}$ , $2 \cdot 10^6$	Herz and Marin, 1980; Graham, 1993
$E_{\text{LH}}$ / $\text{kJ mol}^{-1}$	56.5, 48.2	Herz and Marin, 1980; Graham, 1993
$\beta_{\text{LH}}$ / $\text{kJ mol}^{-1}$	8.4	Zhdanov and Kasemo, 1994
$k_{\text{a,CO}_2}$ / $\text{m}_g^{-3} \text{mol}^{-1} \text{s}^{-1}$	5.5	Graham, 1993
$k_{\text{d,CO}_2}$ / $\text{s}^{-1}$	27.7	Graham, 1993

In Table 4.4 some parameter values from the literature are shown which are used as initial values in the regression analysis. Before the regression was started, some simulations have been performed using the parameters of Table 4.4. The results of the simulations were compared with the experimental data to determine the best initial values of the parameters for the regression. Simulations performed without  $\beta_{d,CO}$  and  $\beta_{LH}$  showed that it is not possible to describe the transient part of the responses during the part of the period  $O_2$  is fed to the reactor without these parameters. When  $\beta_{d,CO}$  is set to zero the rapid decrease of the  $O_2$  response immediately after switching the feed streams cannot be predicted by the model whereas the relatively slow relaxation of the  $O_2$  response cannot be described without  $\beta_{LH}$ . In modelling steady state experiments in the CO inhibition regime, *i.e.* the surface is always almost completely covered with CO, there is no necessity to introduce the  $\beta$ 's as the degree of CO coverage is independent of the experimental conditions.

#### 4.4.2 Rate expressions

The reaction mechanism shown in Table 4.3 is used to describe the cyclic feeding experiments. From this table expressions of the net production rates of the gas phase components and the surface species are derived which have to be substituted into Equations 4.1 and 4.3. For the gas phase components they are given by:

$$\begin{aligned} R_{CO} &= k_{-1}\theta_{CO} - k_1C_{CO}\theta_* + k_{-5}\theta_{OCO} - k_5C_{CO}\theta_O \\ R_{O_2} &= -k_2C_{O_2}\theta_* \\ R_{CO_2,NM} &= k_4\theta_{CO}\theta_O + k_6\theta_{OCO} \end{aligned} \quad (4.17)$$

and for the species on the platinum surface:

$$\begin{aligned} R_{CO,*} &= k_1C_{CO}\theta_* - k_{-1}\theta_{CO} - k_4\theta_{CO}\theta_O \\ R_{O,*} &= 2k_2C_{O_2}\theta_* - k_4\theta_{CO}\theta_O + k_{-5}\theta_{OCO} - k_5C_{CO}\theta_* \\ R_{OCO,*} &= k_5C_{CO}\theta_O - k_{-5}\theta_{OCO} - k_6\theta_{OCO} \end{aligned} \quad (4.18)$$

For  $CO_2$  on the support the net sorption rate is obtained from:

$$R_{CO_2,s} = k_{-7}\zeta_{CO_2} - k_7C_{CO_2}\zeta_* \quad (4.19)$$

where:

$$\begin{aligned} \theta_* &= 1 - \theta_{CO} - \theta_O - \theta_{OCO} \\ \zeta_* &= 1 - \zeta_{CO_2} \end{aligned} \quad (4.20)$$



The rate equations are a function of the kinetic parameters to be estimated and are substituted into the continuity equations for the components in the gas phase, Equation 4.1, and the continuity equations for the surface species Equation 4.3 (see section 4.2.1). The calculated responses are used in the regression of the experimental data.

## 4.5 Regression results

### 4.5.1 Parameter estimates

The final kinetic parameter estimates with their 95% confidence intervals are shown in Table 4.5. The corresponding t-values range between 5 and 2000 indicating that all parameters estimates are statistically significant. Equation 4.12 is used to reconstruct the t-value corresponding to  $A_{d,\text{CO}}$  and  $A_{\text{LH}}$ . F-value after regression amounts to  $1.3 \cdot 10^3$  while the highest absolute value of the binary correlation coefficient occurred between  $s_{\text{CO}}^0$  and  $A_{\text{LH}}$  amounting to 0.72.

All parameters estimates are well in the range calculated from the transition state theory (Zhdanov *et al.*, 1988) and close to values reported in the literature, see Table 4.4. The sticking probability of CO  $s_{\text{CO}}^0$  on a clean surface is lower than the value reported by Herz and Marin (1980) but much higher than the value reported by Graham (1993), while both the activation energy and the pre-exponential factor of the CO desorption are well in agreement with values found in the literature (Herz and Marin, 1980; Campman, 1996). Estimated value of  $\beta_{d,\text{CO}}$  accounting for the dependency of the activation energy on the degree of coverage, is only half the value reported by Zhdanov and Kasemo (1994) and Oh *et al.* (1986) for the oxidation of CO over  $\text{Rh}/\text{Al}_2\text{O}_3$ . The sticking probability of  $\text{O}_2$  on a clean surface is smaller than the value reported by Herz and Marin (1980). However, Herz and Marin (1980) assumed a second order oxygen adsorption in their kinetic model and this leads to a higher value of  $s_{\text{O}_2}^0$ . Compared to the value of Herz and Marin (1980), the activation energy of the surface reaction is rather low but close to the value reported by Graham (1993), whereas the value of the pre-exponential factor of the surface reaction is in good agreement with the value of Herz and Marin (1980) but smaller than the value as reported by Graham (1993). The value of  $\beta_{\text{LH}}$  is in good agreement with the value of Zhdanov and Kasemo (1994). Graham (1993) reported much higher values for the rate coefficients corresponding to sorption of  $\text{CO}_2$  on the support,  $k_r$  and  $k_{-r}$ . Their values suggest that the  $\text{CO}_2$  adsorption on the support and the desorption from the support takes place on a time-scale of less than 0.1 second. However, the values of the estimates shown in Table 4.5 are in agreement with transient experiments conducted with a feed containing  $\text{CO}_2$  only. These experiments showed that the time-scale of adsorption and desorption is

approximately 1 second. In the literature no values are reported of the parameters of step 5 and 6. However, the parameter estimates of  $k_5$ ,  $k_5$  and  $k_6$  are in line with the observations of Barshad *et al.* (1985). They reported a rather low value of  $\theta_{\text{OCO}}$  and a potentially fast reaction of  $\text{OCO}^*$  to  $\text{CO}_2$ , indicating a relatively low value of the equilibrium constant and a high value of the rate coefficient for the desorption of  $\text{OCO}^*$ ,  $k_6$ .

**Table 4.5**

**Final kinetic parameters estimates with corresponding 95% confidence intervals obtained from regression of data acquired from the cyclic feeding experiments performed under conditions shown in Table 4.2 with the model given by Equations 4.1 to 4.7 and 4.14 to 4.20.**

parameter	value
$s_{\text{CO}}^0$ /-	$2.37 \pm 0.03 \cdot 10^{-1}$
$A_{\text{d,CO}}$ /s <sup>-1</sup>	$2.3 \pm 0.9 \cdot 10^{15}$
$E_{\text{d,CO}}$ /kJ mol <sup>-1</sup>	$124 \pm 1$
$\beta_{\text{d,CO}}$ /kJ mol <sup>-1</sup>	$7.25 \pm 0.08$
$S_{\text{O}_2}^0$ /-	$4.89 \pm 0.04 \cdot 10^{-3}$
$A_{\text{LH}}$ /s <sup>-1</sup>	$4.5 \pm 0.6 \cdot 10^6$
$E_{\text{LH}}$ /kJ mol <sup>-1</sup>	$53.8 \pm 0.4$
$\beta_{\text{LH}}$ /kJ mol <sup>-1</sup>	$11.01 \pm 0.09$
$k_5$ /m <sub>g</sub> <sup>3</sup> mol <sup>-1</sup> s <sup>-1</sup>	$3.76 \pm 0.03 \cdot 10^2$
$k_{-5}$ /s <sup>-1</sup>	$4.56 \pm 0.06 \cdot 10^{-2}$
$k_6$ /s <sup>-1</sup>	$1.86 \pm 0.02$
$k_7$ /m <sub>g</sub> <sup>3</sup> mol <sup>-1</sup> s <sup>-1</sup>	$1.234 \pm 0.001$
$k_{-7}$ /s <sup>-1</sup>	$9.61 \pm 0.09 \cdot 10^{-1}$

#### 4.5.2 Simulations

In Figure 4.1 the measured and the calculated responses are shown at a temperature of 433 K and a forcing frequency of 0.1 Hz. The model describes all responses rather well. Both the local maximum and minimum of the oxygen signal are

described adequately by the model. The calculated induction time of the  $\text{CO}_2$  response after switching the feed stream to oxygen is smaller than that of the measured response, and the  $\text{CO}_2$  concentration relaxes initially on a smaller time-scale to the final value, but the overall description is close to the measured data. The maximum of the calculated  $\text{CO}_2$  response coincides with the minimum in the  $\text{O}_2$  concentration, while in the experimental curves the maximum in the  $\text{CO}_2$  concentration occurs after the minimum of the  $\text{O}_2$  signal. Apparently the  $\text{CO}_2$  formation proceeds via more reaction steps than given in Table 4.3. Both the small induction time of the  $\text{CO}_2$  concentration immediately after switching the feed stream from oxygen to CO and the experimentally observed relatively slow  $\text{CO}_2$  relaxation resulting from desorption from the support are present in the calculated response.

From the transient behaviour of the surface coverages it becomes clear that during the first half of the period the formation of  $\text{CO}_2$  mainly proceeds via step 4 in Table 4.3, while after switching the feed stream to CO the production of  $\text{CO}_2$  takes place via step 6. Simulations performed with step 4 leading to the formation of  $\text{OCO}^*$  instead of  $\text{CO}_2$ , *i.e.* considering only one reaction path in the  $\text{CO}_2$  formation, showed a significantly worse description of the measured responses. Hence, in order to describe a complete period adequately the  $\text{CO}_2$  production must proceed via parallel reaction paths, as shown in Table 4.3. This is in line with the results of several experimental studies reported in the literature showing that the  $\text{CO}_2$  formation over Pt proceeds via parallel paths at different time-scales (Herz and Shinouskis 1984; Barshad and Gulari, 1985; Zhou *et al.*, 1980).

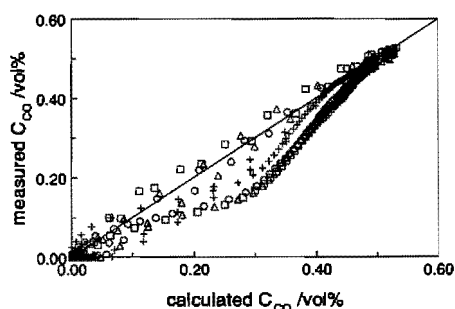


**Figure 4.5**  
**Measured CO outlet concentrations versus concentrations calculated with Equations 4.1 to 4.7 and 4.17 to 4.20, parameters Table 4.5. Symbols: + = 373 K;  $\Delta$  = 393 K;  $\square$  = 413 K;  $\circ$  = 433 K. Conditions: Table 4.2.**

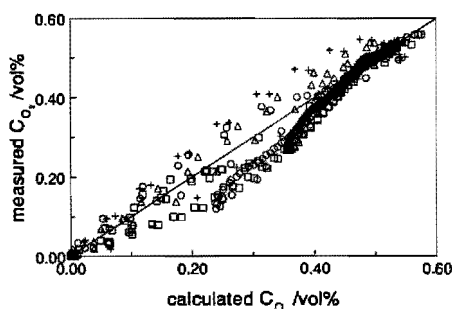


**Figure 4.6**  
**Measured  $\text{O}_2$  outlet concentrations versus concentrations calculated with Equations 4.1 to 4.7 and 4.17 to 4.20, parameters Table 4.5. Symbols: + = 373 K;  $\Delta$  = 393 K;  $\square$  = 413 K;  $\circ$  = 433 K. Conditions: Table 4.2.**

Simulations performed at other experimental conditions showed that the model predicts the dynamic behaviour over a broad range of conditions rather well. An example is shown in Figure 4.2. At 373 K the quality of the model description is comparable with that at a temperature of 433 K, depicted in Figure 4.1. The results at a higher frequency are not shown but are similar to the ones shown in Figure 4.1 and 4.2.

In Figures 4.5 to 4.7 the corresponding parity plots are shown. These figures show that the model describes the measured data rather well over a broad range of inlet concentrations and temperatures. The relatively large deviation from the straight line depicted in Figure 4.7 is mainly caused by the difference between the calculated and the measured response immediately after switching the feed stream from CO to oxygen, see also Figure 4.1.

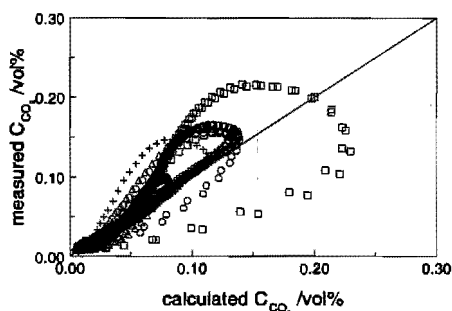


**Figure 4.7**  
**Measured  $\text{CO}_2$  outlet concentrations versus concentrations calculated with Equations 4.1 to 4.7 and 4.17 to 4.20, parameters Table 4.5. Symbols: + = 373 K;  $\Delta$  = 393 K;  $\circ$  = 413 K;  $\square$  = 433 K. Conditions: Table 4.2.**

## 4.6 Steady state simulations

As often reported in the literature, the classical three-step kinetic model, see section 4.1, obtained from steady state experiments cannot describe the measured dynamic responses. However, the same holds for transient kinetic models as they do not predict the observed steady state behaviour. The model of Cutlip (1983) predicts a surface predominantly covered by oxygen which is in contrast to the observations reported in the literature. Under steady state conditions, the model as proposed by Racine and Herz (1992) predicts CO inhibition at relatively low pressures.

To demonstrate the kinetic model obtained from the regression of the data from cyclic feeding experiments can also predict the steady state behaviour, the steady state  $\text{CO}_2$  turnover frequencies as a function of the concentrations are calculated. The accumulation terms of the continuity equations for the species on the surface (Equation 4.3) are set to zero and the set of algebraic equations is solved by means of NAG routine C05NBF (NAG, 1995) for a given gas phase composition. The turnover frequencies as a function of the CO concentration are shown in Figure 4.8 while the

dependency on the oxygen concentration is shown in Figure 4.9. The partial order of the CO concentration at an elevated temperature decreases from 1 to -1 as a function of the CO concentration, as reported by Engel and Ertl (1979). The partial order in the CO inhibition regime of the CO concentration increases from -1 to 0 with decreasing temperature (Berlowitz *et al.*, 1988). The reported dependencies of the partial reaction order in the CO concentration are predicted by the model, as shown in Figure 4.8.

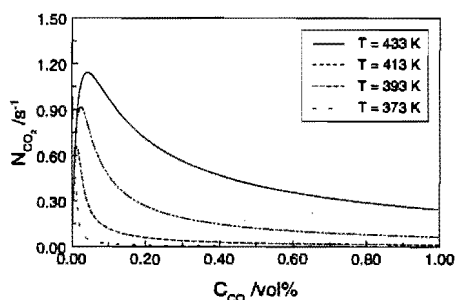


**Figure 4.8**  
Steady state turnover frequency as a function of the CO concentration calculated using Equation 4.3 at four temperatures. Parameters: Table 4.5.

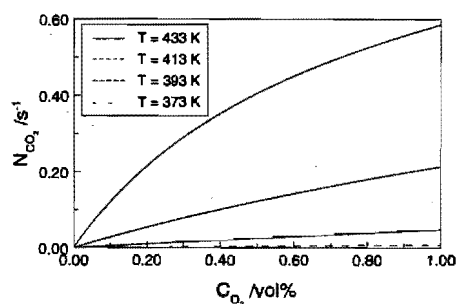


**Figure 4.9**  
Steady state turnover frequency as a function of the  $\text{O}_2$  concentration calculated using Equation 4.3 at four temperatures. Parameters: Table 4.5.

Most studies report a first order  $\text{O}_2$  dependency of the turnover frequency. The partial order of the oxygen concentration calculated with the model decreases from 1 to 0.6 with increasing temperature. The predicted activation energy of the global reaction amounts to 90 kJ/mol. This is in good agreement with the value of 100 kJ/mol often reported in the literature.

## 4.7 Conclusions

In order to study the CO oxidation cyclic feeding experiments in a fixed bed reactor have been performed. A regression analysis showed that cyclic feeding experiments provide much information about the reaction mechanism and the kinetic parameters. The reaction mechanism based on steady state experiments cannot be used to describe the transient responses. In order to describe these responses, the steady state kinetic model has to be adapted. The cyclic feeding experiments showed that the CO adsorption is not inhibited by the adsorbed oxygen, while the adsorbed CO

is inhibiting the  $O_2$  adsorption.

To model the experimental responses it is assumed that CO can chemisorb on a catalytic site already covered with oxygen. To account for the surface non-uniformity a linear dependency on the CO surface coverage of the activation energy of both the CO desorption and the surface reaction between adsorbed CO and oxygen adatoms has to be assumed. The  $CO_2$  adsorption on and the desorption from the support has also to be incorporated into the model.

The reaction mechanism based on the cyclic feeding experiments consists of adsorption, desorption and surface reaction steps. Nonlinear regression analysis showed that all 13 kinetic parameters of the reaction mechanism were estimated significantly. All parameter estimates are well in agreement with the values reported in the literature. The kinetic model also describes the steady state behaviour reported in the literature.

## References

- Bailey, J.E., Periodic phenomena. In Chemical reactor theory: A review (Edited by Lapidus, L. and Amundson N.R.) 758-813, Prentice-Hall, Englewood Cliffs, NJ, 1977
- Barshad, Y., Gulari, E., A dynamic study of CO oxidation on supported platinum, *AIChE J.* **31**, 649-658, 1985a
- Barshad, Y., Gulari, E., A novel catalytic reactor system for transient response and its use in CO oxidation on  $Pd/Al_2O_3$ , *J. Catal.* **94**, 1985b
- Barshad, Y., Zhou, X., Gulari, E., Carbon monoxide oxidation under transient conditions: A Fourier-Transform infrared transmission spectroscopy study, *J. Catal.* **94**, 128-141, 1985
- Berlowitz, P.J., Peden C.H.F., Goodman D.W., Kinetics of CO-oxidation on single-crystal Pd, Pt and Ir, *J. Chem. Phys.* **92**, 5213-5221, 1988
- Bonzel, H.P., Ku R., On the kinetics of oxygen adsorption on a Pt(111) surface, *Surf. Sci.* **40**, 85-101, 1973
- Boudart, M., Djéga-Mariadassou G., Kinetics of Heterogeneous Catalytic Reactions, Princeton University Press, Princeton, N.J., 1984
- Boudart, M., Rumpf F., The catalytic oxidation of CO and structure insensitivity, *React. Kinet. Catal. Lett.* **35**, 95-105, 1987
- Campman, M.A.J., Kinetics of carbon monoxide oxidation over supported platinum catalysts, The role of steam in the presence of ceria, Ph.D. Thesis, Eindhoven University of Technology, 1996
- Cho, B.K., West, L.A., Cyclic operation of  $Pt/Al_2O_3$  catalyst for CO oxidation, *Ind. Eng. Chem. Fund.* **25**, 158-164, 1986

- Compton, R.G., (ed.) Studies of kinetic modeling for oxidation reactions over metals (exemplified by CO oxidation), Comprehensive chemical kinetics, vol. 32: Kinetic models of kinetic reactions, Elsevier Science Publishing Company, Inc., New York, USA, 311-360, 1991
- Cutlip, M.B., Concentration forcing of catalytic surface rate processes, *AIChE J.* **25**, 502-508, 1979
- Cultip, M.B, Hawkins, C.J., Mukesh, P., Morton, W., Kenney, C.N., Modelling of forced periodic oscillations of carbon monoxide oxidation over platinum catalyst, *Chem. Eng. Comm.* **32**, 329-344, 1982
- Engel, T., Ertl G., Elementary steps in the catalytic oxidation of carbon monoxide on platinum metals, *Adv. Catal.* **28**, 1-78, 1979
- Freel, J., Chemisorption on supported platinum II, Stoichiometry for hydrogen, oxygen and carbon monoxide, *J. Catal.* **25**, 149-160, 1972
- Froment, G.F., Hosten L.H., Catalytic kinetics: Modeling, *Cat. Sc. Tech.* Anderson J.R., Boudart M., Springer Verlag, Berlin, 98-170, 1981
- Graham, W.R.C., Oxidation of carbon monoxide on platinum catalyst: kinetic model discrimination using experimental steady-state multiplicity and feed composition cycling, Ph.D. Thesis, University of Alberta, 1993
- Harold, M.P., Garske, M.E., Kinetics and multiple rate states of CO oxidation on Pt. I Model development and multiplicity analysis, *J. Catal.* **127**, 524-552, 1991a
- Harold, M.P., Garske, M.E., Kinetics and multiple rate states of CO oxidation on Pt. II Linking UHV and atmospheric pressure kinetic behavior, *J. Catal.* **127**, 553-575, 1991b
- Herz, R.K., Marin S.P., Surface chemistry models of carbon monoxide oxidation on supported platinum catalysts, *J. Catal.* **65**, 281-296, 1980
- Herz, R.K., Shinouskis, J., Transient oxidation and reduction of alumina supported platinum, *Appl.Surf.Sci.* **19**, 373-397, 1984
- Huinink, J.P.H., A quantitative analysis of transient kinetic experiments: the oxidation of CO by  $O_2/NO$  on Pt, Ph.D. Thesis, Eindhoven University of Technology, 1995
- Kitrell, J.R., Mathematical modelling of chemical reactions, *Adv. Chem. Eng.* **8**, 97, 1970
- Li, Y-E, Boecker, D., Gonzales, R.D., CO oxidation on  $Pt/SiO_2$  and  $Pd/Al_2O_3$  catalysts. Rapid FTIR transient studies, *J. Catal.* **110**, 319-329, 1988
- Luntz, A.C., Grimblot, J., Fowler, D.E., Sequential precursors in dissociative chemisorption:  $O_2$  on  $Pt(111)$ , *Phys. Rev. B.* **39**, 12903-12906, 1989
- Lynch, D.T., Use of elementary step mechanism to explain resonant behaviour for CO oxidation on platinum, *Can. J. Chem. Eng. Sci.* **62**, 691-698, 1984
- Matros, Y.S., Catalytic processes under unsteady-state conditions, Studies in surface science and catalysis, **43**, Elsevier, Amsterdam, 1989
- NAG Fortran Library Manual, mark 16, volume 1, 1995

- Odrpack, User's reference guide for odrpack version 2.01, Software for weighted orthogonal distance regression, 1992
- Oh, S.H., Fisher, G.B., Carpenter J.E., Goodman, D.W., Comparative kinetic studies of CO-O<sub>2</sub> and CO-NO reactions over single crystal and supported rhodium catalysts, *J. Catal.* **100**, 360-376, 1986
- Prairie, M.R., Cho, B.K., Oh, S.H., Shinouskis, E.J., Bailey, J.E., Steady-state and transient studies of carbon monoxide oxidation on alumina-supported rhodium via transmission infrared spectroscopy, *Ind.Eng. Chem. Res.* **127**, 1396-1407, 1988
- Racine, B.N., Herz, R.K., Modelling dynamic CO oxidation over Pt/Al<sub>2</sub>O<sub>3</sub>: Effects of intrapellet diffusion and site heterogeneity, *J. Catal.*, **137**, 158-178, 1992
- Razon, L.F., Schmitz R.A., Intrinsically unstable behaviour during the oxidation of carbon monoxide on platinum, *Catal. Rev. Sci. Eng.* **28**, 89-164, 1986
- Sadhankar, R.R., Lynch, D.T., N<sub>2</sub>O reduction by CO over an alumina supported Pt-catalyst: forced composition cycling, *J. Catal.* **149**, 278-291, 1994
- Sant, R., Wolf, E.E., Elementary step modeling and transient FTIR studies of CO oxidation on Rh/SiO<sub>2</sub>, *Chem. Eng. Sci.* **45**, 3137-3147, 1990
- van Santen, R.A., Niemantsverdriet, J.W., Chemical kinetics and Catalysis, Eindhoven University of Technology, 1992
- Schiesser, W.E., The numerical methods of lines, Academic Press, San Diego, 1993
- Silveston P., Hudgins, R.R., Renken, A., Periodic operation of catalytic reactors - introduction and overview, *Catal. Today*, 91-112, 1996
- Tumer, J.E., Maple, M.B., Oxide formation and reduction over Pt, Pd, and Ir: A driving mechanism for oscillations in the CO oxidation reaction, *Surf. Sci.* **147**, 1984
- Zhdanov, V.P., Pavlíček, J., Knor, Z., Preexponential factors for elementary surface processes, *Catal. Rev. Sci. Eng.* **30**, 501-517, 1988.
- Zhdanov, V.P., Kasemo, B., Steady-state kinetics of CO oxidation on Pt: extrapolation from 10<sup>-10</sup> to 1 bar, *Appl. Surf. Sci.* **74**, 147-164, 1994
- Zhou, X., Barshad, Y., Gulari, E., CO oxidation on Pd/Al<sub>2</sub>O<sub>3</sub>. Transient response and rate enhancement through forced concentration cycling, *Chem. Eng. Sci.* **41**, 1277-1284, 1984
- Zhou, X., Gulari, E., CO oxidation on Pt/Al<sub>2</sub>O<sub>3</sub> and Pd/Al<sub>2</sub>O<sub>3</sub> transient response and concentration cycling studies, *Chem. Eng. Sci.* **41**, 883-890, 1986



# 5

---

## TRANSIENT KINETICS OF THE CO OXIDATION OVER Pt/Rh/CeO<sub>2</sub>/γ-Al<sub>2</sub>O<sub>3</sub>

### 5.1 Introduction

Commercial automotive three-way exhaust catalysts commonly contain relatively large amounts of cerium oxide. Several effects have been ascribed to the cerium oxide addition. Ceria has been found to stabilize the noble metal dispersion at high temperatures (Summers and Ausen, 1979; Su *et al.* 1985) and to improve the thermal stability of the catalyst (Harrison *et al.*, 1988). Furthermore it was found to promote the water-gas shift reaction at temperatures above the light-off (Kim, 1982; Herz and Sell, 1985; Harrison *et al.*, 1988), hence improving the catalyst's CO conversion activity. However, the experimentally found higher activity of a ceria promoted catalyst cannot totally be explained by the water-gas shift reaction. Several studies show that ceria improves the CO oxidation activity even at relatively low temperatures (Serre *et al.*, 1993b; Nunan *et al.*, 1992; Campman, 1996), when there is no contribution of the water-gas shift reaction to the rate of CO oxidation.

The higher activity is often explained by assuming a second mechanism for the CO oxidation with oxygen apart from the Langmuir-Hinshelwood reaction: the reaction between CO adsorbed on the noble metal and oxygen from ceria. Zafiris and Gorte (1993) assumed that oxygen adsorbs on ceria and reacts with CO on the noble metal after reverse spill-over of oxygen. However, most often the observed behaviour is explained by the reaction between oxygen adsorbed on ceria and CO on the noble metal (Jin *et al.*, 1987; Oh and Eickel, 1988; Serre *et al.*, 1993a; Campman, 1996).

Under transient conditions cerium oxide acts as an oxygen storage component (Kim, 1982; Herz, 1981; Herz *et al.*, 1983; Yao and Y Yao, 1984; Su *et al.*, 1985), which is a very important feature under conditions encountered in practical use. Because of the feed-back controller applied in cars to keep the air to fuel ratio near to its stoichiometric point, the exhaust gas has a cyclic net oxidizing to net reducing composition oscillation. Cerium oxide can provide oxygen for the CO and hydrocarbon oxidation during the net reducing excursions of the oscillation period, while oxygen is stored from the gas phase at net oxidizing conditions. Hence, during dynamic operation the time-average activity is improved by sustaining the appropriate oxygen stoichiometry (Herz *et al.*, 1983; Yao and Y Yao, 1984). Su *et al.* (1985) and Yao and Y Yao (1984) showed that only a fraction of the total amount of oxygen in the bulk of ceria is available for reaction under transient conditions.

Since automotive exhaust gas contains about 10% steam its influence on the CO oxidation activity is an interesting issue. Although beneficial effects are generally assigned to the water gas shift reaction even at low temperatures it was found that temperatures over 670 K were required for this reaction to occur at a substantial rate (Schlatter and Mitchell, 1980; Kim, 1982).

The purpose of the present chapter is to study the CO oxidation with oxygen over Pt/Rh/CeO<sub>2</sub>/γ-Al<sub>2</sub>O<sub>3</sub> under typical exhaust gas conditions using cyclic feeding experiments. From these experiments especially the role of ceria will become clear. Experiments with a feed stream which also contains steam and CO<sub>2</sub> are performed to study the effects of these components on the CO oxidation under realistic exhaust gas conditions.

## 5.2 Experimental results and discussion

### 5.2.1 Experimental conditions

After the catalyst pretreatment as described in section 2.4.1 and prior to the experiments with cycling of the feed streams, steady state experiments were carried out to check the catalyst's activity. When the activity of the catalyst was stable after approximately one hour it was compared with that of a fresh catalyst. The reactor was loaded with a new catalyst when the activity has decreased more than 10%.

In Table 5.1 the conditions during the transient experiments are shown. They are similar to the conditions during experiments with the Pt/γ-Al<sub>2</sub>O<sub>3</sub> catalyst, discussed in Chapter 4. Therefore, the results of experiments presented in this chapter can be compared with the results of the Pt/γ-Al<sub>2</sub>O<sub>3</sub> catalyst discussed in Chapter 4, to clarify the role of ceria even more.

**Table 5.1**  
**Experimental conditions during the cyclic**  
**feeding experiments over  $\text{Pt/Rh/CeO}_2/\gamma\text{-Al}_2\text{O}_3$ .**

$p_{\text{tot}}$	/kPa	110
$p_{\text{CO}}^{1) 2)}$	/kPa	0.55
$p_{\text{O}_2}^{1) 2)}$	/kPa	0.55
T	/K	373 - 473
W	/kg <sub>c</sub>	$1.01 \cdot 10^{-3}$
f	/Hz	0.1 - 2
$F_{\text{tot}}^{3)}$	/mol s <sup>-1</sup>	$5.6 \cdot 10^{-3}$
<sup>1)</sup> CO and O <sub>2</sub> oscillate in counter phase; CO is fed one half of a period, O <sub>2</sub> the other half.		
<sup>2)</sup> during the experiments with CO <sub>2</sub> and steam the feed also contains 11 kPa CO <sub>2</sub> and 11 kPa H <sub>2</sub> O		
<sup>3)</sup> $F_{\text{tot}}$ includes balance gas He		

### 5.2.2 Cyclic feeding experiments with CO and O<sub>2</sub>

In Figure 5.1 the outlet concentrations are shown when the inlet concentrations are cycled at a frequency of 0.1 Hz. One half of the period CO only is fed to the reactor, while the other half the feed contains oxygen. The responses are a part of a stable oscillation which allows the calculation of the oxygen and CO adsorption capacities by integrating the CO<sub>2</sub> response in time. During the time oxygen only is fed to the reactor the amount of CO<sub>2</sub> produced is determined by the CO adsorption capacity and amounts to  $1.7 \cdot 10^{-2}$  mol/kg<sub>c</sub>. This value is in good agreement with the noble metal capacity determined by stationary CO chemisorption experiments, see Table 2.1 section 2.3. The amount of CO<sub>2</sub> produced during the CO containing feed stream is larger than the noble metal capacity and amounts to  $2.1 \cdot 10^{-2}$  mol/kg<sub>c</sub>.

After switching from the CO to the O<sub>2</sub> containing feed stream, the oxygen concentration initially increases very fast. The outlet oxygen concentration follows

then the inlet concentration (not shown). After 0.1 s the oxygen concentration passes the local maximum whereas the local minimum is reached after 0.2 s. The oxygen concentration relaxes to the steady state on a time-scale of about 1 s. As soon as the oxygen concentration passes the local maximum, the  $\text{CO}_2$  outlet concentration starts to increase and it takes about 0.4 s to reach the local maximum. After that the concentration relaxes to the final value without reaching a steady state.

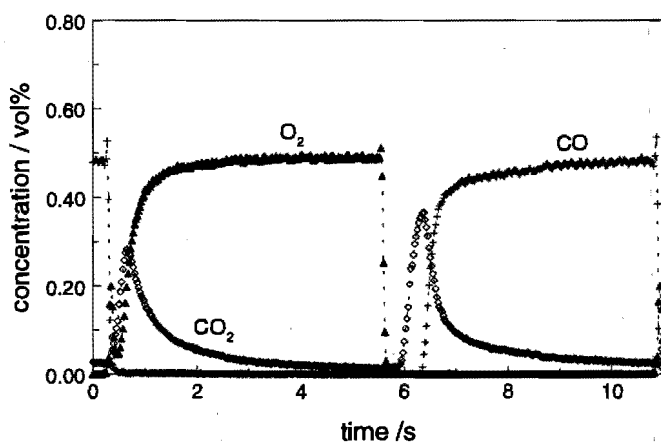


**Figure 5.1**

**$\text{CO}$ ,  $\text{O}_2$  and  $\text{CO}_2$  outlet concentrations versus time during forced cycling of the  $\text{CO}$  and  $\text{O}_2$  concentration. + =  $\text{CO}$ ;  $\blacktriangle$  =  $\text{O}_2$ ;  $\diamond$  =  $\text{CO}_2$ . Conditions:  $T = 393\text{ K}$ ,  $f = 0.1\text{ Hz}$  and Table 5.1.**

The observed behaviour can be explained as follows. At  $t = 0$  the noble metal surface is in quasi-steady state with the gas phase and will be almost completely covered with  $\text{CO}$ . Immediately after switching the feed streams, oxygen cannot adsorb on the noble metal surface due to the high degree of  $\text{CO}$  coverage. Since ceria is reduced by the  $\text{CO}$  containing feed stream its surface possesses a relatively large amount of oxygen vacancies (Jin *et al.*, 1987; Oh and Eickel, 1988; Serre *et al.*, 1993a) and therefore oxygen in the gas phase initially adsorbs on ceria after switching the feed streams. As no oxygen is present at the noble metal, the increasing  $\text{CO}_2$  concentration can only be explained by the existence of another route for the  $\text{CO}_2$  formation apart from the Langmuir-Hinshelwood reaction. Most probably oxygen at the noble metal-ceria interface reacts with  $\text{CO}$  adsorbed on the noble metal via the so-called bifunctional reaction path. The reaction path is considered bifunctional because ceria provides oxygen adsorption sites, while  $\text{CO}$

only adsorbs significantly on the noble metal surface. As a result of the CO<sub>2</sub> formation via the bifunctional reaction path the O<sub>2</sub> outlet concentration starts to decrease and vacant sites are created at the noble metal surface. Oxygen from the gas phase now also adsorbs on the noble metal and the Langmuir-Hinshelwood reaction takes place. The CO<sub>2</sub> formation proceeds then via two parallel pathways: the Langmuir Hinshelwood reaction and the reaction between oxygen on ceria and CO on the noble metal. This leads to a faster decreasing O<sub>2</sub> gas phase concentration. When the rate of CO<sub>2</sub> production becomes smaller due to depletion of CO adsorbed on the noble metal, the oxygen concentration starts to increase and the noble metal becomes more covered with oxygen. When all adsorbed CO has reacted the noble metal surface will be totally covered with oxygen adatoms and the CO<sub>2</sub> production stops. The ceria surface and the bulk of ceria will become more oxidized by oxygen in the feed stream and the O<sub>2</sub> concentration relaxes to the steady state value. The relatively large time-scale of the CO<sub>2</sub> relaxation after O<sub>2</sub> has reached the steady state is caused by desorption from ceria (Li *et al.*, 1989a), and from γ-Al<sub>2</sub>O<sub>3</sub> (Lynch and Graham, 1990).

When switching from the feed stream containing O<sub>2</sub> to the one containing CO it takes about 0.8 s before CO is detected at the outlet. After an induction time of 0.4 s the CO<sub>2</sub> concentration starts to increase. The global maximum of the CO<sub>2</sub> response coincides with the breakthrough of the CO concentration. Both CO and CO<sub>2</sub> relax to their final values without reaching the steady state.

Just before switching the feed stream to CO, the noble metal surface is completely covered with oxygen. The number of vacant sites will be smaller compared the beginning of the period  $t = 0$  s, since oxygen desorption is negligible under the experimental conditions (Engel and Ertl, 1979). However, as it follows from Figure 5.1, all CO fed to the reactor adsorbs on the catalyst after switching the feed streams. Probably, some CO will adsorb on the oxidized ceria surface thereby creating carbonate like species (Jin *et al.*, 1987; Li *et al.*, 1989a), but this cannot explain the large induction time of the CO concentration shown in Figure 5.1. As discussed in Chapter 4, CO adsorption on Pt/γ-Al<sub>2</sub>O<sub>3</sub> is not inhibited by oxygen adsorbed on the noble metal. There exist sufficient evidence that CO adsorption on ceria promoted catalysts is similar to unpromoted catalysts (Oh and Eickel, 1988; Zafiridis and Gorte, 1993). Therefore, it is reasonable to assume that most of CO adsorbs on the noble metal surface covered with oxygen adatoms and reacts with both noble metal oxygen and oxygen from ceria via the bifunctional path.

When most of noble metal oxygen has reacted the CO<sub>2</sub> formation rate decreases and the surface becomes covered with CO. The gas phase concentration starts to increase but does not reach the inlet concentration of 0.5 vol% because of the reaction between CO adsorbed on the noble metal and oxygen from ceria. The latter causes an ongoing CO<sub>2</sub> formation even when there is no oxygen left on the

noble metal. The significantly higher  $\text{CO}_2$  concentration in the slow transient part of the response compared to that during the  $\text{O}_2$  containing feed stream is also an indication of the ongoing reaction. Oxygen depletion of the ceria interface can be filled up by both surface diffusion and diffusion from the bulk of ceria. The ceria surface will be reduced to some extent before bulk diffusion becomes important since surface diffusion takes place at a time-scale which is several orders of magnitude smaller than that of bulk diffusion (Martin and Duprez, 1996). Assuming  $\text{CeO}_2$  particles with a diameter of  $6 \cdot 10^{-9}$  m (Oh and Eickel, 1988) and a diffusion coefficient of  $10^{-18}$   $\text{m}^2/\text{s}$  (Martin and Duprez, 1996), the time-scale of surface diffusion will be of the same order as the period. The assumption that surface diffusion is the rate determining step of the bifunctional path (Martin and Duprez, 1993) leads to the conclusion that the ceria surface is almost completely oxidized and reduced within one period at a cycling frequency of 0.1 Hz. The time-scale of bulk diffusion is large compared to the period and therefore this process will be in the sliding regime, meaning that the oxygen flux due to diffusion oscillates with a relatively small amplitude. Hence, mainly the reaction between noble metal CO and oxygen on the surface of ceria leads to the ongoing  $\text{CO}_2$  formation shown in Figure 5.1.

The induction time of the  $\text{CO}_2$  concentration is probably caused by adsorption of gaseous  $\text{CO}_2$  on ceria as reported by Li *et al.*, (1989a). They showed that for  $\text{CO}_2$  adsorption to take place significantly the ceria surface has to be oxidized. Therefore, it is reasonable to assume that after switching the feed stream to CO initially all  $\text{CO}_2$  adsorbs on the oxidized ceria surface. Since the ceria surface is reduced at  $t = 0$  s, no significant  $\text{CO}_2$  adsorption occurs after switching the feed stream to oxygen.

The difference between the amount of  $\text{CO}_2$  produced during the CO and the  $\text{O}_2$  feeding part of the period is now also clear. The amount of  $\text{CO}_2$  produced during feeding oxygen is determined by the capacity of the noble metal only. However,  $\text{CO}_2$  formation proceeds via two parallel pathways when the feed stream contains CO only: the Langmuir-Hinshelwood reaction and the reaction between CO adsorbed on the noble metal and oxygen on the ceria surface. Hence, the amount of  $\text{CO}_2$  is not only determined by the noble metal capacity but also by the amount of oxygen from ceria which is available for reaction.

Summarizing, the transient behaviour of the CO oxidation with oxygen over  $\text{Pt/Rh/CeO}_2/\gamma\text{-Al}_2\text{O}_3$  can be explained assuming the following steps: adsorption of CO and  $\text{O}_2$  on the noble metal surface leading to the  $\text{CO}_2$  formation via the Langmuir-Hinshelwood reaction. Oxygen in the gas phase can also adsorb on the ceria surface and diffuse into the bulk of ceria or to the noble metal-ceria interface where the reaction with CO adsorbed on the noble metal takes place. Bulk oxygen diffuses to the ceria surface where it can also participate in the CO oxidation. At relatively low temperatures bulk oxygen plays almost no role in the  $\text{CO}_2$  formation.

### Effect of temperature

In Figure 5.2 the responses of CO,  $\text{O}_2$  and  $\text{CO}_2$  are shown at a temperature of 373 K. Compared to a temperature of 393 K, see Figure 5.1, the local maximum of the  $\text{O}_2$  concentration is higher after switching to the oxygen containing feed stream. This can be explained by assuming that a smaller amount of oxygen adsorbs on the ceria surface. The ceria surface will be less reduced at a lower temperature, as a result of the lower rate of  $\text{CO}_2$  formation via the bifunctional path. Therefore, less vacant adsorption sites are available for oxygen to adsorb on.

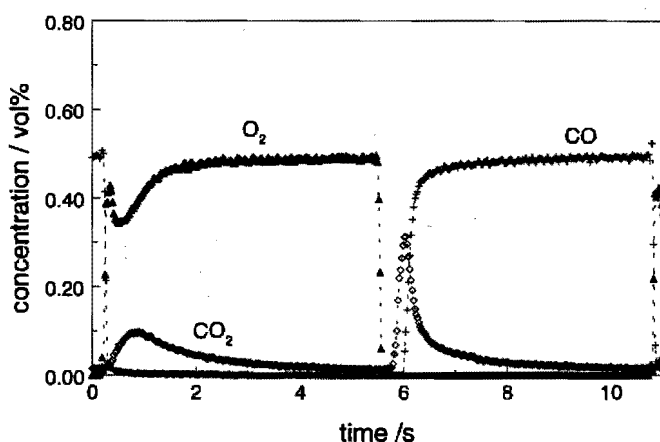


**Figure 5.2**

**CO,  $\text{O}_2$  and  $\text{CO}_2$  outlet concentrations versus time during forced cycling of the CO and  $\text{O}_2$  concentration. + = CO; ▲ =  $\text{O}_2$ ; ◇ =  $\text{CO}_2$ . Conditions:  $T = 373\text{ K}$ ,  $f = 0.1\text{ Hz}$  and Table 5.1.**

As a result of the lower rate of the reaction between adsorbed CO and oxygen at the ceria and of the Langmuir-Hinshelwood reaction  $\text{CO}_2$  formation proceeds on a larger time-scale, as shown in Figure 5.2. The amount of  $\text{CO}_2$  produced during feeding oxygen is smaller compared to Figure 5.1. This is an indication that not all adsorbed CO reacts with oxygen within half a period and consequently less oxygen can adsorb on the noble metal surface. When comparing Figures 5.1 and 5.2 it is also clear that  $\text{CO}_2$  desorption from both ceria and  $\gamma\text{-Al}_2\text{O}_3$  is rather independent of the temperature.

The shape of the responses after switching the feed stream from  $\text{O}_2$  to CO is rather independent of the temperature. Compared to Figure 5.1, the induction time of the CO response is smaller which can be explained by assuming that CO

adsorption is inhibited by CO already present on the noble metal surface as a result of the relatively large time-scale of  $\text{CO}_2$  formation. In contrast to Figure 5.1, the CO concentration in Figure 5.2 equals the inlet concentration at the end of the period. The ongoing reaction in the second half of the period at a temperature of 393 K was explained by oxygen supply mainly as a result of surface diffusion. The time-scale of surface diffusion will be comparable to the time-scale at a temperature of 393 K, as the temperature dependence of surface diffusion is rather small (Martin and Duprez, 1996). Clearly the reaction at the noble metal-ceria interface is the rate determining step of the bifunctional path at a temperature of 373 K, which is in agreement with the behaviour after switching the feed stream from CO to  $\text{O}_2$ .

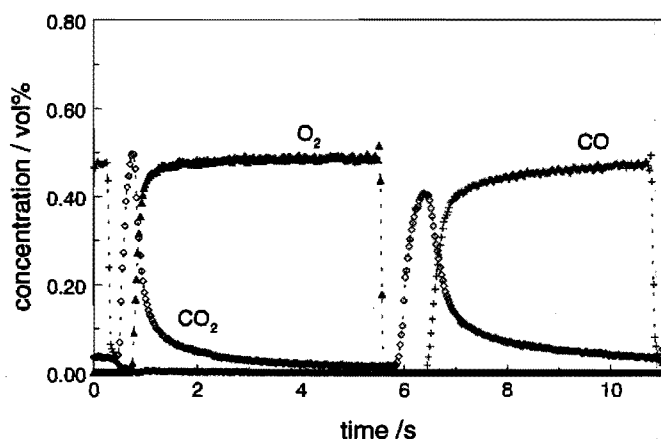


**Figure 5.3**

**CO,  $\text{O}_2$  and  $\text{CO}_2$  outlet concentrations versus time during forced cycling of the CO and  $\text{O}_2$  concentration. + = CO; ▲ =  $\text{O}_2$ ; ◇ =  $\text{CO}_2$ . Conditions:  $T = 453 \text{ K}$ ,  $f = 0.1 \text{ Hz}$  and Table 5.1.**

Experiments conducted at a higher temperature show that oxygen diffusion in the bulk of ceria is strongly dependent of the temperature. In Figure 5.3 the outlet concentrations at a temperature of 453 K are shown. After switching from CO to  $\text{O}_2$ , the  $\text{O}_2$  signal at the outlet initially remains zero. All oxygen adsorbs on the ceria surface and reacts with CO via the bifunctional path. The processes occur on a smaller time-scale at this temperature compared to a temperature of 373 K as can be seen from the steeper slope of the responses. As also shown in Figure 5.3, a significant extent of diffusion of oxygen from the bulk takes place at elevated temperatures since a large amount of  $\text{CO}_2$  is produced when the feeds stream



contains CO only.

### Effect of frequency

As shown in Figure 5.4, the reactor is operated in the dynamic regime at a frequency of 0.5 Hz and a temperature of 453 K. The shape of the responses is similar to part of the responses immediately after switching the feed stream, shown in Figure 5.3. In contrast to a cycling frequency of 0.1 Hz, reaction always takes place at a frequency of 0.5 Hz. Clearly, there is always CO present at the noble metal surface which reacts with both oxygen on the noble metal surface via the

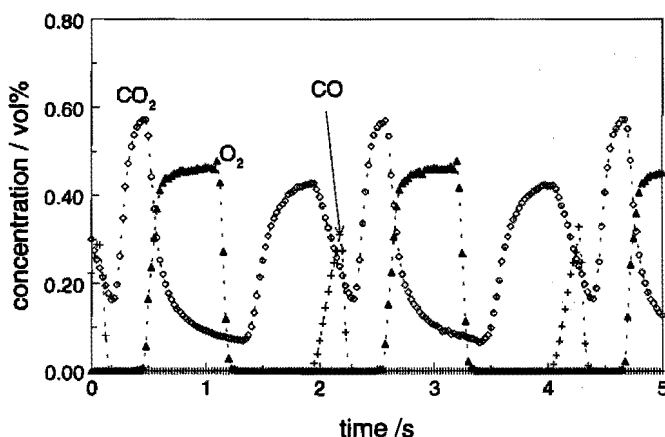


**Figure 5.4**

**CO, O<sub>2</sub> and CO<sub>2</sub> outlet concentrations versus time during forced cycling of the CO and O<sub>2</sub> concentration. + = CO; ▲ = O<sub>2</sub>; ◇ = CO<sub>2</sub>. Conditions:  $T = 453\text{ K}$ ,  $f = 0.5\text{ Hz}$  and Table 5.1.**

Langmuir-Hinshelwood reaction and with oxygen at the ceria surface via the bifunctional path. Probably the noble metal surface is also covered with some oxygen because it is unlikely that a large part of the surface remains unoccupied when the feed stream contains O<sub>2</sub> only. The induction time of the CO concentration is comparable to the induction time in Figure 5.3, the induction time of the CO<sub>2</sub> concentration is smaller. The latter is caused by the rather constant and relatively high degree of CO<sub>2</sub> coverage on the ceria which inhibits the adsorption of CO<sub>2</sub> from the gas phase.

### Comparison with the Pt/ $\gamma$ -Al<sub>2</sub>O<sub>3</sub> catalyst

In Chapter 4 cyclic feeding experiments with a Pt/ $\gamma$ -Al<sub>2</sub>O<sub>3</sub> catalyst are discussed. The role of ceria becomes even more clear when comparing the dynamic behaviour of both catalysts. It should however be noted that from the CO chemisorption experiments, see section 2.3, it is clear that the specific noble metal adsorption capacity of the Pt/Rh/CeO<sub>2</sub>/ $\gamma$ -Al<sub>2</sub>O<sub>3</sub> is larger than that of the Pt/ $\gamma$ -Al<sub>2</sub>O<sub>3</sub> catalyst. Therefore, the amount of CO<sub>2</sub> produced during feeding oxygen will not be the same for both catalyst although the reactor contained approximately the same amount of catalysts. However, the role of ceria can be determined in a direct way by comparison of the results of the two catalyst since the shape of the individual responses contains most of the kinetic information. The amounts of CO<sub>2</sub> produced give information about the oxygen and CO adsorption capacity only.

As mentioned before, oxygen from the gas phase not only adsorbs on the noble metal surface but also on the reduced ceria surface of the Pt/Rh/CeO<sub>2</sub>/ $\gamma$ -Al<sub>2</sub>O<sub>3</sub> catalyst, and CO<sub>2</sub> formation proceeds via two pathways: CO adsorbed on the noble metal surface can react with noble metal oxygen and with oxygen from ceria. In case of the Pt/ $\gamma$ -Al<sub>2</sub>O<sub>3</sub> catalyst oxygen adsorbs on the noble metal surface only and CO<sub>2</sub> formation takes place via the Langmuir-Hinshelwood reaction.

The local maximum of the O<sub>2</sub> concentration immediately after switching the feed stream from CO to oxygen, see Figure 5.2, is lower compared to the Pt/ $\gamma$ -Al<sub>2</sub>O<sub>3</sub> catalyst, Figure 4.2, since oxygen adsorption on the ceria promoted catalyst proceeds on a smaller time-scale as a result of the vacant sites on ceria. In case of the Pt/ $\gamma$ -Al<sub>2</sub>O<sub>3</sub> catalyst, CO inhibition leads to a large time-scale of oxygen adsorption which explains also the induction time after switching the feed stream to O<sub>2</sub>. Furthermore, the parallel reaction pathways for the CO oxidation over the ceria containing catalyst lead to a relatively small time-scale of CO<sub>2</sub> formation after switching the feed streams. The oxygen concentration relaxes faster to the steady state value and the CO<sub>2</sub> concentrations increases faster.

The CO response as a result of switching the feed stream from oxygen to CO is similar for both catalysts. As CO adsorption is not inhibited by oxygen initially all CO adsorbs on the noble metal surface. Both the faster CO<sub>2</sub> relaxation behaviour and the higher maximum in Figure 5.2 are a result of the two parallel reaction paths. The induction time of the CO<sub>2</sub> concentration in case of the Pt/Rh/CeO<sub>2</sub>/ $\gamma$ -Al<sub>2</sub>O<sub>3</sub> catalyst is caused by adsorption of CO<sub>2</sub> on the oxidized ceria surface.

### **5.2.3 Effect of CO<sub>2</sub> and H<sub>2</sub>O**

Automotive exhaust gas contains about 10% CO<sub>2</sub> and 10% steam. The

presence of CO<sub>2</sub> lowers the steady state CO<sub>2</sub> production rate whereas water is found to have a beneficial effect on the CO oxidation activity (Campman, 1996). To study the influence of H<sub>2</sub>O and CO<sub>2</sub> on the CO oxidation under dynamic conditions forced concentration cycling experiments were performed. The results of a typical experiment with both feed streams containing 10% CO<sub>2</sub> and H<sub>2</sub>O, *i.e.* cyclic feeding of the CO and O<sub>2</sub> concentration only, is shown in Figure 5.5. It should be noticed that the noise on the CO<sub>2</sub> signal is a result of the relatively small changes in the concentration due to the cyclic feed compared to the feed concentration. Notice also that the right axis in Figure 5.5 begins at 9.9 vol%.

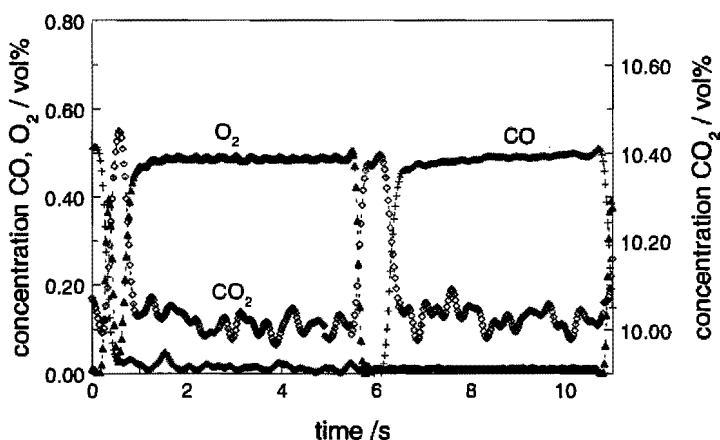


**Figure 5.5**

**CO, O<sub>2</sub> and CO<sub>2</sub> outlet concentrations versus time during forced cycling of the CO and O<sub>2</sub> concentration and 10% CO<sub>2</sub> and 10% H<sub>2</sub>O in the feed stream. Conditions:  $T = 393$  K,  $f = 0.1$  Hz and Table 5.1.**

After switching from CO to O<sub>2</sub>, the O<sub>2</sub> signal increases very fast and follows the inlet concentration. Compared to the results with a feed containing CO and O<sub>2</sub> only, see Figure 5.1, the local maximum of the oxygen concentration is much higher. The relaxation of the O<sub>2</sub> and CO<sub>2</sub> the concentration to the steady state proceeds on a smaller time-scale compared to the experiments without CO<sub>2</sub> and H<sub>2</sub>O.

The observed behaviour can be explained as follows. Oxygen adsorption on ceria is initially blocked by the large amount of CO<sub>2</sub> present at the ceria surface (Herz 1981; Jin *et al.*, 1987; Li *et al.*, 1989a), due to the high CO<sub>2</sub> concentration in feed. Probably the presence of hydroxyl groups on ceria as a result of adsorption of water blocks also adsorption sites for oxygen (Sass *et al.*, 1985; Padeste *et al.*,

1993). As a smaller amount of oxygen adsorbs on the ceria surface, the  $\text{CO}_2$  formation via the bifunctional path becomes less important and the CO oxidation activity decreases. The role of ceria becomes less pronounced and the behaviour of the  $\text{Pt}/\gamma\text{-Al}_2\text{O}_3$  catalyst is approximated. The small time-scale of the  $\text{CO}_2$  relaxation is due to the absence of significant  $\text{CO}_2$  adsorption as a result of inhibition by the large amount of  $\text{CO}_2$  present on both ceria and the alumina support.

After switching from the  $\text{O}_2$  to the CO containing feed stream there is no induction time in  $\text{CO}_2$  concentration. As mentioned before,  $\text{CO}_2$  produced by reaction no longer adsorbs on ceria and is therefore immediately detected at the outlet of the reactor.

Water is said to have a beneficial effect on the CO oxidation activity (Campman, 1996). The relaxation of the CO concentration to the steady state proceeds on a smaller time-scale compared to the experiments without  $\text{CO}_2$  and steam in the feed stream. Since  $\text{CO}_2$  and water do not adsorb significantly on the noble metal surface (Engel and Ertl, 1979; Heras and Viscido, 1988, respectively), it is clear that the CO oxidation rate is higher when  $\text{H}_2\text{O}$  is present in the feed stream. Campman (1996) assumed that the reaction between hydroxyl groups as a result of  $\text{H}_2\text{O}$  adsorption on ceria and molecular adsorbed oxygen on the ceria surface (Sass *et al.*, 1986) leads to the formation atomic oxygen species. The latter are more reactive than molecularly adsorbed oxygen and react readily with CO on the noble metal which explains the rate enhancement by steam.

It is not possible to calculate the amounts of  $\text{CO}_2$  produced during the oxygen and CO part of the period due to the noisy signal of  $\text{CO}_2$ , and therefore the oxygen and CO capacities cannot be determined. However, compared to the experiments without  $\text{CO}_2$  and steam the CO capacity has not changed since  $\text{CO}_2$  and water do not adsorb on the noble metal (Engel and Ertl, 1979; Heras and Viscido, 1988, respectively). The oxygen capacity will be smaller as result of the adsorption of  $\text{CO}_2$  and  $\text{H}_2\text{O}$  on ceria.

#### 5.2.4 Effects of cerium oxide on the time-average conversion

Under dynamic reactor operation ceria is believed to increase the time-average conversions. During the net reducing cycle of the oscillation oxygen from bulk ceria participates in the reaction resulting in a higher  $\text{CO}_2$  production rate. During the net oxidizing part of the oscillation the bulk is replenished with oxygen. Therefore, the oxygen capacity of ceria leads to a more appropriate oxygen stoichiometry during the oscillation resulting in a higher time-average conversion. In Figure 5.6 the time-average CO conversions at four temperatures are shown as a function of the frequency.

The behaviour at a temperature of 373 K in the quasi-steady state regime, *i.e.* at sufficiently low frequencies, can be explained considering the amounts of CO<sub>2</sub> produced per second during the oxygen and during the CO feeding part of the period. Just before switching the feed stream to oxygen, the noble metal surface will be totally covered with CO. After switching over, the amount of CO<sub>2</sub> produced by the reaction between adsorbed CO and oxygen from the feed is independent of the frequency and determined by the capacity of the noble metal only. Hence, the time-average CO<sub>2</sub> production during the oxygen feeding part of the period increases proportionally with the frequency. During the CO feeding half of the period the amount of CO<sub>2</sub> produced is not only determined by the noble metal capacity but also by the amount of oxygen adsorbed on the ceria surface. The CO<sub>2</sub> production per second is therefore higher and increases linearly as a function of the frequency. Hence, in the quasi-steady regime at 373 K the time-average CO<sub>2</sub> production within one complete period increases linearly as a function of the frequency.

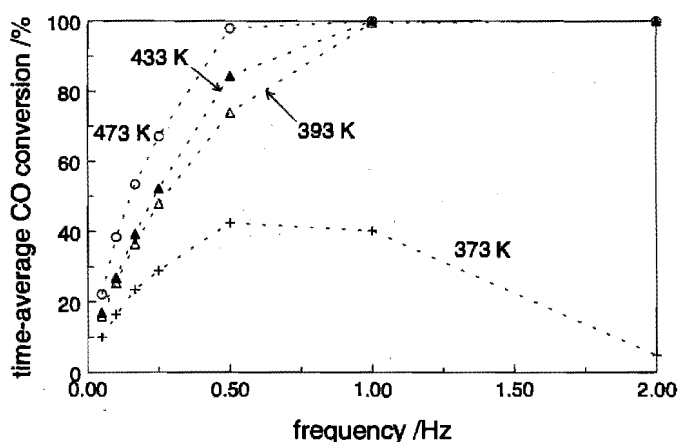


**Figure 5.6**

**Time-average conversions as a function of the frequency at four temperatures: + = 373 K; Δ = 393 K; ▲ = 433 K; o = 473 K.**

Conditions: Table 5.1.

When the reactor enters the dynamic regime the time-average conversion increases initially less than proportional as a function of the frequency. In contrast to the quasi-steady state regime the noble metal surface is not completely covered with either CO or oxygen at the end of the relevant reactant feeding part of the period. The time-scales of the surface processes are of the same order as the period, and therefore the surface coverages do not reach the steady state within a half a period.

The amount of  $\text{CO}_2$  produced during one complete period is now determined by ratio of the time-scale of  $\text{CO}_2$  formation to the period. Since CO adsorption proceeds on a smaller time-scale than oxygen adsorption, the surface becomes more and more CO covered with increasing frequency. The resulting lower surface coverage of oxygen leads to a less than proportional increase of time-scale of  $\text{CO}_2$  formation due to the non-linear behaviour of the reaction. Consequently, the time-average conversion increases also less than proportional as a function of the frequency. Since the degree of the CO coverage increases as a function of the frequency, oxygen adsorption is more inhibited and  $\text{CO}_2$  formation via the bifunctional path becomes more important.

In the sliding regime, at relatively high frequencies, the time-average conversion decreases with increasing frequency. The noble metal surface becomes even more covered with strongly adsorbed CO and the steady state surface coverage corresponding to the time-average feed composition is approached. During the whole oxygen feeding part period CO adsorbed on the noble metal inhibits the adsorption of oxygen and less  $\text{CO}_2$  is produced by the Langmuir-Hinshelwood reaction. At a very high frequency,  $\text{CO}_2$  formation proceeds via the bifunctional path only.

At a higher temperature the time-average conversion increases faster but less than proportional as a function of the frequency. In the quasi-steady state regime the amount of  $\text{CO}_2$  produced during the half of the period the feed stream contains oxygen, is still determined by amount of adsorbed CO. The latter decreases with increasing temperature due to the lower steady state value of the surface coverage as a result of the activated CO desorption. However, significantly more  $\text{CO}_2$  is produced during feeding CO as the amount of oxygen from ceria which participates in the reaction increases. But, since the time-scale of bulk diffusion is large compared to the period, the amount of  $\text{CO}_2$  produced within half a period decrease as a function of the frequency. Therefore, the time-average conversion increases less than proportional to the frequency at a higher temperature.

In the sliding regime the time-average conversion becomes 100%. At an elevated temperature the time-scale of the surface processes is much smaller than the period. The noble metal is always covered with both CO and oxygen and  $\text{CO}_2$  formation always takes place leading to 100% conversion.

Compared to the  $\text{Pt}/\gamma\text{-Al}_2\text{O}_3$  catalyst in case of the  $\text{Pt}/\text{Rh}/\text{CeO}_2/\gamma\text{-Al}_2\text{O}_3$  catalyst the time-average conversion increases faster as a function of the temperature due to the extra oxygen capacity of the ceria addition. The ongoing reaction when the feed stream contains CO only results in a higher time-average conversion.

### 5.3 Reaction mechanism

A reaction mechanism for the CO oxidation by oxygen over the Pt/Rh/CeO<sub>2</sub>/γ-Al<sub>2</sub>O<sub>3</sub> catalyst based on the cyclic feeding experiments without CO<sub>2</sub> and steam is presented in Table 5.2. There exists sufficient evidence that the adsorption characteristics of CO and oxygen on alumina supported noble metal catalysts are not significantly modified by ceria (Oh and Eickel, 1988; Zafiridis and Gorte, 1993). Therefore, it can be assumed that the monofunctional reaction path is similar to the

**Table 5.2**

**Reaction mechanism for the CO oxidation with oxygen in the absence of steam on a Pt/Rh/CeO<sub>2</sub>/γ-Al<sub>2</sub>O<sub>3</sub> catalyst.**

elementary reaction	
1	$CO + * \rightleftharpoons CO^*$
2	$O_2 + * \rightarrow O_2^*$
3	$O_2^* + * \rightarrow 2 O^*$
4	$CO^* + O^* \rightarrow CO_2 + 2 *$
5	$CO + O^* \rightleftharpoons OCO^*$
6	$OCO^* \rightarrow CO_2 + *$
7	$O_2 + \square \rightarrow O_2\square$
8	$O_2\square + \square \rightarrow 2 O\square$
9	$CO^* + O_2\square \rightarrow CO_2 + O\square + *$
10	$CO^* + O\square \rightarrow CO_2 + \square + *$
11	$CO_2 + O\square \rightleftharpoons CO_3\square$
12	$CO_2 + \ddagger \rightleftharpoons CO_2\ddagger$
$2 CO + O_2 \rightarrow 2 CO_2$	

\* site on noble metal     $\square$  site on ceria     $\ddagger$  site on γ-Al<sub>2</sub>O<sub>3</sub>

mechanism over Pt/ $\gamma$ -Al<sub>2</sub>O<sub>3</sub>. Steps 1 to 6 represent the part of the reaction mechanism occurring on the noble metal surface as discussed in section 4.4.1.

Steps 7 to 10 represent the bifunctional reaction path due to the presence of ceria in the catalyst. At temperatures relevant for this study, oxygen adsorbs molecularly on ceria followed by dissociation (Sass *et al.*, 1986; Li *et al.*, 1989b). Sass *et al.*, (1986) proposed that the reaction with CO proceeds via two parallel paths. CO adsorbed on the noble metal reacts with molecularly adsorbed oxygen, step 9 in Table 5.2, producing CO<sub>2</sub> and O□, and with oxygen adatoms, step 10. The latter is potentially faster than the reaction between CO<sub>2</sub> and O<sub>2</sub>□. From the cyclic feeding experiments it is clear that CO<sub>2</sub> adsorbs significantly on an oxidized ceria surface, step 11 and on alumina, step 12.

At small  $P_{CO}/P_{O_2}$  ratios, CO<sub>2</sub> formation via the Langmuir-Hinshelwood reaction will be the most important pathway, while at high  $P_{CO}/P_{O_2}$  ratios the route via the bifunctional path will become significant. The oxygen adsorption on the noble metal surface is then inhibited by the high degree of CO coverage, leading to a relatively low Langmuir-Hinshelwood reaction rate.

The oxygen vacancies created at the ceria surface can either be filled up by oxygen from the gas phase, step 7 or by diffusion of oxygen from the bulk of ceria.

## 5.4 Conclusions

Cyclic feeding experiments with CO and O<sub>2</sub> showed that oxygen adsorbs on the ceria surface and reacts with CO adsorbed on the noble metal surface via a bifunctional path which occurs parallel to the reaction path for the CO oxidation on alumina supported catalysts.

At a low temperature the amount of oxygen on the ceria surface plays a role only, while at an elevated temperature oxygen diffusion in the bulk ceria results in a significantly CO<sub>2</sub> formation when CO only is fed to the reactor. Ceria acts then as a storage component that releases oxygen under net reducing conditions and is filled up with oxygen under net oxidizing conditions. The oxygen supplied by ceria leads to a higher time-average CO conversion.

Experiments with steam and CO<sub>2</sub> added to the CO and oxygen containing feed stream showed an enhancement of the CO oxidation rate. CO<sub>2</sub> in the feed stream adsorbs on the ceria surface and blocks adsorption sites for oxygen from the gas phase. The reaction via the bifunctional pathway becomes then less important resulting and therefore the role of ceria less pronounced.



## References

- Campman, M., Kinetics of carbon monoxide oxidation over supported platinum catalysts, The role of steam in the presence of ceria, Ph.D. Thesis, Eindhoven University of Technology, 1996
- Engel, T., Ertl, G., Elementary steps in the catalytic oxidation of CO on platinum metals, *Adv. in Catalysis* **28**, 1-78, 1979
- Harrison, B., Diwell, A.F., Hallett, C., Promoting platinum metals by ceria, *Platinum Metals Rev.* **32(2)**, 73-83, 1988
- Heras, J.M., Viscido, L., The behaviour of water on metal surfaces, *Catal. Rev.-Sci. Eng.*, **30(2)**, 281-338, 1988
- Herz, R.K., Dynamic behavior of automotive catalysts. 1. Catalyst oxidation and reduction, *Ind. Eng. Chem. Prod. Res. Dev.* **20**, 451-457, 1981
- Herz, R.K., Kiela, J.B., Sell, J.A., Dynamic behavior of automotive catalysts 2. Carbon monoxide conversion under transient air/fuel conditions, *Ind. Chem. Prod. Res. Dev.* **22**, 387-396, 1983
- Herz, R.K., Sell, J.A., Dynamic behavior of automotive catalysts 3. Transient enhancement of water-gas shift over rhodium, *J. Catal.* **94**, 166-174, 1985
- Jin, T., Okuhara, T., Mains, G.J., White, J.M., Temperature-programmed desorption of CO and CO<sub>2</sub> from Pt/CeO<sub>2</sub>. An important role for lattice oxygen in CO oxidation, *J. Phys. Chem.* **91**, 3310-3315, 1987
- Kim, G., Ceria promoted three-way catalysts for auto exhaust emission control, *Ind. Eng. Chem. Prod. Res. Dev.* **21**, 267-274, 1982
- Li, C., Sakata, Y., Arai, T., Domen, K., Maruya, K., Onishi, T., Carbon monoxide and carbon dioxide adsorption on cerium oxide studied by Fourier-transform infrared spectroscopy, part 1.-Formation of carbonate species on dehydroxylated CeO<sub>2</sub> at Room Temperature, *J. Chem. Soc. Faraday Trans. 1* **85(4)**, 929-943, 1989a
- Li, C., Domen, K., Maruya, K., Onishi, T., Dioxygen adsorption on well-outgassed and partially reduced cerium oxide studied by FT-IR, *J. Am. Chem. Soc.* **111**, 7683-7687, 1989b
- Lynch, D.T., Graham, W.R.C., CO-oxydation on platinum: Variable phasing of inputs during forced composition cycling, *AIChE J.* **36**, 1797-1806, 1990
- Martin, D., Duprez, D., Mobility of surface species on oxides. 1. Isotopic exchange of <sup>18</sup>O<sub>2</sub> with <sup>18</sup>O of SiO<sub>2</sub>, Al<sub>2</sub>O<sub>3</sub>, ZrO<sub>2</sub>, MgO, CeO<sub>2</sub>, and CeO<sub>2</sub>-Al<sub>2</sub>O<sub>3</sub>. Activation by noble metals. Correlation with oxide basicity, *J. Phys. Chem.* **100**, 9429-9438, 1996
- Nunan, J.G., Roberta, H.J., Cohn, M.J., Bradley, S.A., Physicochemical properties of Ce-containing three-way catalysts and the effect of Ce on catalysts activity, *J. Catal.* **133**, 309-324, 1992a

- Oh, S.H.; Eickel, C.C., Effects of Cerium addition on CO oxidation kinetics over Alumina-supported Rhodium catalysts, *J. Catal.* **112**, 1988, 543-555
- Padeste, C., Cant, N.W., Trimm, D.L., The influence of water on the reduction and reoxidation of ceria, *Catal. Lett.* **18**, 305-316, 1993
- Sass, A.S., Kuznetsov, A.V., Shvets, V.A., Savel'eva, G.A., Popova, N.M., Kazanskii, V.B., Luminescence and optical spectroscopic study of the interaction of palladium and cerium in catalysts, *Kinet. Katal.* **26**, 1411-1415, 1985
- Sass, A.S., Shvets, V.A., Savel'era, G.A., Povova, N.M., Kazanskii, V.B., Mechanism of the low-temperature oxidation of CO on applied mixed catalysts containing noble metals and cerium oxide, *Kinet. Katal.* **27**, 894-903, 1986
- Schlatter, J.C., Mitchell, P.J., Three-way catalyst response to transients, *Ind. Eng. Chem. Prod. Res. Dev.* **19**, 288-293, 1980
- Serre, C., Garin, F., Belot, G., Maire, G., Reactivity of Pt/Al<sub>2</sub>O<sub>3</sub> and Pt-CeO<sub>2</sub>/Al<sub>2</sub>O<sub>3</sub> catalysts for the oxidation of Carbon Monoxide by Oxygen I. Catalyst characterization by TPR using CO as reducing agent, *J. Catal.* **141**, 1-8, 1993a
- Serre, C., Garin, F., Belot, G., Maire, G., Reactivity of Pt/Al<sub>2</sub>O<sub>3</sub> and Pt/CeO<sub>2</sub>/Al<sub>2</sub>O<sub>3</sub> catalysts for the oxidation of carbon monoxide by oxygen II. Influence of the pretreatment step on the oxidation mechanism, *J. Catal.* **141**, 9-20, 1993b
- Summers, J.C., Ausen, S.A., Interaction of cerium oxide with noble metals, *J. Catal.* **58**, 131-143, 1979
- Su, E.C., Montreuil, C.N., Rothscild, W.G., Oxygen storage capacity of monolith three-way catalysts, *Appl. Catal.* **17**, 75-86, 1985
- Yao, H.C., Yu Yao, Y.F., Ceria in automotive exhaust catalysts I. Oxygen storage, *J. Catal.* **86**, 254-265, 1984
- Zafiridis G.S., Gorte, R.J., Evidence for a second CO oxidation mechanism on Rh/ceria, *J. Catal.* **143**, 86-91, 1993

# 6

---

## **SIMULATION OF AN AUTOMOTIVE EXHAUST GAS CONVERTER**

### **6.1 Introduction**

To prevent the emissions of harmful components in the exhaust of automotive engines, most cars are equipped with a catalytic converter, the so-called three-way catalyst, which is located in the exhaust pipe. The converter is usually a monolith, a block of ceramic material with several thousands of parallel channels. The channels are coated with an alumina washcoat which serves as support of the noble metals, usually platinum, rhodium and sometimes palladium, and considerable amounts of ceria as well as small amounts of additives.

Car and catalyst manufacturers put much effort in reducing the emission of pollutants to meet the ever more stringent standards. Both engine construction improvements and new catalyst developments are necessary to achieve ultra low emission vehicles. Optimisation of the existing catalysts is facilitated by knowledge of the underlying reaction kinetics, while insights obtained from reactor modelling can be used to optimise the performance as a function of the operating conditions.

To allow simultaneously the oxidation of CO and hydrocarbons and the reduction of NO, a fuel control system is applied to keep the engine's exhaust gas composition close to the stoichiometric value. The delay time in the feedback loop of the control system leads to an oscillating exhaust composition around the stoichiometric point at a typical frequency of 1 Hz. Hence, in modelling the dynamic behaviour of the reactor under typical exhaust conditions, detailed kinetic models based on elementary steps have to be used, since the frequency of the oscillation is of the same order as the

turnover frequency of the occurring reactions and therefore no quasi-steady state approximation can be used.

In this chapter the catalytic converter is modelled under both steady state and dynamic conditions. The results of the simulations with a cyclic feed will be used to calculate the effects of the oscillations on the time-average conversions.

## 6.2 Kinetic model

### 6.2.1 Reaction mechanism

In modelling the exhaust gas converter propane and propene are frequently used as model components for hydrocarbons. However, they are not suited to simulate the behaviour under typical exhaust gas compositions as they do not affect the light-off temperature of the CO oxidation and the NO reduction (Mabilon, *et al.*, 1995). As reported in the literature, the presence of hydrocarbons in real exhaust gas retards the light-off of CO and NO (Mabilon *et al.*, 1995). In the modelling discussed in this chapter ethyne and ethene are used as model hydrocarbons. Ethyne is chosen since it is present in quantities (about 20 mol%, Impels, 1987) that substantially retard the oxidation of CO and reduction of NO due to inhibition (Mabilon *et al.*, 1995). Ethene is chosen as a representative for all organic species except ethyne and methane because it is also present in relatively high quantities in exhaust gas (25 mol%, Impels, 1987), and its ease of oxidation is similar to that of aromatics and oxygenated organic species. As methane is difficult to oxidise, it is often considered as inert with respect to exhaust gas treatment.

The kinetic model, see Table 6.1, for the reactions between CO, O<sub>2</sub>, NO, C<sub>2</sub>H<sub>4</sub> and C<sub>2</sub>H<sub>2</sub> was constructed from literature data. Basically the steps involving CO, NO and O<sub>2</sub>, denoted by pathways  $\sigma_1$  to  $\sigma_3$ , were taken from Oh *et al.* (1986). In pathway  $\sigma_1$  the route for the CO<sub>2</sub> formation via the CO oxidation with oxygen is given. Two different pathways lead to the N<sub>2</sub> formation: the reaction of adsorbed nitrogen with adsorbed NO,  $\sigma_2$ , and the recombination of N adatoms,  $\sigma_3$ . Both ethene and ethyne oxidation were based on the work of Sant *et al.* (1989). They proposed two models for the ethene oxidation: a model for low oxygen conditions which uses adsorbed CO as an intermediate and a model for high oxygen concentrations which uses a direct pathway to the CO<sub>2</sub> formation. In the present kinetic model, ethene oxidation was based on the model for low oxygen concentrations, since ethene light-off typically occurs after ethyne and CO oxidation and therefore most of the oxygen has reacted. As data for ethyne oxidation were not available at all, the ethene oxidation model for high oxygen concentration was applied for ethyne as its conversion is expected near the reactor entrance, before the conversion of the other components. The sticking probability of

Table 6.1.

'Elementary steps' and reaction pathways, indicated by the stoichiometric numbers  $\sigma_i$ , for exhaust gas conversion.

	$\sigma_1$	$\sigma_2$	$\sigma_3$	$\sigma_4$	$\sigma_5$
$\text{CO} + * \xrightleftharpoons[k_{d,\text{CO}}]{k_{a,\text{CO}}} \text{CO}^*$	2	2	2	0	0
$\text{O}_2 + 2* \xrightleftharpoons[k_{d,\text{O}_2}]{k_{a,\text{O}_2}} 2\text{O}^*$	1	0	0	3	5
$\text{NO} + * \xrightleftharpoons[k_{d,\text{NO}}]{k_{a,\text{NO}}} \text{NO}^*$	0	2	2	0	0
$\text{C}_2\text{H}_4 + 2* \xrightleftharpoons[k_{d,\text{C}_2\text{H}_4}]{k_{a,\text{C}_2\text{H}_4}} \text{C}_2\text{H}_4^{**}$	0	0	0	1	0
$\text{C}_2\text{H}_2 + 4* \xrightleftharpoons[k_{d,\text{C}_2\text{H}_2}]{k_{a,\text{C}_2\text{H}_2}} \text{C}_2\text{H}_2^{****}$	0	0	0	0	2
$\text{NO}^* + * \xrightarrow{k_{\text{diss}}} \text{N}^* + \text{O}^*$	0	1	2	0	0
$\text{CO}^* + \text{O}^* \xrightarrow{k_{\text{CO}_2}} \text{CO}_2 + 2*$	2	2	2	2	0
$\text{NO}^* + \text{N}^* \xrightarrow{k_{\text{N}_2,1}} \text{N}_2 + \text{O}^* + *$	0	1	0	0	0
$2\text{N}^* \xrightarrow{k_{\text{N}_2,2}} \text{N}_2 + 2*$	0	0	1	0	0
$\text{C}_2\text{H}_4^{**} + 4\text{O}^* \xrightarrow{k_{\text{H}_2\text{O},1}} 2\text{CO}^* + 2\text{H}_2\text{O} + 4*$	0	0	0	1	0
$\text{C}_2\text{H}_2^{****} + 5\text{O}^* \xrightarrow{k_{\text{H}_2\text{O},2}} 2\text{CO}_2 + \text{H}_2\text{O} + 9*$	0	0	0	0	2
<p>1: <math>\sigma_1</math>: <math>2\text{CO} + \text{O}_2 \rightarrow 2\text{CO}_2</math></p> <p>2: <math>\sigma_2, \sigma_3</math>: <math>2\text{CO} + 2\text{NO} \rightarrow 2\text{CO}_2 + \text{N}_2</math></p> <p>3: <math>\sigma_4</math>: <math>\text{C}_2\text{H}_4 + 3\text{O}_2 \rightarrow 2\text{CO}_2 + 2\text{H}_2\text{O}</math></p> <p>4: <math>\sigma_5</math>: <math>2\text{C}_2\text{H}_2 + 5\text{O}_2 \rightarrow 4\text{CO}_2 + 2\text{H}_2\text{O}</math></p>					

\* stands for catalytic site

ethene and the surface reaction rate constant  $k_{\text{H}_2\text{O},2}$  of the model of Sant *et al.* (1989) for high oxygen concentrations were adapted, however, to describe the light-off data from Mabilon *et al.* (1995).

The global reactions shown in Table 6.1 correspond with the minimal number of reactions which has to be taken into account. From a mathematical point of view they can be regarded as a base for the space including all possible reactions. The reaction between e.g. NO and  $\text{C}_2\text{H}_4$  or  $\text{C}_2\text{H}_2$  can also take place and is a linear combination of the global reactions given in Table 6.1, as well as of the appropriate 'elementary steps'.

### 6.2.2 Rate equations

Adsorption of oxygen is assumed as irreversible and dissociative with a rate proportional to the fraction of vacant sites (Oh *et al.*, 1986). In contrast to Sant *et al.* (1989) adsorption of both ethene and ethyne is also assumed to be first order in the vacant sites. The adsorption rate of component  $i$  ( $i = \text{CO}$ ,  $\text{O}_2$ ,  $\text{NO}$ ,  $\text{C}_2\text{H}_4$  or  $\text{C}_2\text{H}_2$ ) is given by:

$$r_{a,i} = k_{a,i} L_i C_i \theta_* \quad (6.1)$$

where the fraction of vacant catalytic sites is given by:

$$\theta_* = 1 - \theta_{\text{CO}} - \theta_{\text{O}} - \theta_{\text{NO}} - \theta_{\text{N}} - \theta_{\text{C}_2\text{H}_4} - \theta_{\text{C}_2\text{H}_2} \quad (6.2)$$

The fractional coverage  $\theta$  of the surface species is defined by the ratio of the sites occupied by a species to the total number of active sites. Hence, according to Table 6.1, for the adsorption of one molecule ethyne are four vacant sites are needed, and for one molecule ethene two vacant sites:

$$\theta_{\text{C}_2\text{H}_2} = \frac{4 L_{\text{C}_2\text{H}_2}}{L_t}, \quad \theta_{\text{C}_2\text{H}_4} = \frac{2 L_{\text{C}_2\text{H}_4}}{L_t} \quad (6.3)$$

The adsorption rate coefficients are obtained from the kinetic gas theory:

$$k_{a,i} = \frac{1}{L_t} \sqrt{\frac{RT}{2\pi M_i}} s_i^0 \quad (6.4)$$

where  $s_i^0$  is the sticking probability on a clean surface.

The behaviour of the converter at low temperatures only is simulated ( $T < 500$  K), i.e. just before and after the light-off temperature of the components, hence the

**Table 6.2**  
**Kinetic parameters and corresponding references.**

parameter		value	reference
$s_{CO}^0$	/-	0.5	Oh <i>et al.</i> (1986)
$A_{d,CO}$	/s <sup>-1</sup>	$1.6 \cdot 10^{14}$	Oh <i>et al.</i> (1986)
$E_{d,CO}^{1)}$	/kJ mol <sup>-1</sup>	112	Oh <i>et al.</i> (1986)
$s_{O_2}^0$	/-	0.01	Oh <i>et al.</i> (1986)
$s_{NO}^0$	/-	0.5	Oh <i>et al.</i> (1986)
$A_{d,NO}$	/s <sup>-1</sup>	$5 \cdot 10^{13}$	Oh <i>et al.</i> (1986)
$E_{d,NO}$	/kJ mol <sup>-1</sup>	108.7	Oh <i>et al.</i> (1986)
$s_{C_2H_4}^0$	/-	0.35	Sant <i>et al.</i> (1989)
$A_{d,C_2H_4}$	/s <sup>-1</sup>	1013	Sant <i>et al.</i> (1989)
$E_{d,C_2H_4}$	/kJ mol <sup>-1</sup>	57.3	Sant <i>et al.</i> (1989)
$s_{C_2H_2}^0$	/-	1	Palmer (1977)
$A_{d,C_2H_2}$	/s <sup>-1</sup>	$6.5 \cdot 10^{13}$	Sant <i>et al.</i> (1989)
$E_{d,C_2H_2}$	/kJ mol <sup>-1</sup>	115	Sant <i>et al.</i> (1989)
$A_{diss}$	/s <sup>-1</sup>	$3 \cdot 10^{10}$	Oh <i>et al.</i> (1986)
$E_{diss}$	/kJ mol <sup>-1</sup>	79.4	Oh <i>et al.</i> (1986)
$A_{CO_2}$	/s <sup>-1</sup>	1012	Oh <i>et al.</i> (1986)
$E_{CO_2}$	/kJ mol <sup>-1</sup>	60	Oh <i>et al.</i> (1986)
$A_{N_2,1}$	/s <sup>-1</sup>	$2 \cdot 10^9$	Oh <i>et al.</i> (1986)
$E_{N_2,1}^{2)}$	/kJ mol <sup>-1</sup>	87.8	Oh <i>et al.</i> (1986)
$A_{N_2,2}$	/s <sup>-1</sup>	$3 \cdot 10^{10}$	Oh <i>et al.</i> (1986)
$E_{N_2,2}$	/kJ mol <sup>-1</sup>	120	Oh <i>et al.</i> (1986)
$A_{H_2O,1}$	/s <sup>-1</sup>	$6.0 \cdot 10^{13}$	Sant <i>et al.</i> (1989)
$E_{H_2O,1}$	/kJ mol <sup>-1</sup>	62.7	Sant <i>et al.</i> (1989)
$A_{H_2O,2}^{3)}$	/s <sup>-1</sup>	1012	Oh <i>et al.</i> (1986)
$E_{H_2O,2}$	/kJ mol <sup>-1</sup>	54.3	Sant <i>et al.</i> (1989)

<sup>1)</sup> Oh *et al.*, (1986) used for the CO desorption activation energy:  $132 - 19 \theta_{CO} - 42 \theta_N$   
<sup>2)</sup> Oh *et al.*, (1986) used for the recombination of N adatoms as activation energy:  $130 - 17 \theta_N$   
<sup>3)</sup> The frequency factor for ethyne oxidation is increased from  $8 \cdot 10^7 \text{ s}^{-1}$  (Sant *et al.*, 1989) to  $10^{12} \text{ s}^{-1}$  (Oh *et al.*, 1986), reflecting the much higher oxidation rate of ethyne compared to ethene.

desorption rate of oxygen can be neglected (Engel and Ertl, 1979). The desorption rate of any other adsorbed species  $j$  ( $j = \text{CO}^*$ ,  $\text{NO}^*$ ,  $\text{C}_2\text{H}_4^{**}$  or  $\text{C}_2\text{H}_2^{****}$ ) is proportional to the surface coverage and given by:

$$r_{d,j} = k_{d,j} L_i \theta_j \quad (6.5)$$

The rate of NO dissociation is expressed as:

$$r_{\text{diss}} = k_{\text{diss}} L_i \theta_{\text{NO}} \theta_{\cdot} \quad (6.6)$$

The rate of the surface reactions  $l$  ( $l = \text{CO}_2$ ,  $\text{N}_2$ , 1,  $\text{N}_2$ , 2  $\text{H}_2\text{O}$ , 1 and  $\text{H}_2\text{O}$ , 2, see Table 6.1) leading to the formation of  $\text{CO}_2$ ,  $\text{N}_2$  and  $\text{H}_2\text{O}$  respectively, is considered as proportional to the product of the involved surface coverages  $\theta_x$  and  $\theta_y$  ( $x, y = \text{CO}^*$ ,  $\text{O}^*$ ,  $\text{NO}^*$ ,  $\text{N}^*$ ,  $\text{C}_2\text{H}_4^{**}$  or  $\text{C}_2\text{H}_2^{****}$ ):

$$r_l = k_l L_i \theta_x \theta_y \quad (6.7)$$

It is clear from Equations 6.1, 6.3, 6.5 and 6.7 that the corresponding 'elementary steps' in Table 6.1 are assumed to consist of a set of steps with a rate determining step involving a single active site.

Rate coefficients for desorption, dissociation and surface reactions are Arrhenius-type expressions. The kinetic parameter values and corresponding references as used in this study, are shown in Table 6.2.

As a kinetic model for both the CO oxidation and the NO reduction as well as the oxidation of hydrocarbons was not available, kinetic models from the literature for the reaction between CO, NO and  $\text{O}_2$  and for  $\text{C}_2\text{H}_2$  and  $\text{C}_2\text{H}_4$  oxidation have been used to model the exhaust gas converter. After adaptation of the sticking probability and the surface reaction constant of ethyne not only the experimental data van Mabilon *et al.*, (1995) could be described but also the experimental data shown in Chapter 4. Therefore, instead of adapting the kinetic model presented in Chapter 4 to account for the oxidation of hydrocarbons and the NO reduction, a kinetic model based on literature data was used to model the converter.

## 6.3 Reactor model

### 6.3.1 Assumptions

The adiabatic model of the monolithic converter is based on the one-dimensional model reported by Lie (1992). For both the gas phase and the solid phase, only axial



concentration and temperature gradients are considered. Heat and mass transport resistances are located at the interface between bulk gas phase and the washcoat, see also Figure 6.1. For the Sherwood and Nusselt numbers corresponding to these processes the asymptotic values of 3.66 are taken. Derivation of mass and heat transfer coefficients from these numbers is given in Appendix 6A. From comparisons of this one-dimensional film model and the fundamental Graetz-Nusselt model, Leclerc and Schweich (1993) concluded that the models are probably indistinguishable in practice.

More specifically, the model equations are based on the following assumptions:

- The radial velocity distribution is uniform. In practice the flow in the outer channels might be lower than in the inner channels due to a short divergent inlet of the monolith (Zygourakis, 1989; Eigenberger and Nieken, 1991; Cybulski and Moulijn, 1994).
- The reactor operates adiabatically, since the converter in the exhaust line is thermally insulated.
- The walls of the channels are impenetrable to gas and all channels have equal diameters.

As a result of these assumptions all channels are equal and model equations for one channel only have to be derived to predict the behaviour of the monolith.

Other assumptions are:

- Axial mass diffusion and axial heat conduction in the gas phase is neglected, since the Péclet number is larger than 50.
- Axial mass diffusion in the washcoat is neglected.
- The thermal conductivities of washcoat and ceramic are equal.
- The flow in the channels is laminar, since the Reynolds number is less than 300. Plug flow behaviour is assumed nevertheless in view of the small channel diameter, since radial profiles are flattened by molecular diffusion (Taylor, 1953).
- Entrance effects are neglected, as the hydrodynamic entrance length is only a fraction of the total length of the converter.
- Pore diffusion limitation is neglected (Hayes and Kolaczowski, 1994).
- The gas is ideal with a constant average molecular mass, since the molar concentrations of the reactive components are very low.
- Pressure drop is neglected, as it amounts to about 1 kPa according to the Hagen-Poiseuille equation (Villermaux and Schweich, 1994).

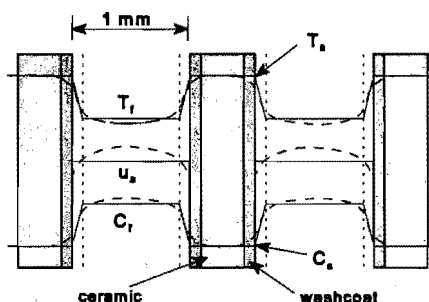


**Figure 6.1**  
**Actual profiles (dotted lines) as well as the assumed profiles (full lines) in the channels of the monolith.**

Figure 6.1 shows the actual and the assumed profiles in the monolith channels.

### 6.3.2 Continuity equations

The model for the converter consists of a set of continuity equations for the reactants in the bulk gas phase and in the pores of the washcoat, as well energy equations for the bulk gas phase and the solid phase. Accumulation of mass on the catalytic surface is accounted for by continuity equations for the adsorbed species. It is not necessary to calculate the product concentrations since the continuity equations of the reactants are independent of them.

The continuity equation for reactant  $i$  ( $i = \text{CO}, \text{O}_2, \text{NO}, \text{C}_2\text{H}_4, \text{ or } \text{C}_2\text{H}_2$ ) in the bulk gas phase is given by:

$$\varepsilon \rho_f \frac{\partial}{\partial t} \left( \frac{C_{f,i}}{\rho_f} \right) = - \phi_m^{\text{sup}} \frac{\partial}{\partial x} \left( \frac{C_{f,i}}{\rho_f} \right) - \rho_f k_{f,i} a_v \left( \frac{C_{f,i}}{\rho_f} - \frac{C_{s,i}}{\rho_f} \right) \quad (6.8)$$

where  $\phi_m^{\text{sup}} = G/A_s$ .

For reactant  $i$  in the pores of the washcoat it is given by:

$$\varepsilon_w \rho_f \frac{4 \varepsilon d_w}{d_b} \frac{\partial}{\partial t} \left( \frac{C_{s,i}}{\rho_f} \right) = \rho_f k_{f,i} a_v \left( \frac{C_{f,i}}{\rho_f} - \frac{C_{s,i}}{\rho_f} \right) - a_{\text{cat}} R_i \quad (6.9)$$

The dependent variables are expressed as  $C/\rho_f$  to correct for density changes as a function of the axial coordinate due to non-uniform temperatures

The continuity equation for surface species  $j$  ( $j = \text{CO}^*, \text{O}^*, \text{NO}^*, \text{N}^*, \text{C}_2\text{H}_4^{**}, \text{ or } \text{C}_2\text{H}_2^{****}$ ) is given by:

$$L_t \frac{\partial \theta_j}{\partial t} = R_j \quad (6.10)$$

The enthalpy equations for the gas phase and for the solid phase are given by:

$$\varepsilon \rho_f c_{pf} \frac{\partial T_f}{\partial t} = - \phi_m^{\text{sup}} c_{pf} \frac{\partial T_f}{\partial x} - \alpha a_v (T_f - T_s) \quad (6.11)$$

$$(1-\varepsilon) \rho_s c_{ps} \frac{\partial T_s}{\partial t} = \lambda_s (1-\varepsilon) \frac{\partial^2 T_s}{\partial x^2} + \alpha a_v (T_f - T_s) + a_{\text{cat}} \sum_{k=1}^4 (-\Delta_r H)_{\alpha_k} r_k \quad (6.12)$$

where  $r_k$  gives the rates of the global reactions, see Table 6.1. The rate of the global reaction between CO and oxygen  $r_1$  is calculated from the net CO disappearance rate due to sorption and the rate of the global reaction between NO and CO.

$$\begin{aligned} r_1 &= r_{a,CO} - r_{d,CO} - r_2 \\ r_2 &= r_{a,NO} - r_{d,NO} \\ r_3 &= r_{a,C_2H_4} - r_{d,C_2H_4} \\ r_4 &= r_{a,C_2H_2} - r_{d,C_2H_2} \end{aligned} \quad (6.13)$$

The heat production is calculated from the reaction enthalpies of the global reactions given in Table 6.1. This is allowed, since temperature oscillations due to the time dependent heat production as a result of the changing surface coverages are negligible (van Selow, 1996).

Boundary conditions for the bulk gas concentrations are given by the inlet concentrations:

$$C_{f,i}(0,t) = \bar{C}_{f,i}^{\text{in}} [1 + B \sin(2\pi f t + \phi)] \quad t \geq 0 \quad (6.14)$$

where  $\phi = 0$  for CO,  $C_2H_2$  and  $C_2H_4$ , and  $\phi = \pi$  for  $O_2$  and NO, indicating that the former and the latter oscillate in counter phase.

For the gas phase temperature the boundary condition at the inlet is defined by:

$$T_f(0,t) = T_f^{\text{in}} \quad t \geq 0 \quad (6.15)$$

while for the solid phase zero fluxes are assumed at the reactor inlet and outlet:

$$\frac{\partial T_s(0,t)}{\partial x} = 0, \quad \frac{\partial T_s(L,t)}{\partial x} = 0 \quad t \geq 0 \quad (6.16)$$

The initial conditions are imposed by the assumption that the reactor operates in steady state before the feed oscillation starts. Hence, for the concentrations of reactant  $i$  ( $i = \text{CO}, O_2, \text{NO}, C_2H_4$ , or  $C_2H_2$ ) in the bulk gas phase and in the solid phase they are given by:

$$C_{f,i}(x,0) = C_{f,i}^{\text{ss}}(x), \quad C_{s,i}(x,0) = C_{s,i}^{\text{ss}}(x) \quad 0 \leq x \leq L \quad (6.17)$$

and for the surface coverage of species  $j$  ( $j = \text{CO}^*, O^*, \text{NO}^*, N^*, C_2H_4^{**}$ , or  $C_2H_2^{****}$ ) by:

$$\theta_j(x,0) = \theta_j^{\text{ss}}(x) \quad 0 \leq x \leq L \quad (6.18)$$

Initial conditions for the bulk gas phase temperature and the solid phase temperature are:

$$T_f(x,0) = T_f^{ss}(x), T_s(x,0) = T_s^{ss}(x) \quad 0 \leq x \leq L \quad (6.19)$$

The reactor parameters at a temperature of 500 K are listed in Table 6.3.

**Table 6.3.**

**Reactor parameters at  $T = 500$  K (Nievergeld, 1994).**

parameter	value	parameter	value
$\varepsilon$	$/m_i^3 m_R^{-3}$ 0.6	$A_s$	$/m_R^2$ $6.0 \cdot 10^{-3}$
$\phi_m^{\text{sup}}$	$/\text{kg } m_R^{-2} \text{ s}^{-1}$ 5.83	$c_{pf}$	$/\text{J kg}^{-1} \text{ K}^{-1}$ $1.081 \cdot 10^3$
$\rho_f$	$/\text{kg } m_i^{-3}$ 0.68	$c_{ps}$	$/\text{J kg}^{-1} \text{ K}^{-1}$ $1.015 \cdot 10^3$
$\rho_s$	$/\text{kg } m_s^{-3}$ $2.5 \cdot 10^3$	$\lambda_f$	$/\text{W m}^{-1} \text{ K}^{-1}$ $3.86 \cdot 10^{-2}$
Sh, Nu	/- 3.66	$\lambda_s$	$/\text{W m}^{-1} \text{ K}^{-1}$ 1.675
$k_{f,\text{CO}}, k_{f,\text{O}_2}$	$/m_i^{-3} m_i^{-2} \text{ s}^{-1}$ 0.18	$\alpha$	$/\text{W m}^{-2} \text{ K}^{-1}$ 141
$k_{f,\text{NO}}$	$/m_i^{-3} m_i^{-2} \text{ s}^{-1}$ 0.21	$(-\Delta_f H)_{\text{CO}}$	$/\text{J mol}^{-1}$ $283 \cdot 10^3$
$k_{f,\text{C}_2\text{H}_4}, k_{f,\text{C}_2\text{H}_2}$	$/m_i^{-3} m_i^{-2} \text{ s}^{-1}$ 0.14	$(-\Delta_f H)_{\text{C}_2\text{H}_4}$	$/\text{J mol}^{-1}$ $373 \cdot 10^3$
$\varepsilon_w$	$/m_i^3 m_w^{-3}$ 0.4	$(-\Delta_f H)_{\text{C}_2\text{H}_2}$	$/\text{J mol}^{-1}$ $1322 \cdot 10^3$
$a_v$	$/m_i^2 m_R^{-3}$ $2.4 \cdot 10^3$	$(-\Delta_f H)_{\text{C}_2\text{H}_2}$	$/\text{J mol}^{-1}$ $1254 \cdot 10^3$
$d_b$	$/m_R$ $1.0 \cdot 10^{-3}$	$L_i$	$/\text{mol } m_{\text{NM}}^{-2}$ $2.7 \cdot 10^{-5}$
$d_w$	$/m_R$ $2.5 \cdot 10^{-5}$	$a_{\text{cat}}$	$/m_{\text{NM}}^2 m_R^{-3}$ $1.25 \cdot 10^4$
L	$/m_R$ 0.15	B	/- 0.15

### Numerical methods

The model for the converter consists of a coupled set of partial and ordinary differential equations which is solved with the package PDECOL (Madsen and Sincovec, 1979). The method implemented in this package is based on the methods of lines and uses finite element orthogonal collocation for discretization in the axial direction. Piecewise polynomials (splines) are used as base functions. The internal collocation points of the elements follow from the zeros of Legendre polynomials. Application of the method of lines to the model equations transforms the partial

differential equations to a (larger) set of initial value ordinary differential equations. The latter is solved using the Backward Differentiation Formulae (BDF) with variable order and variable step size.

In solving the model equations the axial direction is divided into 40 elements and on each of these elements 4th order splines are used as base functions. Typical computation over a period of 10 seconds required 300 seconds of CPU time on a Silicon Graphics Power Challenge

## 6.4 Results and discussion

Both steady state and cyclic feeding simulations have been performed. The latter allow the calculation of the oscillatory effects on the time average performance. Time-average inlet concentrations and the corresponding equivalence ratio  $\lambda$ , defined by the ratio  $(A/F)$  to  $(A/F)_{\text{stoich}}$ , are given in Table 6.4. The inlet concentrations are derived from the non-linear engine behaviour as a function of the air/fuel ratio as reported by (Taylor and Sinkevitch, 1983). During all simulations the mass flow rate is kept at a typical

**Table 6.4**

**Equivalence ratio  $\lambda$  and the corresponding time-average inlet concentrations**

$\lambda$ -	CO vol%	O <sub>2</sub> vol%	NO ppm	C <sub>x</sub> H <sub>y</sub> <sup>a</sup> ppm	$\lambda$ -	CO vol%	O <sub>2</sub> vol%	NO ppm	C <sub>x</sub> H <sub>y</sub> <sup>a</sup> ppm
0.94	1.41	0.32	637	615	1	0.5	0.48	1000	500
0.95	1.21	0.34	678	593	1.01	0.41	0.51	1088	485
0.96	1.03	0.36	727	572	1.02	0.33	0.54	1182	472
0.97	0.87	0.39	782	552	1.03	0.27	0.58	1280	461
0.98	0.73	0.42	846	534	1.04	0.22	0.62	1379	451
0.99	0.61	0.44	919	516					

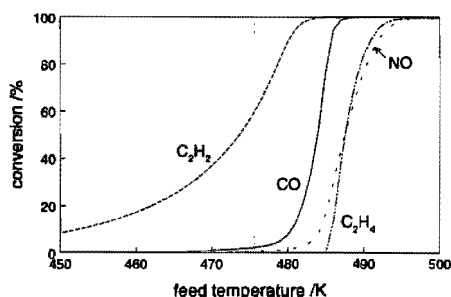
<sup>a</sup> C<sub>x</sub>H<sub>y</sub> = C<sub>2</sub>H<sub>2</sub> or C<sub>2</sub>H<sub>4</sub>

value of 10<sup>-2</sup> kg/s; the amplitude of all reactants is set at 15% of the time-average inlet concentrations. The oxidizing reactants are oscillating out-of-phase with the reducing components, *i.e.* the phase shift between them amounts to  $\pi$ .

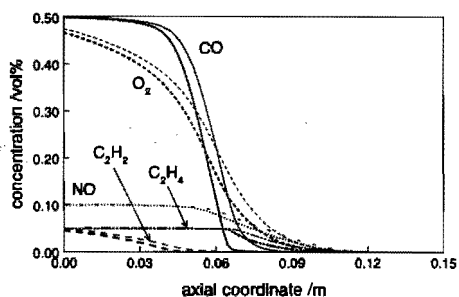
### 6.4.1 Steady state

Figure 6.2 shows the light-off curves of all four pollutants in the mixture. Ethyne is oxidized first, followed by CO above 480 K. When most CO has reacted the

conversion of ethene and NO starts simultaneously. From this figure it is clear that the reactions take place in the sequence:  $C_2H_2 < CO < NO + C_2H_4$ . This is also shown in Figure 6.3 in which the bulk gas concentrations and the concentrations in the pores of the washcoat as a function of the axial coordinate at a feed temperature of 500 K are depicted. In the first part of the reactor ethyne is converted. When most ethyne has reacted, the CO oxidation starts followed by both the NO reduction and the  $C_2H_4$  oxidation. As is clear from the oxygen profile, initially oxygen reacts with  $C_2H_2$  and CO whereas the reaction with NO takes place after all  $C_2H_2$  has reacted. Pattas *et al.* (1994) showed that 20% of the hydrocarbons



**Figure 6.2**  
**Outlet concentrations versus feed temperature.** Conditions:  $\lambda = 1$ , Tables 6.3 and 6.4.



**Figure 6.3**  
**Concentration versus axial coordinate at a feed temperature of 500 K.** Thin line: bulk gas phase; thick: line pores of the washcoat. Conditions:  $\lambda = 1$ , Tables 6.3 and 6.4.

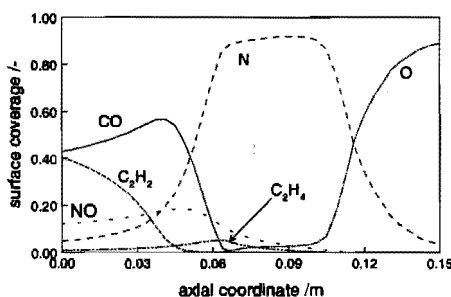


**Figure 6.4**  
**Surface coverage versus axial coordinate at a feed temperature of 500 K.** Conditions:  $\lambda = 1$ , Tables 6.3 and 6.4.

are converted before the CO oxidation starts, which is in line with the alkyne oxidation as the alkyne content of exhaust gas is typical 20% of the total organics (Impens, 1987). From Figure 6.3 it is also clear that significant mass transfer limitations are absent at this temperature, except for CO and  $O_2$  in the region of high conversion rates. Furthermore it is also clear from this figure that the reaction between NO and  $C_2H_4$  takes place significantly when most of CO,  $O_2$  and  $C_2H_2$  is converted.

The strict reaction sequence can be understood from the corresponding axial surface coverage profiles shown in Figure 6.4. In the first part of the reactor mainly ethyne and CO compete for the active sites and inhibit the adsorption of oxygen and ethene. There is also some NO adsorption and dissociation. After all  $C_2H_2$  and CO has reacted, vacant sites become available for the adsorption of  $C_2H_4$ , and also more NO adsorption and dissociation can occur. The latter leads to a higher degree of nitrogen coverage only since the extra adsorbed oxygen due to NO dissociation reacts immediately with surface ethene. When almost all pollutants are converted, the surface becomes oxygen covered.

In Figure 6.5 the axial temperature profiles of the gas and the solid phase are shown. The solid temperature is slightly, about 10 K at most, higher than the bulk gas temperature due to the heat of reaction. The maximum temperature rise across the reactor equals the adiabatic temperature rise amounting to 94 K. At elevated feed temperatures the reactant conversions move more to the front part of the reactor and the temperature profiles become almost uniform over the entire length of the reactor.

#### 6.4.2 Light-off behaviour

A step increase in feed temperature from 300 to 550 K causes reactor light-off. The evolution of the axial solid phase temperature profiles in the reactor are shown in Figure 6.6. Initially the converter is heated by convective energy transfer only, so that the solid temperature is highest at the inlet. It takes more than 120 seconds to approach the steady state temperature profiles shown in Figure 6.5 because of the large heat capacity of the solid phase.

Simulations performed without heat conductivity in the solid phase showed

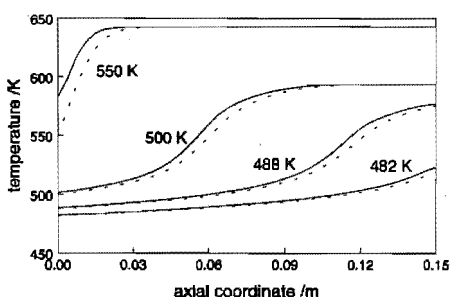


**Figure 6.5**  
*Temperature of the gas and the solid phase versus axial coordinate at four feed temperatures. Dotted lines: gas phase; solid lines: solid phase. Conditions:  $\lambda = 1$ , Tables 6.3 and 6.4.*

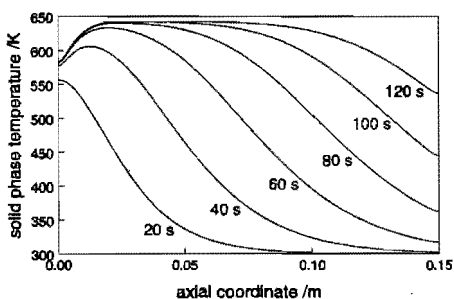


**Figure 6.6**  
*Evolution of the axial temperature profiles of the solid phase after a step increase of the feed temperature from 300 to 550 K. Conditions:  $\lambda = 1$  and Tables 6.3 and 6.4.*

identical profiles to the ones in Figure 6.6. Leighton and Chang (1995) showed theoretically that the temperature front during light-off is smoothed by an effective Taylor-Aris dispersion phenomenon. This apparent dispersion is significantly larger than the solid thermal diffusivity of the ceramic converter and therefore heat conductivity of the solid phase plays no role during light-off.

Figure 6.7 shows the conversion of the pollutants as a function of time as a result of a step increase of the feed temperature from 300 K to 550 K. In this figure a similar conversion sequence of the pollutants is visible as in Figure 6.2. When the ethyne conversion starting after about 10 s is considerable, the CO oxidation begins. After 50 s conversion of both NO and  $C_2H_4$  is completed. At this point a steady state has not yet been reached since the temperature in the second half of the reactor is still increasing, as shown in Figure 6.6. The first half of the reactor, however, has reached sufficiently high temperatures as to allow full pollutant conversions, in line with the results in Figure 6.3. The shoulder in the NO conversion is caused by strongly increased NO adsorption when the CO oxidation is complete and more vacant sites becoming available.

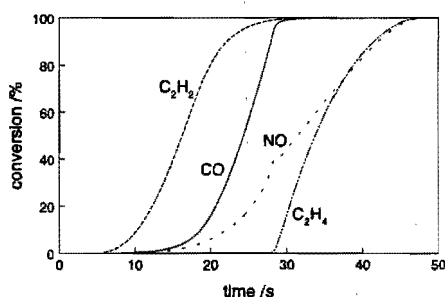


**Figure 6.7**  
**Conversions versus time after a step increase of the feed temperature from 300 K to 550 K. Conditions:  $\lambda = 1$ , Tables 6.3 and 6.4.**

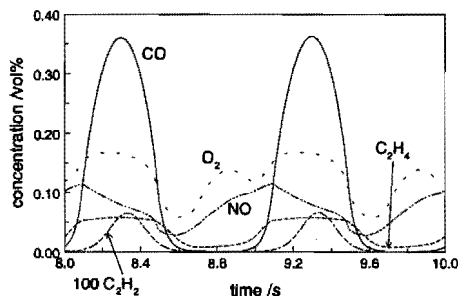
### 6.4.3 Cyclic feeding

Figure 6.8 shows the gas phase outlet concentrations as a function of time when the inlet concentrations are cycled at a typical frequency of 1 Hz. Since the oscillation is started from the steady state, there is a transition to a stable oscillation. The latter takes about 8 s and is not shown in Figure 6.8. The concentrations in the pores of the washcoat are not shown either but they oscillate in phase with the corresponding gas phase concentrations.

The amplitude of all concentrations except for  $O_2$  increases towards the outlet of the reactor. Hydrocarbons and CO concentrations remain in phase with the inlet, but the NO and oxygen outlet concentrations oscillate out of phase with respect to the inlet concentrations. During the net reducing part of the period the minimum of the oxygen inlet concentration turns into a maximum as also reported by Lie *et al.* (1993) for the CO oxidation with oxygen and by Nievergeld *et al.* (1995) for the reaction between CO, NO and oxygen. During the net oxidizing part the oxygen concentration shows a local



maximum. The minima of the outlet NO concentration coincide with the global oxygen minima, but the NO maxima are shifted in time with respect to the oxygen maxima.



**Figure 6.8**  
**Outlet concentrations versus time during 1 Hz cycling.** Conditions:  $\lambda = 1$ ,  $T_r = 485$  K, Tables 6.3 and 6.4.

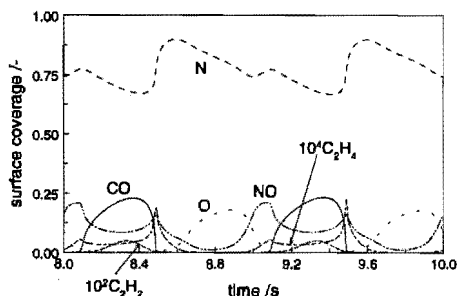


**Figure 6.9**  
**Outlet surface coverages versus time during 1 Hz cycling.** Conditions:  $\lambda = 1$ ,  $T_r = 485$  K, Tables 6.3 and 6.4.

The increase of the amplitudes can be understood from the outlet surface coverages shown in Figure 6.9. When the concentration of the reducing components increases, mainly the higher degree of CO coverage leads to stronger inhibition of the other components. The resulting lower degree of coverages of NO, N and O causes lower reaction rates. In contrast, when the concentration of the reducing components starts to decrease, the coverages of the strongly adsorbing components CO and  $C_2H_2$  decrease also and more vacant sites become available. The resulting higher adsorption rates of NO,  $O_2$ , and  $C_2H_4$  lead to higher surface coverages of NO,  $C_2H_4$  and N, the latter due to higher rate of NO dissociation, and corresponding higher surface reaction rates. The extra adsorbed oxygen reacts immediately with adsorbed CO and  $C_2H_4$ . Hence, the out-of-phase oscillation of the reaction rates with respect to the CO,  $C_2H_4$  and  $C_2H_2$  gas phase concentrations leads to an increasing amplitude of the corresponding components as a function of the reactor coordinate, while the in-phase oscillation with respect to oxygen leads to a smaller amplitude for  $O_2$ . This effect is further enhanced by the counter phase oscillation of the oxygen/NO gas phase concentrations versus those of CO/hydrocarbons. When the surface coverage of the reducing components becomes very low the oxidation reactions stop and the degree of oxygen coverage increases. The surface becomes almost totally covered with nitrogen and oxygen adatoms and the  $O_2$  and NO gas phase concentrations start to increase.

### 6.4.4 Effects of cyclic feeding on the time-average conversions

Several experimental studies show that cyclic feeding leads to a higher time average performance (Schlatter *et al.*, 1983; Taylor and Sinkevitch, 1983; Muraki *et al.*, 1985). In general this is caused by the non-linear behaviour of the occurring reactions (Matros, 1989). To show the effects of the perturbations on the reactor performance, calculations with oscillating feeds have been performed for different temperatures, frequencies, and feed composition. The results are presented as a conversion improvement which can be either positive or negative and is defined by the difference of the time-average conversion during cyclic feeding and the steady state conversion.

#### Effects as a function of the temperature and the frequency

In Figures 6.10 to 6.13 the conversion improvements are shown as a function of the temperature at five frequencies. The conversion improvement for CO increases initially with increasing temperature. Above 480 K the improvement decreases and becomes negative, whereas at a temperature of 490 K the time-average conversion equals the steady state value. Higher frequencies lead to lower time-average conversions for all temperatures.

Cycling of the inlet concentrations is not beneficial for the NO conversion, as shown in Figure 6.11. Above 480 K the time-average conversions are lower than the steady state ones for all frequencies.

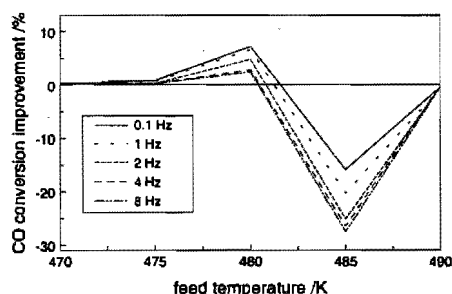


**Figure 6.10**  
Time-average CO conversion improvement due to cycling of the inlet concentrations versus feed temperature. Conditions  $\lambda = 1$ , Tables 6.3 and 6.4.

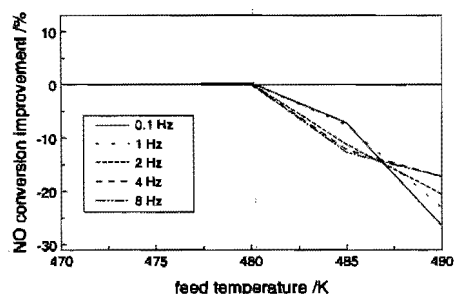


**Figure 6.11**  
Time-average NO conversion improvement due to cycling of the inlet concentrations versus feed temperature. Conditions  $\lambda = 1$ , Tables 6.3 and 6.4.

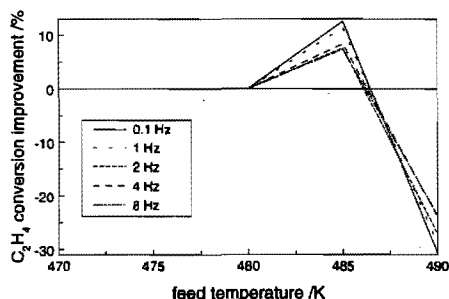


**Figure 6.12**

**Time-average  $C_2H_4$  conversion improvement due to cycling of the inlet concentrations versus feed temperature. Conditions  $\lambda = 1$ , Tables 6.3 and 6.4.**

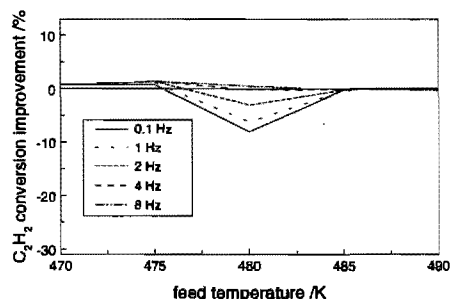


**Figure 6.13**

**Time-average  $C_2H_2$  conversion improvement due to cycling of the inlet concentrations versus feed temperature. Conditions  $\lambda = 1$ , Tables 6.3 and 6.4.**

The behaviour of the time-average  $C_2H_4$  conversion as a function of the temperature, see Figure 6.12, is similar to that of CO, but shifted towards higher temperatures. The improvement initially increases but becomes negative at an elevated temperature. The effects of the frequency are less pronounced than for CO, since higher frequencies lead to less improvement but also to less deterioration of the time-average conversion.

At low temperatures the time-average  $C_2H_2$  conversion is slightly higher than the steady state conversion, Figure 6.13. Higher temperatures lead initially to lower conversions but at an elevated temperature the steady state value is reached. Higher frequencies diminish the effects of the oscillations, leading to steady state conversions.

From Figures 6.10 to 6.13 it can be concluded that except for NO, cyclic feeding is beneficial at a temperature below the light-off of the individual components and that the cycling frequency should be relatively low. At low temperatures the strong inhibition of CO and  $C_2H_2$  leads to small amplitudes of the surface coverage resulting in steady state conversions. At high temperatures cycling effects become negative as a periodic shortage of either oxidants or reductants will

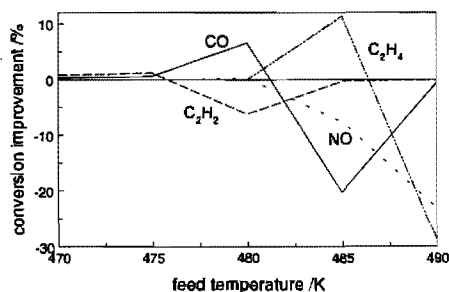


**Figure 6.14**

**Time-average conversion improvements due to 1 Hz cycling versus feed temperature. Conditions:  $\lambda = 1$ , Tables 6.3 and 6.4.**

arise. At elevated temperatures the amplitudes of CO and  $C_2H_2$  become zero, leading to complete conversions the whole period. As shown in Figure 6.4 the catalyst surface becomes covered with oxygen when almost all pollutants are converted. At elevated temperatures high conversions take place in the most front part of the reactor and therefore the last part of the becomes available for the storage of oxygen. During the net oxidizing part of the oscillation the excess of  $O_2$  and NO in the feed is stored on the catalytic surface. The oxygen adatoms as a result of adsorption and NO dissociation react with CO and hydrocarbons during the net reducing part of period.

The effects as a function of the feed temperature are summarized for a typical frequency of 1 Hz in Figure 6.14. As mentioned before, cyclic feeding leads to higher time-average conversions compared to steady state operation until the light-off temperature of the individual reactants is reached. Since the light-off temperatures are different for the individual reactants, the beneficial effects do not coincide at any temperature, as depicted in Figure 6.14. The strict sequence in pollutant conversions, see Figure 6.2, causes improvements for components at a low conversion level and worse situations for the others.

### Effects as a function of the feed composition

For a feed temperature of 500 K Figures 6.15 to 6.17 show the effect of the air/fuel ratio on the performance of the reactor during both steady state and cyclic feeding. The simulation results shown in these figures are in qualitative agreement with experimental results from the literature (Schlatter *et al.*, 1983; Taylor and Sinkevitch, 1983; Muraki *et al.*, 1985). As depicted in Figure 6.15, full conversion of all pollutants takes place at a stoichiometric feed only (equivalence ratio  $\lambda = 1$ ). At values of  $\lambda$  above unity, *i.e.* net oxidizing conditions, the NO conversion is reduced tremendously. Ethene oxidation is also slightly reduced since ethene adsorption has to compete with oxygen for the vacant sites. Under net reducing conditions ethene is not converted since it is a much weaker competitor for oxidizing species than ethyne and CO. Under deeper net reducing conditions NO reduction is decreased since its adsorption is inhibited by adsorbed CO and adsorbed nitrogen

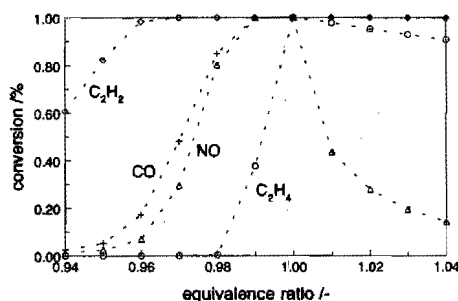


**Figure 6.15**  
**Effects of air-to-fuel ratio on the steady state average conversions. =  $C_2H_4$ ; + = CO;  $\diamond$  =  $C_2H_2$ ;  $\Delta$  = NO.**  
Conditions:  $T_f = 500$  K, Tables 6.3 and 6.4.

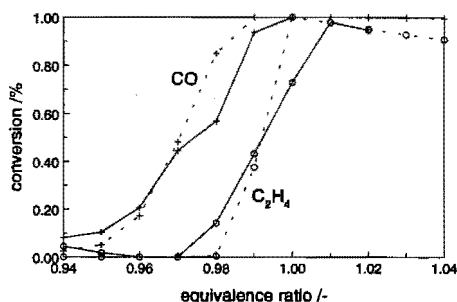


**Figure 6.16**

**Effects of air-to-fuel ratio on both the steady state and time average conversions. Full lines: cyclic feeding; dotted line: steady state.  $\diamond = \text{C}_2\text{H}_2$ ;  $+$  = CO. Conditions:  $T_1 = 500 \text{ K}$ ,  $f = 1 \text{ Hz}$ , Tables 6.3 and 6.4.**

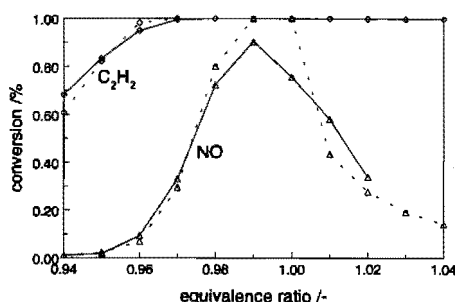


**Figure 6.17**

**Effects of air-to-fuel ratio on both the steady state and time average conversions. Full lines: cyclic feeding; dotted line: steady state.  $\diamond = \text{C}_2\text{H}_2$ ;  $\Delta = \text{NO}$ . Conditions:  $T_1 = 500 \text{ K}$ ,  $f = 1 \text{ Hz}$ , Tables 6.3 and 6.4.**

From Figures 6.16 and 6.17 it is clear that cyclic feeding is only beneficial at non-stoichiometric feeds where steady state conversions are far from complete. For a net reducing feed, time-average ethene conversion is higher than the steady state conversion. Under deeper net reducing conditions cyclic feeding is beneficial for CO and ethyne. Under a net oxidizing feed composition time-average NO conversion is higher than the steady state one. Hence, at a feed temperature of 500 K steady state operation is preferable and the so-called  $\lambda$ -window should be as narrow as possible to obtain high conversions of all pollutants.

## 6.5 Conclusions

A dynamic model based on first principles is used to predict the behaviour of an exhaust gas converter as a function of the process conditions. The simulation results are in qualitative agreement with the experimental results from the literature and the experiments described in Chapter 4 of this thesis. The model of the converter can therefore be used in the optimisation of the reactor performance.

Steady state simulations show that first ethyne is converted, then carbon monoxide, and finally nitrogen oxides and ethene simultaneously. Cycling feeding can either improve or deteriorate the performance of the converter and the effects are strongly influenced by the process conditions, such as feed temperature and composition, and the frequency. Below the light-off temperature the conversion improvement of CO, C<sub>2</sub>H<sub>4</sub> and C<sub>2</sub>H<sub>2</sub> increases with increasing temperature. Above the

light-off temperature time-average conversions become lower than the steady state ones. Steady state reactor operation at the stoichiometric point leads then to the highest performance.

Light-off calculations show that it takes more than 100 seconds to warm-up the reactor completely, but after 50 seconds conversion of all components is completed. During the warming-up of the reactor axial heat conductivity of the solid plays no role.

## References

- Cybulski, A., and Moulijn, J.A., Monoliths in Heterogeneous Catalysis. *Catal. Rev. -Sci. Eng.*, **36(2)**, 179-270, 1994
- Eigenberger, G., und Nieken, U., Katalytische Abluftreinigung: Verfahrenstechnische Aufgaben und neue Lösungen. *Chem.-Ing.-Tech.* **63(8)**, 781-791, 1991
- Engel, T., Ertl G., Elementary steps in the catalytic oxidation of carbon monoxide on platinum metals, *Adv. Catal.* **28**, 1-78, 1979
- Groppi, G., Belloli, A., Tronconi, E., Forzatti, P., A Comparison of Lumped and Distributed Models of Monolith Catalytic Combustors. *Chem. Eng. Sci.* **17**, 2705, 1995
- Hayes, R.E., and Kolaczkowski, S.T., Mass and Heat Transfer Effects in Catalytic Monolith Reactors. *Chem. Eng. Sci.* **49**, 3587-3599, 1994
- Heck, R.H., Wei, J. and Katzer, J.R., Mathematical Modeling of Monolithic Catalysts. *AIChE J.* **22(3)**, 477-484, 1976
- Impens, R., Automotive Traffic: Risks for the Environment. In: *Catalysis and Automotive Pollution Control I*, A. Frennet and J.-M. Bastin (Eds.). Elsevier Science Publishers B.V., Amsterdam, 11-30, 1987
- Leclerc, J.P., and Schweich, D., Modeling Catalytic Monoliths for Automobile Emission Control. *Lasa, H.I. de, et al. (Eds.), Chemical Reactor for Environmentally Safe Reactors and Products*, Kluwer Academic Publishers, 547-576, 1993
- Leighton, D.T., and Chang, H.C., A Theory for Fast-Igniting Catalytic Converters. *AIChE J.* **41(8)**, 1898-1914, 1995
- Lie, A.B.K., Modelling van een monolietreactor toegepast als autouitlaatgas-katalysator. *Graduation Report*, Institute for Continuing Education, Eindhoven University of Technology, 1992
- Lie, A.B.K., Hoebink, J.H.B.J and Marin, G.B., The Effects of Oscillatory Feeding of CO and O<sub>2</sub> on the Performance of a Monolithic Catalytic Converter of Automobile Exhaust Gas: A Modelling Study. *Chem. Eng. J.* **53**, 47-54, 1993
- Mabilon, G., Durand, D. and Courty, Ph., Inhibition of Post-Combustion Catalysts by Alkynes: A Clue for Understanding their Behaviour under Real Exhaust Conditions. In: *Catalysis and Automotive Pollution Control III* **96** (Studies in

- Surface Science and Catalysis*), A. Frennet and J.-M. Bastin (Eds.). Elsevier Science Publishers B.V., Amsterdam, 775-788, 1995
- Matros, Y.S., Catalytic processes under unsteady-state conditions, *Studies in surface science and catalysis*, **43**, Elsevier, Amsterdam, 1989
  - Madsen, N.K., and Sincovec, R.F., PDECOL, General Collocation Software for Partial Differential Equations [D3]. *ACM Trans. Math. Softw.* **5(3)**, 326-351, 1979
  - Muraki, H., Shinjoh, H., Sobukawa, H., Yokota, K. and Fujitani, Y., Behavior of automotive noble metal catalysts in cycled feedstreams, *Ind. Eng. Chem. Prod. Res. Dev.* **24**, 43-49, 1985
  - Nievergeld, A.J.L., Simulation and design of a catalytic monolith reactor for automobile exhaust gas conversion. *Graduation Report*, Institute for Continuing Education, Eindhoven University of Technology, 1994
  - Nievergeld, A.J.L., Hoebink, J.H.B.J and Marin, G.B., The performance of a monolithic catalytic converter of automobile exhaust gas with oscillatory feeding of CO, NO and O<sub>2</sub>: a modelling study, *Studies in Surface Science and Catalysis* **96**, 909 - 918, 1995
  - Oh, S.H., Fisher, G.B., Carpenter, J.E. and Goodman, D.W., Comparative Kinetic Studies of CO-O<sub>2</sub> and CO-NO Reactions over Single Crystal and Supported Rhodium Catalysts. *J. Catal.* **100**, 360-376, 1986
  - Palmer, R.L., Chemical Reactions on Solid Surfaces Using Molecular Beam Techniques. *US NTIS AD Report*, A040579, 1977
  - Pattas, K.N., Stamatelos, A.M., Pistikopoulos, P.K., Koltsakis, G.C., Konstandinidis, P.A., Volpi, E. and Leveroni, E., Transient Modeling of 3-Way Catalytic Converters. *SAE Paper* 940934, 1994
  - Reid, R.C., Polling, J.M. and Prausnitz, The Properties of Gases and Liquids. *McGraw-Hill*, New York, 587, 1987
  - Sant, R., Kaul, D.J. and Wolf, E.E., Transient Studies and Kinetic Modeling of Ethylene Oxidation on Pt/SiO<sub>2</sub>. *AIChE J.* **35(2)** 267-278, 1989
  - Schlatter, J.C., Laboratory Reactor Systems for Three-Way Automotive Catalyst Evaluation. *Ind. Eng. Chem. Prod. Dev.* **22(1)**, 51-56, 1983
  - v. Selow, E.R., Graduate Report, Design of a monolithic reactor for automobile exhaust gas conversion with improved light-off behaviour, Institute for Continuing Education, Eindhoven University of Technology, 63-65, 1996
  - Siemund, S., Schweich, D., Leclerc, J.P. and Villermaux, J., Modelling Three-Way Monolithic Catalytic Converter: Comparison between Simulation and Experimental Data. In: *Catalysis and Automotive Pollution Control III* **96** (*Studies in Surface Science and Catalysis*), A. Frennet and J.-M. Bastin (Eds.). Elsevier Science Publishers B.V., Amsterdam, 887-896, 1995
  - Taylor, G.I., Dispersion of soluble matter in solvent flowing through a tube, *Proc. Roy. Soc.* **A219**, 186, 1953

- Taylor, K.C., and Sinkevitch, R.M., Behaviour of Automobile Exhaust Catalysts with Cycled Feedstreams. *Ind. Eng. Chem. Prod. Res. Dev.* **22**, 45-51, 1983
- Villermaux, J., and Schweich, D., Is the Catalytic Monolith Reactor Well Suited to Environmentally Benign Processing? *Ind. Eng. Chem. Res.* **33**, 3025-3030, 1994
- Zygourakis, K. Transient Operation of Monolith Catalytic Converters: A Two-Dimensional Reactor Model and the Effects of Radially Nonuniform Flow Distributions. *Chem. Eng. Sci.* **44(9)**, 2075-2086, 1989



## APPENDIX 6A

### Calculation of Physical Coefficients

In modelling the converter, radial concentration, temperature and velocity profiles in the channels were approximated by the application of the asymptotic Sherwood and Nusselt number. For fully developed laminar flows in long cylindrical channels, two limit cases for the asymptotic Nusselt number  $Nu_w$  for heat transfer are known:  $Nu_w = 4.36$  if the wall heat flux is constant, and  $Nu_T = 3.66$  if the wall temperature is constant. The Nusselt number for fully developed flow with constant wall temperature is used in this work; the asymptotic Sherwood number for mass transfer follows from the Reynolds analogy  $Sh = Nu$ . For significantly long monolith segments, working with asymptotic values for Nusselt and Sherwood is adequate (Heck *et al.*, 1976; Groppi *et al.*, 1995; Siemund *et al.*, 1995).

The binary diffusion coefficient of component A in component B is calculated by application of the method of Füller-Schettler-Giddings (Reid *et al.*, 1987):

$$D_{AB} = \frac{3.16 \cdot 10^{-8} T^{1.75}}{P_{tot} (v_A^{1/3} + v_B^{1/3})^2} \left( \frac{1}{M_A} + \frac{1}{M_B} \right)^{1/2} \quad (6A.1)$$

where  $v$  is the diffusion volume in  $m^3 \text{ mol}^{-1}$ , as given in Table 6A.1. The coefficients are calculated for diffusion in nitrogen (component B in Equation 6A.1), *i.e.* there is no correction made for multi component diffusion.

**Table 6A.1.**  
Diffusion volumes in  $m^3 \text{ mol}^{-1}$  of some gases  
(Reid *et al.*, 1987).

$N_2$	$18.5 \cdot 10^{-6}$
CO	$18.0 \cdot 10^{-6}$
$O_2$	$16.3 \cdot 10^{-6}$
NO	$10.7 \cdot 10^{-6}$
$C_2H_4$	$41.0 \cdot 10^{-6}$
$C_2H_2$	$36.4 \cdot 10^{-6}$

The mass transfer coefficient for reactant  $i$  ( $i = \text{CO}, \text{O}_2, \text{NO}, \text{C}_2\text{H}_4, \text{C}_2\text{H}_2$ ) is given by:

$$k_{t,i} = \frac{\text{Sh}_\infty D_i}{d_b} \quad (6A.2)$$

Thermal conductivity of bulk gas phase is approximated by that of  $\text{N}_2$  and given by (Lie, 1992):

$$\lambda_t = 3.912 \cdot 10^{-4} + 9.798 \cdot 10^{-5} T_{\text{avg}} - 5.06 \cdot 10^{-8} T_{\text{avg}}^2 + 1.501 \cdot 10^{-11} T_{\text{avg}}^3 \quad [\text{W m}^{-1} \text{K}^{-1}] \quad (6A.3)$$

As the Lewis number is close to 1 for all reactants, film thicknesses for heat and mass transfer are practically identical. The average temperature in the film is defined by:

$$T_{\text{avg}} = \frac{T_f + T_s}{2} \quad (6A.4)$$

The heat transfer coefficient follows from:

$$\alpha = \frac{\text{Nu}_\infty \lambda_t}{d_b} \quad (6A.5)$$

where  $\text{Nu}_\infty = 3.66$ .

The specific heat of the bulk gas phase is given by (Lie, 1992):

$$c_{pf} = 1.055 \cdot 10^3 + 0.197 T_f + 4.94 \cdot 10^{-4} T_f^2 - 1.88 \cdot 10^{-7} T_f^3 \quad [\text{J kg}^{-1} \text{K}^{-1}] \quad (6A.6)$$

and of the solid phase (Oh and Cavendish, 1982):

$$c_{ps} = 1.071 \cdot 10^3 + 0.156 T_s - 3.435 \cdot 10^{-7} T_s^2 \quad [\text{J kg}^{-1} \text{K}^{-1}] \quad (6A.7)$$

# 7

---

## MODEL PREDICTIVE CONTROL OF THE AUTOMOTIVE EXHAUST GAS CONVERTER

### 7.1. Introduction

Nowadays, almost every new car sold in Europe is equipped with a catalytic converter in combination with a fuel control system to reduce the pollutants in the exhaust of gasoline engines. The applied converter enables the removal of CO, NO and hydrocarbons. To let these three reactions proceed simultaneously the exhaust gas composition is kept close to the stoichiometric point by a fuel control system which controls the air-to-fuel ratio fed to the engine. As the delay time in the feedback loop of the system prevents the control algorithm of maintaining a stoichiometric exhaust gas composition under all operating conditions, the gas composition oscillates with a frequency typically between 0.5 and 10 Hz around the stoichiometric composition. These oscillations may lead to higher time-average conversions as demonstrated in Chapter 6. However, to exploit the oscillatory effects on the performance of the converter fully, the frequency and the amplitude have to be set to their corresponding optimal values. To maintain the optimum frequency and amplitude under all conditions a robust and stable control system is required to control the air-to-fuel ratio. The currently applied control system cannot fulfill these demands as the oscillations are determined by the process conditions, *e.g.* the engine speed. Therefore, it may be beneficial to replace the applied control system by a so-called Model Predictive Controller which can cope far better with delay times than a traditional feedback controller.

Furthermore, novel catalyst technologies require more sophisticated control

algorithms. Several studies were performed to explore the use of Pd as a possible replacement for Rh. Palladium features both better light-off performance (Beck and Sommers, 1994) and better thermal stability as compared to Pt and Rh, but only in combination with very tight air-to-fuel control (Taylor, 1994). As several other new developments focus on externally heated converters (Oh *et al.*, 1993) the temperature of the converters must be controlled carefully to ensure a long durability since overheating may lead to fast degeneration of the catalyst.

This chapter demonstrates the use of a Model Predictive Control scheme in the strategy towards Ultra Low Emission Vehicles. The controller is based on the model of the catalytic converter, discussed in Chapter 6, and a simple model of the gasoline engine. In section 7.2 some aspects of model predictive control will be addressed first. The performance of the model predictive controller will be compared with the performance of a conventional controller.

## 7.2 Model predictive control

In this section some aspects of Model Predictive Control (MPC) will be discussed briefly. For a more detailed description see Richalet *et al.* (1978), Garcia *et al.* (1989), Muske and Rawlings (1993) and Richalet (1993). To show the difference between a MPC and a conventional controller the latter will be discussed first. A basic representation of a conventional closed loop control system is given in Figure 7.1. The controlled process can be either a so-called SISO system, *i.e.* a system with only one input and one output or a MIMO system with multiple inputs and multiple outputs. Often not all inputs and outputs of a MIMO system are used in the controller. The controlled process outputs are called the controlled variables (CV's), while the inputs the controller adapts to keep the CV's at their setpoints are called the manipulated variables (MV's). The control objective is to keep the controlled variables at the setpoints in the presence of disturbances. To accomplish this, the controlled variables are subtracted from the corresponding setpoints and the errors are supplied to the controller which adapts the manipulated variables of the process in a way that reduces the deviation from the setpoints.

In Figure 7.2 the model predictive control diagram is shown. The so-called feed forward part of this controller consists of a model of the process which is used to predict the values of the controlled variables, while the feedback loop compensates for model errors and disturbances entering the process. The controlled variables are now compared with the model output and the error is fed to the controller. The controller uses the deviation between the model and the process in combination with the setpoints to calculate the new values of the manipulated variables. This in contrast to a conventional controller which determines the values of the manipulated variables

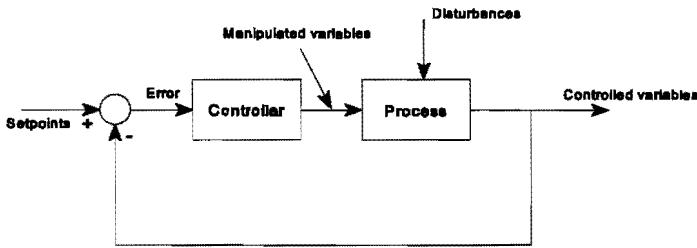


**Figure 7.1**  
**Basic block diagram of a closed loop system.**

using the deviation between the setpoints and the controlled variables. In steady state the controlled variables have obtained the same values as the setpoints due to the integrating behaviour of the MPC. This also means that the model outputs equal the setpoints which is only the case if the controller behaviour equals the inverse steady state model behaviour.

The control algorithm calculates the moves  $\Delta u$  of the manipulated variables implemented to reach the setpoints by minimizing the objective function given by:

$$\min_{\Delta u(k) \dots \Delta u(k+m-1)} \sum_{l=1}^p (w_{y,l} (y_m(k+l) - y(k)))^2 + \sum_{l=1}^m w_{u,l} \Delta u(k+l-1)^2 \quad (7.1)$$

subject to the constraints on manipulated and the controlled variables:

$$u_{\min} \leq u(\cdot) \leq u_{\max}, \quad |\Delta u(\cdot)| \leq \Delta u_{\max}, \quad y_{\min} \leq y(\cdot) \leq y_{\max} \quad (7.2)$$

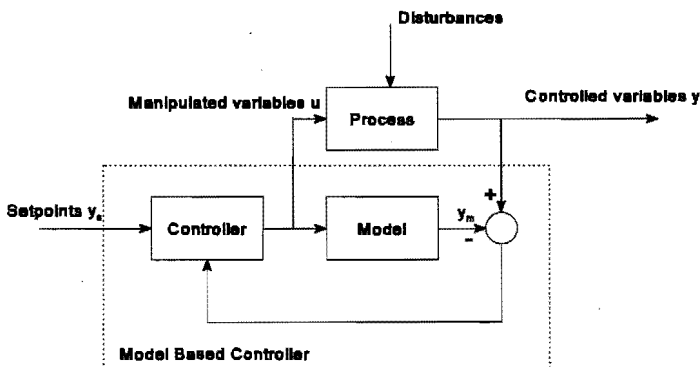


**Figure 7.2**  
**Basic block diagram for model predictive control.**

where  $y$  is the process output,  $y_m$  the model output,  $\Delta u$  the so-called control moves, the changes of manipulated variables,  $p$  the prediction horizon, *i.e.* the number of samples the model outputs are calculated, and  $m$  the number of next control moves the controller calculates to drive the CV's to the setpoints. The first term of Equation 7.1 represents the error between the model outputs and the process outputs at the current time, where  $w_{y,i}$  is the (time-dependent) weight penalizing the deviations from the CV's. The second term of Equations 7.1 represents the so-called costs related to the moves of the manipulated variables. Large values of  $w_{u,i}$  lead to smaller values of  $\Delta u$  and hence to a less aggressive control action. So, the algorithm of the controller minimizes the error between the model output and the process output over a horizon of  $p$  sampling times by calculating  $m$  control moves of the manipulated variables. Although  $m$  moves are calculated, only the first one is implemented. At the next sampling interval, new values of the measured outputs are obtained, the control horizon is shifted forward by one step, and the same computations are repeated. This control law is referred to as moving horizon. The actions implemented in the feed forward control algorithm in case of a SISO system are summarized in Figure 7.3. The controller tries to minimize the difference between the model output and the process output, see Figure 7.2, which is equivalent to minimizing the deviation from the setpoint.

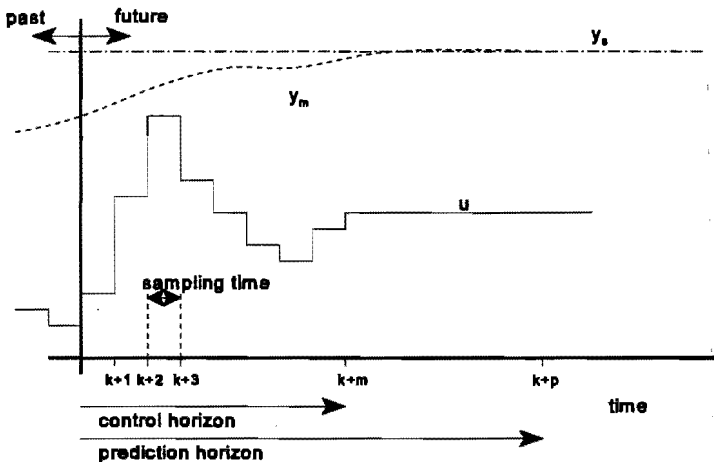


**Figure 7.3**  
**Model based predictive control law.**

Controller designs based on the MPC concept have found wide acceptance in industrial applications (Garcia *et al.*, 1989). Model based controllers have the advantage over conventional types of feedback controllers to cope with delay times and with

bounds on the manipulated variables reflecting real process constraints. A conventional controller will not detect a disturbance entering the process until after the delay time, and therefore the proper control action will be taken too late. For instance, in case of the exhaust gas converter the nowadays applied controller causes oscillatory behaviour as result of the relatively large delay time compared with the time scales of the process. Furthermore, the air-to-fuel ratio is constrained as the engine will not run properly when the deviation from the stoichiometric value of 14.6 becomes too large. As a classical feedback controller, see Figure 7.1, reacts only after it has detected a deviation from the setpoints, a model based control algorithm uses the information about the process dynamics to anticipate the effects of the disturbance on the output and to adjust the process inputs properly in order to keep the controlled variables at the setpoints.

Most often a model predictive controller uses a linear model to predict the values of controlled variables whereas the process itself may be nonlinear. Using a linear model to predict the responses of a nonlinear process is allowed assuming a small region of operating conditions around the steady state operation of interest. MPC algorithms have been successfully used to control chemical processes, which often exhibit both nonlinear steady state and dynamic behaviour (Richalet *et al.*, 1978; Richalet, 1993). In case of highly nonlinear process behaviour in the surroundings of the working point the process is approximated by a linear system, whereas the nonlinear behaviour is handled with (static) nonlinear transformations. When the assumption of linearity around the working point is allowed, the superposition principle can be applied. Hence, when the model describes the process response for a given input signal it can be used to predict the responses to other input signals as well. However, nowadays much effort has been put in studying usability of nonlinear models in MPC controllers.

MPC algorithms often use a so-called black box model to predict the responses of the process over a given time horizon. This black box model describes the input-output behaviour in a pure mathematical sense as the underlying equations are not based on physical laws. An advantage of a black box model is the easy-to-solve model equations. This is very important when dealing with real time control as the governing equations have to be solved within one fixed sample period. The black box model is obtained by an identification algorithm which adapts coefficients of the model in such a way to describe the process responses. The model identification is usually carried out perturbing the process. By monitoring the output responses after inducing changes to the inputs the relevant process dynamics, including the delay times when applicable, can be determined. As the control algorithm contains valuable information about the dynamics and the delay times of the process, a model based controller can respond in a more dedicated way to disturbances and is therefore more robust than a conventional controller. For more information about the identification see Backx (1987) and Ljung (1987).

### 7.3 Identification procedure

The process identification procedure used to develop the black box model of the model based controller can be divided into two parts, each with its own steps. Each step of the procedure is directed to obtain more detailed information about dynamic behaviour of the process in the surroundings of the working point of interest. The identification procedure consists of a preliminary study, followed by model estimation and validation (Backx, 1987; Backx and Damen, 1989). The subsequent steps will be discussed in more detail.

#### Preliminary study

A first step in the preliminary study is the selection of the appropriate manipulated and controlled variables. The economics of the process, environmental legislation and critical process operation conditions determine the controlled variables. Manipulated variables are selected according to their different effects on the controlled variables. When manipulation of an input does not lead to measurable process responses then this input is not considered in the identification procedure. Inputs that cannot be manipulated but influence the controlled variables are called disturbance or feed forward signals. Disturbance signals which are measurable can be included in the identification and used for feed forward disturbance compensation; unmeasurable disturbance signals are compensated for by the feedback control.

Since the identification procedure is based on modelling the dynamic behaviour of the process with linear dynamic models, an important step of the preliminary study is the test if the amplitude ranges applied to the inputs are allowable without violating the assumption of linearity around the operating conditions of interest. To test the steady state linearity of the process in the surroundings of the working point, a staircase signal is applied to each input separately, see Figure 7.4. The time between the steps is chosen according to the characteristic response time, which is related to the largest time constant of the process. For the analysis of the steady state linearity the process must reach a steady state for each step applied. As the separate steps have the same amplitude, the responses to the steps will have the same amplitude in case of a linear process. When the amplitudes of the responses to each step differ significantly, *i.e.* the process shows nonlinear steady state behaviour, a nonlinear transformation can be applied to the output of the linear model. The applied transformation approximates the steady state behaviour of the process, and the overall behaviour of the model will resemble the nonlinear process behaviour. More properties about the use of these transformations will be discussed in section 7.5.2. Furthermore, the responses of the process to the staircase signal enable an estimate of the characteristic response time,



which is required to define the duration of the input signals used in the next test step, and in the final estimation of the model parameters.

For the detection of dynamic nonlinearities and an impression of the bandwidth of the process, *i.e.* the smallest time constant of the process, a random input signal (noise) is often applied. In order to be able to determine the bandwidth of the process the input signal must cover a broad frequency spectrum, *i.e.* starting at the reciprocal of characteristic response time determined from the staircase experiments up to the reciprocal of the smallest time scale to be expected, to force the process to

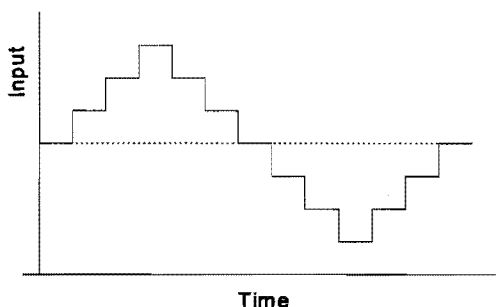


**Figure 7.4**  
***Staircase input signal applied for steady state linearity analysis of a process.***

enter the sliding regime. Significant changes in the cross-correlations functions of the input signal and the corresponding responses indicate dynamic nonlinearities.

### Model estimation and validation

In the preliminary study the bandwidth and the region of linear process behaviour have been determined. Based on this information the input signals for the final parameter estimation can be constructed. The frequency range of the input signals must again cover the bandwidth of the process to obtain a model which describes the dynamic behaviour completely, whereas the amplitudes for each input must be in the estimated range of linearity, if necessary extended by the application of linearizing functions. The model parameters are estimated by means of nonlinear regression of the model equations with measured responses. For the validation of the model the responses to input signals not used in the regression are calculated and compared with the recorded real process responses.

## **7.4 Description of the process**

The process to be controlled consists of a gasoline engine in combination with the exhaust gas converter. The model of the converter, discussed in Chapter 6 is used to simulate the behaviour of a real converter, while the model of the engine is constructed from literature data (Taylor and Sinkevitch, 1983). The  $C_2H_4$  and  $C_2H_2$

concentrations of the model are calculated by dividing the reported total hydrocarbon concentration by two. For sake of simplicity it is assumed that the exhaust gas composition changes instantaneously as a result of adaptations of the equivalence ratio  $\lambda$ , meaning that a steady state model of the engine can be applied. The engine outlet concentrations as a function of  $\lambda$  are depicted in Figure 7.5.

In Figure 7.6 the complete process is shown. The delay time  $\Delta t$  accounts for the residence time of the exhaust gas in the tailpipe between the exhaust manifold and the converter and for the residence time of the air-fuel mixture in the inlet manifold of the engine. The exhaust gas mass flow rate and the converter feed temperature are considered as feed forward signals, meaning that they have known values and influence the outlet concentrations. The former is assumed to be constant meaning that the variations of the engine revolutions per second are very small compared with the mean engine speed; the latter will be included in the identification process so the effects of the feed temperature on the outlet concentrations will be accounted for.

Before the identification is carried out the controlled variables, the feed forward variables and the manipulated variables have to be determined. As mentioned before  $T_i$  will be regarded as a feed forward signal. This means that there is only one degree of freedom left and hence only one outlet concentration can be controlled. The  $\lambda$ -sensor of the currently applied control system in cars measures the oxygen concentration upstream of the converter and the signal of this sensor is used as a controlled variable; the composition of the air-fuel mixture fed to the engine is the manipulated variable. In line with this system, the air-to-

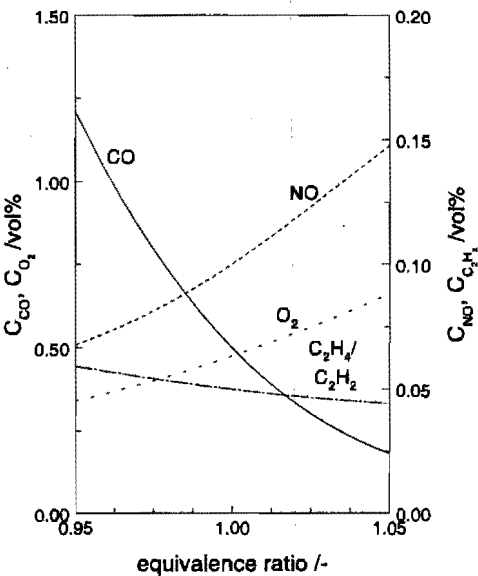


**Figure 7.5**  
*Engine outlet concentrations versus equivalence ratio  $\lambda$ .*

**Table 7.1**  
*Process parameters and range of input variables.*

G	/kg s <sup>-1</sup>	0.01
$\Delta t$	/s	0.1
$\lambda$	/-	0.95..1.05
$T_i$	/K	400..510

fuel ratio given by  $\lambda$  is used as manipulated variable in the MPC design. In contrast to the real system it is assumed that the oxygen concentration downstream of the converter is measured and this value will be used as controlled variable. This enables the optimisation of the reactor performance as a function of the air-to-fuel ratio. Hence, the control system adapts  $\lambda$  so the oxygen outlet concentration is close to the desired value, the setpoint. The parameters of the process and the range of the inputs are given in Table 7.1. Both the mass flow  $G$  and the delay time  $\Delta t$  are set to values typical for normal engine operation. The feed temperature covers the temperature range from cold-start behaviour to a fully warmed-up converter, whereas  $\lambda$  is in the range of allowed values for proper operation of the engine.

The models derived from the identification process will be used as the controlled process instead of the rigorous converter model discussed in Chapter 6 as the computational time decreases substantially. This is allowed since the purpose of this chapter is to demonstrate the advantages of a model based controller compared with a conventional controller.

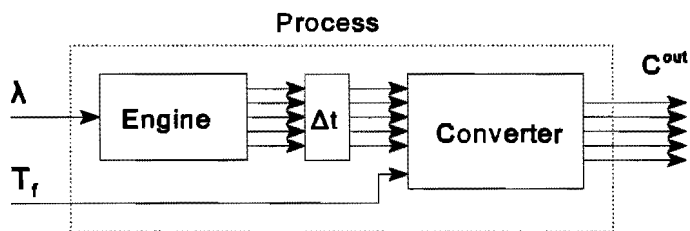


**Figure 7.6**

**Schematic drawing of the process.**  $C^{out} = CO, O_2, NO, C_2H_4$  and  $C_2H_2$ .

## 7.5 Identification results

### 7.5.1 Preliminary analysis

The outlet concentrations at three feed temperatures and the staircase input signal  $\lambda$  are given in Figures 7.7 to 7.11. The duration of the steps is based on the characteristic times of the outlet concentrations as a result of step changes of  $\lambda$ . It should be noticed that due to the engine characteristics, see Figure 7.5, the concentrations of the reducing components at the inlet of the converter decrease with increasing  $\lambda$ , whereas the concentrations of oxidizing components increase with increasing  $\lambda$ . From the figures it is clear that the process exhibits nonlinear behaviour

under some operating conditions. At a feed temperature of 470 K the steady state input-output behaviour of all components is rather linear. It is reasonable to assume that

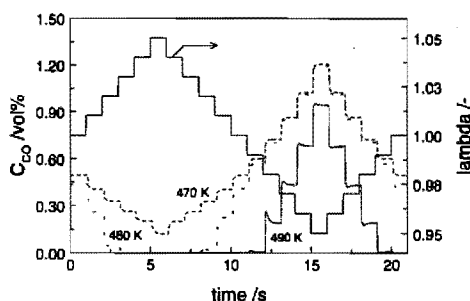


**Figure 7.7**

$\lambda$  and  $\text{CO}$  outlet concentration versus time at three feed temperatures. (—) =  $\lambda$ ; (---) = 470 K; (...) = 480 K; (-.-) = 490 K.

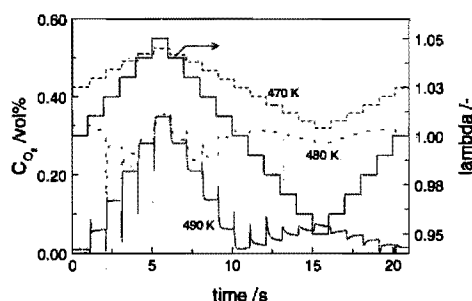


**Figure 7.8**

$\lambda$  and  $\text{O}_2$  outlet concentration versus time at three feed temperatures. (—) =  $\lambda$ ; (---) = 470 K; (...) = 480 K; (-.-) = 490 K.

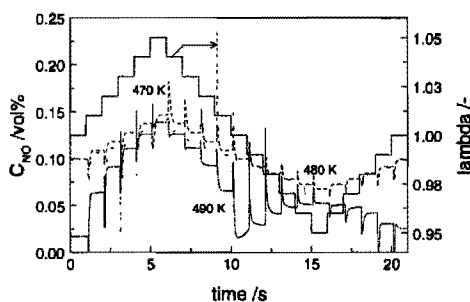


**Figure 7.9**

$\lambda$  and  $\text{NO}$  outlet concentration versus time at three feed temperatures. (—) =  $\lambda$ ; (---) = 470 K; (...) = 480 K; (-.-) = 490 K.

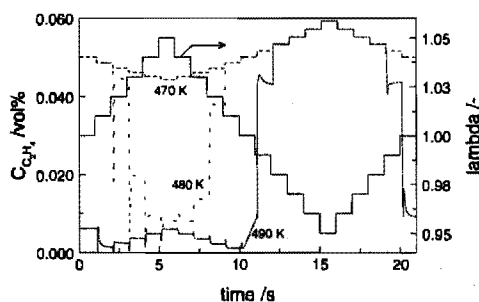


**Figure 7.10**

$\lambda$  and  $\text{C}_2\text{H}_4$  outlet concentration versus time at three feed temperatures. (—) =  $\lambda$ ; (---) = 470 K; (...) = 480 K; (-.-) = 490 K.

most of the nonlinear behaviour is caused by the kinetics of the occurring reactions. The reaction rates are relatively low at a temperature of 470 K and consequently there is little interaction between the gas phase and the catalyst surface. This means that the steady state input-output behaviour at low temperatures is mainly determined by the engine characteristics. At a higher temperature the process cannot be considered as linear around the stoichiometric value of  $\lambda$  ( $\lambda = 1$ ) since the reactions proceed at higher rates. The steady state behaviour is determined by the so-called gains only, see also

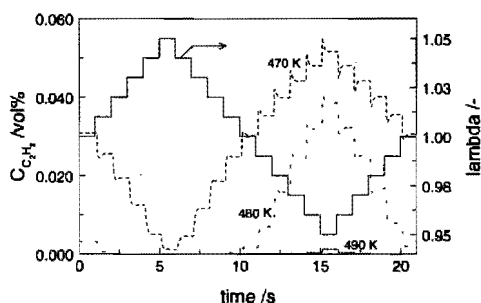


**Figure 7.11**

**$\lambda$  and  $C_{C_2H_2}$  outlet concentration versus time at three feed temperatures. (—) =  $\lambda$ ; (--) = 470 K; (...) = 480 K; (-.-) = 490 K.**

Chapter 3, which are given by the ratio of changes of an output to changes of an input in the surroundings of the working point. As the converter exhibits nonlinear behaviour the steady state gains are strongly dependent on the inputs as shown in the figures. For example, the steady state gains of CO and  $C_2H_2$  are always negative, but the steady state gains of  $C_2H_4$  are negative for temperatures up to 480 K and become positive at a feed temperature of 490 K and  $\lambda$  between 1.02 and 1.05. The NO outlet concentration at 490 K follows  $\lambda$  for  $\lambda > 1$ , but shows opposite behaviour for  $\lambda < 1$ . The sign of the steady state gains of  $O_2$  changes several times as a function of  $\lambda$  for temperatures

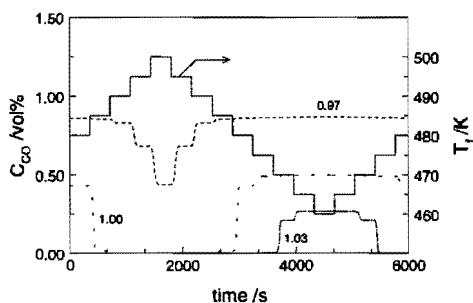


**Figure 7.12**

**Feed temperature and CO outlet concentration versus time at three values of  $\lambda$ . (—) =  $T_f$ ; (--) = 0.97; (...) = 1.00; (-.-) = 1.03.**

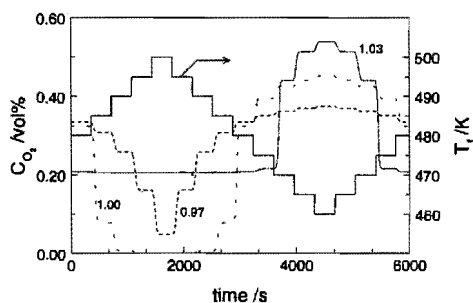


**Figure 7.13**

**Feed temperature and  $O_2$  outlet concentration versus time at three values of  $\lambda$ . (—) =  $T_f$ ; (--) = 0.97; (...) = 1.00; (-.-) = 1.03.**

above 470 K. This change of sign of the gains may lead to instabilities in combination with a feedback control system as the (stabilizing) negative feedback becomes a positive feedback when the sign of the gain changes as function of the operating conditions. In the design of the control system special attention has to be paid to avoid changes of sign in the feedback loop.

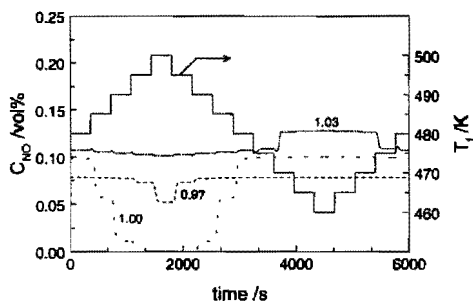


**Figure 7.14**

**Feed temperature and NO outlet concentration versus time at three values of  $\lambda$ . (—) =  $T_f$ ; (---) = 0.97; (...) = 1.00; (-.-) = 1.03.**

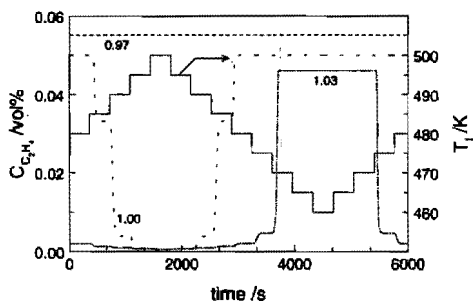


**Figure 7.15**

**Feed temperature and  $C_2H_4$  outlet concentration versus time at three values of  $\lambda$ . (—) =  $T_f$ ; (---) = 0.97; (...) = 1.00; (-.-) = 1.03.**

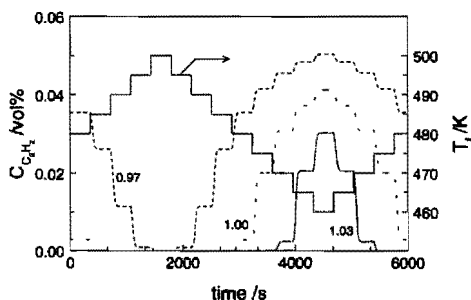


**Figure 7.16**

**Feed temperature and  $C_2H_2$  outlet concentration versus time at three values of  $\lambda$ . (—) =  $T_f$ ; (---) = 0.97; (...) = 1.00; (-.-) = 1.03.**

There are also dynamic nonlinearities present in the process as the characteristic response times depend on  $\lambda$  and  $T_i$ . At low temperatures, the dynamic behaviour of the process is mainly determined by the gas flow through the reactor. The absence of axial dispersion in the gas phase results in responses which have about the same shape as the input. They are only shifted in time due to the gas flow through the reactor. At higher temperatures the dynamic behaviour is mainly determined by the kinetics. However, the characteristic times of the outlet concentrations due to changes of  $\lambda$  are all of the order of magnitude of seconds.

The responses as a result of a staircase feed temperature at three values of  $\lambda$  are shown in Figures 7.12 to 7.16. The length of the step is of the same order as the characteristic response time. From these figures it is clear that the outlet concentrations have a nonlinear dependency on the feed temperature. The behaviour of all components is similar. Under net reducing conditions and sufficient high temperatures the oxidizing components are completely converted, whereas the reducing components are fully converted under net oxidizing conditions. The characteristic response time is of the order of magnitude of 100 s and is rather independent of the conditions and is mainly determined by the heat capacity of the converter and the heat transfer resistance located between the bulk gas phase and the solid phase. As the operating conditions of interest cover the range from a cold-start to a fully warmed-up converter, it is clear that the process cannot be considered as linear. Therefore, nonlinear transformations have to be applied to the outputs in order to use linear models in the controller.

### 7.5.2 Nonlinear transformations

The purpose of this chapter is to show the design and the performance of a MPC based on a linear internal model. However, in section 7.5.1 it has been shown that the process cannot be considered as linear over the interesting range of input values. Furthermore, the change of sign of the steady state gains may lead to instabilities of the controlled process if not compensated for properly. To allow the use of a dynamic linear model in the controller a nonlinear transformation has to be applied to the oxygen outlet concentration of the converter. The transformed output will depend linearly on the manipulated variable and is used as controlled variable instead of the oxygen output concentration. The inverse of the steady state process behaviour is used to

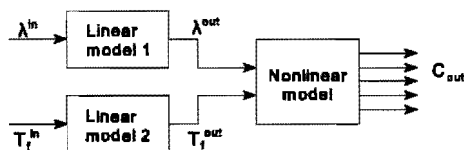


**Figure 7.17**  
Block diagram of the process. Linear model 1 and 2 will be obtained by the identification analysis.

calculate the controlled variable dependence on the manipulated variable  $\lambda$ . The feed temperature dependency of the oxygen concentration is also linearized as  $T_f$  is used as feed forward in the controller and therefore this behaviour has to be accounted for. The input-output behaviour of the dynamic linear models in combination with the nonlinear transformation approximate then the nonlinear behaviour of the process, see Figure 7.17. First the steady state behaviour is determined by solving the equations of the converter in combination with the engine over the range of operating conditions. This data will be used to derive a set of equations which describe the steady state behaviour of all outlet concentrations, since this model will be used to calculate the optimal values of  $\lambda$  as a function of the temperature, see section 7.7.

The steady state behaviour of the process is determined by calculating the outlet concentrations of the converter as a function of the feed temperature  $T_f$  and the equivalence ratio  $\lambda$ . Equations 7.3 to 7.8 show the equations used to describe the steady state behaviour of the process. In Figures 7.18 to 7.22 the steady state outlet concentrations and outlet concentrations calculated using these equations as a function of  $T_f$  and  $\lambda$  are depicted. The first step in developing the transformations was the selection of the base function. Since the outlet concentrations are saturated for both low and high temperatures a tangent hyperbolic function is most suited to describe the steady state outlet concentrations. This function is shifted to positive values for the range of temperatures of interest by the introduction of  $T_0$ , being a function of both  $T_f$  and  $\lambda$ , and of  $C_i^l$  and  $C_i^h$ , being the concentrations of component  $i$  at 400 and 510 K respectively. The  $\lambda$  dependence of both  $C_i^l$  and  $C_i^h$  cannot be described by a simple function and is accounted for by interpolation of the values of  $\lambda$  given in Figures 7.18 to 7.22 using splines as base functions. The exponential function in the argument of the tanh accounts for the asymmetric steady behaviour of the outlet concentrations around  $T_0$ , whereas parameter  $p$  determines whether the steepest descent is located at temperatures below  $T_0$  ( $p=-1$ ) or above  $T_0$  ( $p=1$ ).  $b_1$  and  $b_2$  are  $\lambda$  dependent tuning parameters.

The outlet concentration  $i$  ( $i = \text{CO}$ ,  $\text{O}_2$ , and  $\text{C}_2\text{H}_2$  ( $p=1$ ), and  $\text{NO}$  and  $\text{C}_2\text{H}_4$  ( $p=-1$ )) is calculated using Equation 7.3, given by:

$$C_i = C_i^l + \frac{C_i^h - C_i^l}{2} \left( 1 + p \tanh \left( -b_1 (e^{-b_2 T_0} - T_0) \right) \right) \quad (7.3)$$

where  $C_i^l$  is the outlet concentration of component  $i$  at  $T_f = 400$  K and  $C_i^h$  the outlet concentration at  $T_f = 510$  K. As mentioned before, both  $C_i^l$  and  $C_i^h$  are a function of  $\lambda$ . Values of these parameters at intermediate values of  $\lambda$  are determined by interpolation with splines as base functions.  $T_0$  is given by:



$$T_0 = p \frac{\beta_1 + \beta_2 \lambda + \beta_3 \lambda^2 - T_i}{\beta_1 + \beta_2 \lambda + \beta_3 \lambda^2 - T_i} \quad (7.4)$$

where  $T_i = 400$  K. For  $i = \text{CO}$ ,  $\text{O}_2$ ,  $\text{C}_2\text{H}_4$  and  $\text{C}_2\text{H}_2$   $b_1$  and  $b_2$  are given by:

$$b_1 = \beta_4 + \beta_5 \lambda \quad (7.5)$$

$$b_2 = \beta_6 + \beta_7 \lambda \quad (7.6)$$

The  $\lambda$  dependence of both  $b_1$  and  $b_2$  for  $i = \text{NO}$  cannot be described by a linear function, and is therefore given by:

$$b_1 = \beta_4 + \beta_5 \lambda + \beta_6 \lambda^2 \quad (7.7)$$

$$b_2 = 9.27 \cdot 10^{-29} e^{\beta_7 \lambda} \quad (7.8)$$

The parameters  $\beta_i$ , given in table 7.2, are obtained by nonlinear regression of the steady state outlet concentrations of the process with Equations 7.3 to 7.8. In Figures 7.18 to 7.22 the outlet concentrations as a function of the inputs  $\lambda$  and  $T_i$  and the calculated concentrations using Equations 7.3 to 7.8 are shown and it can be concluded that the steady state process behaviour is described adequately by the model.

**Table 7.2**

**Parameters of the nonlinear transformations obtained by regression of the outlet concentrations with Equations 7.3 to 7.8. Conditions see Table 7.1.**

		CO	O <sub>2</sub>	NO	C <sub>2</sub> H <sub>4</sub>	C <sub>2</sub> H <sub>2</sub>
$\beta_1$	/-	5.5 10 <sup>3</sup>	3.1 10 <sup>3</sup>	-3.9 10 <sup>3</sup>	3.5 10 <sup>3</sup>	2.7 10 <sup>3</sup>
$\beta_2$	/-	-9.2 10 <sup>3</sup>	-4.8 10 <sup>3</sup>	8.9 10 <sup>3</sup>	-5.6 10 <sup>3</sup>	-4.0 10 <sup>3</sup>
$\beta_3$	/-	4.2 10 <sup>3</sup>	2.1 10 <sup>3</sup>	-4.5 10 <sup>3</sup>	2.6 10 <sup>3</sup>	1.8 10 <sup>3</sup>
$\beta_4$	/-	-1.3 10 <sup>2</sup>	-14.1	-1.3 10 <sup>3</sup>	42.2	6.2
$\beta_5$	/-	1.4 10 <sup>2</sup>	18.6	2.7 10 <sup>3</sup>	-30	-3.3
$\beta_6$	/-	-58.1	-3.0 10 <sup>2</sup>	-1.4 10 <sup>3</sup>	-1.0 10 <sup>3</sup>	-56.8
$\beta_7$	/-	65.6	3.2 10 <sup>2</sup>	67.4	1.0 10 <sup>3</sup>	72.1

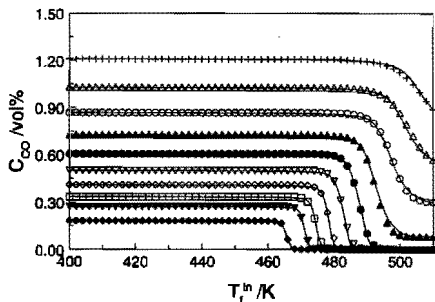


**Figure 7.18**  
**Steady state CO outlet concentrations of the process (full line) and the model (symbols) versus feed temperature.**  
 Parameter  $\lambda$ : + :0.95;  $\Delta$ : 0.96;  $\circ$ : 0.97;  $\blacktriangle$ : 0.98;  $\bullet$ : 0.99;  $\nabla$ : 1;  $\diamond$ : 1.01;  $\square$ : 1.02;  $\blacktriangledown$ : 1.03;  $\blacklozenge$ : 1.05.

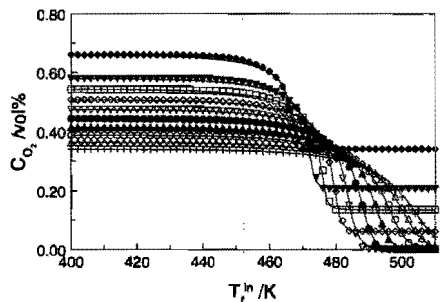


**Figure 7.19**  
**Steady state O<sub>2</sub> outlet concentrations of the process (full line) and the model (symbols) versus feed temperature.**  
 Legend see Figure 7.18.

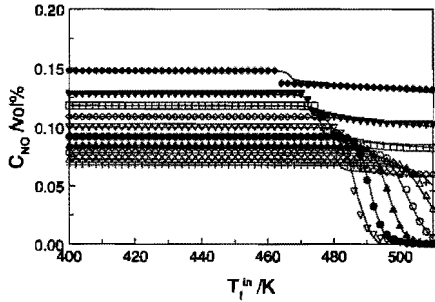


**Figure 7.20**  
**Steady state NO outlet concentrations of the process (full line) and the model (symbols) versus feed temperature.**  
 Legend see Figure 7.18.

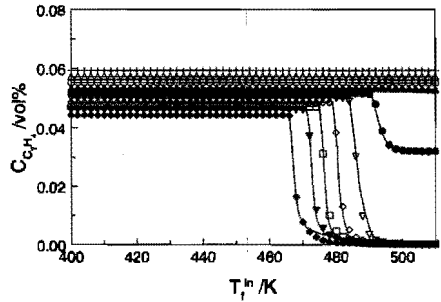


**Figure 7.21**  
**Steady state C<sub>2</sub>H<sub>4</sub> outlet concentrations of the process (full line) and the model (symbols) versus feed temperature.**  
 Legend see Figure 7.18.

The nonlinear behaviour of the oxygen outlet concentration as a function of  $\lambda$  and  $T_i$  is transformed to two new variables  $\lambda^{\text{out}}$  and  $T_i^{\text{out}}$  (see Figure 7.17) using Equations 7.3 to 7.8. The linear models 1 and 2 will be obtained by the identification procedure and they account for the linearized dynamic behaviour of the O<sub>2</sub> outlet concentration as

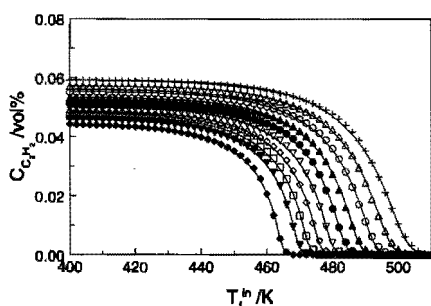


**Figure 7.22**  
**Steady state  $C_{C_2H_2}$  outlet concentrations**  
**of the process (full line) and the model**  
**(symbols) versus feed temperature.**  
 Legend see Figure 7.18.

a function of either  $\lambda^{in}$  or  $T_f^{in}$ . In the controller design  $\lambda^{out}$  will be the CV, whereas the corresponding outlet concentrations are calculated using Equations 7.3 to 7.8. It is allowed to control  $\lambda^{out}$  instead of the  $O_2$  outlet concentration as the concentration is a function of  $\lambda^{out}$ , see also Figure 7.23.  $T_f^{out}$  is an internal variable of the model accounting for the warming up dynamics of the reactor.

The influence of the feed temperature on the dynamic behaviour of  $\lambda^{out}$  is not accounted for in linear model 1; all linearizing calculations are performed at a typical feed temperature of 480 K. Since the oxygen outlet concentration as a function of  $\lambda$  is not a monotonous function, see Figure 7.23, no inverse of this function exists, and hence the calculation of  $\lambda^{out}$  from the oxygen concentration is not straightforward.  $\lambda^{out}$  is calculated by least square regression of the nonlinear process data with Equations 7.3 to 7.8. The corresponding values of  $\lambda^{in}$  are used as initial values in the regression.  $T_f^{out}$  is calculated using the inverse function of Equations 7.3 to 7.8 where  $\lambda$  equals one. This inverse function is obtained by interpolation of  $\lambda^{out}$  at given  $O_2$  outlet concentrations by means of routine E01BEF (NAG, 1995). The staircase oxygen concentration depicted in Figures 7.8 and 7.13 is

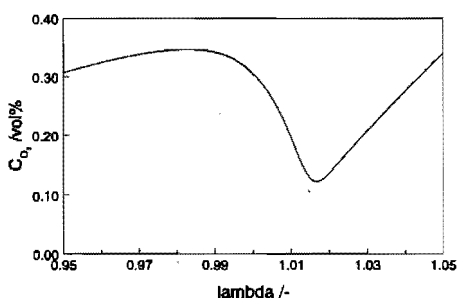


**Figure 7.23**  
 **$O_2$  outlet concentration versus  $\lambda$**   
**calculated using Eq. 7.3 to 7.8.**  
 $T_f = 480$  K.

used to calculate  $\lambda^{\text{out}}$  and  $T_i^{\text{out}}$  as a function of time. This data is used in the identification procedure.

### 7.5.3 Model estimation and validation

The purpose of the identification is to obtain dynamic models which describe both the manipulated and the feed forward variable dependence of the controlled variable. The calculated outputs using the identification model, the inputs and the linearized outputs are depicted in Figures 7.24 and 7.25. From Figure 7.24 it is clear that  $\lambda^{\text{out}}$  still exhibits some nonlinear behaviour and this explains the discrepancy between the linear model and the process. The nonlinearity is probably caused by nonlinear dynamic behaviour of the occurring reactions. However, the delay time and the overall relaxation behaviour are described adequately.

As shown in Figure 7.25, linear model 2 describes the response of  $T_i^{\text{out}}$  very well. The linear behaviour of  $T_i^{\text{out}}$  can be explained assuming steady state surface species and hence steady state reaction rates. The dynamic behaviour of the outlet concentration is then almost completely determined by the heat capacity of the monolith and the rate of energy transfer from the gas phase to the solid phase. Since the inverse steady state behaviour is used to linearize the output the dynamic behaviour of  $T_i^{\text{out}}$  will be linear as well.

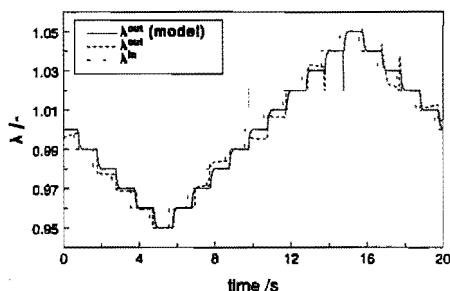


**Figure 7.24**  
 $\lambda^{\text{in}}, \lambda^{\text{out}}$  (process and linear model 1)  
versus time.  $T_i = 480$  K.

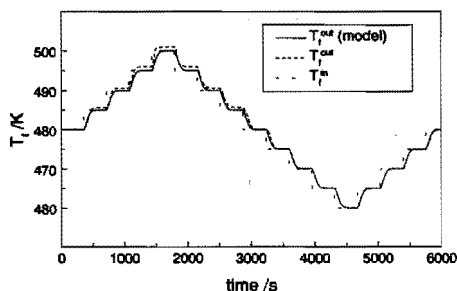


**Figure 7.25**  
 $T_i^{\text{in}}, T_i^{\text{out}}$  (process and linear model 2)  
versus time.  $\lambda = 1$ .

### 7.6 Controller design and performance

In this section a MPC controller for the exhaust gas converter is designed. To demonstrate the benefits of the MPC the performance will be compared with the

performance of a proportional - integral (PI) controller. Most often a PI controller is applied to control the air-to-fuel ratio of the mixture fed to the gasoline engine of cars. As mentioned before, the models resulting from the identification contain all relevant features of the real process such as the delay time and the same dynamic behaviour and therefore it is allowed to use them as the process to be controlled instead of the rigorous model. Once again it should be noted that there is only one MV,  $\lambda^{\text{in}}$ , and one CV,  $\lambda^{\text{out}}$ , which is in line with real exhaust gas conversion. All calculations are performed in Matlab (Mathworks, 1992), a software package especially developed for control applications and signal analysis.

### 7.6.1 PI controller

A discrete PI controller calculates the value  $u$  of the MV at time  $kT_s$  (see also Figure 7.1) using:

$$u(kT_s) = K_p e(kT_s) + \frac{T_s}{T_i} \sum_{m=0}^k e(mT_s) \quad (7.9)$$

where  $T_s$  is the sampling period and  $e(j)$  the deviation from the setpoint at  $t = j$  seconds. The proportional gain  $K_p$  and the integration time  $\tau_i$  are the tuning parameters of the controller. Most often such a controller is tuned by 'trial and error'; the test signal is usually a step change of the setpoint. The final closed loop response is a tradeoff between time to reach a new steady state and the overshoot. Large values of  $K_p$  and/or small values of  $\tau_i$  lead to a more aggressive control action and more overshoot. When tuning the controller the integration time  $\tau_i$  is initially set to a very high value. By increasing  $K_p$  until the response to the step change of the setpoint does not show any overshoot the value of the proportional gain is determined. Next  $\tau_i$  is decreased until the step response exhibits an acceptable overshoot. As the integral action of the controller causes the manipulated variable to change as long as an error exists in the process output, such a controller can eliminate even small errors. However, in case of large delay times a conventional (PI) controller will not act properly to disturbances and setpoint changes. For more details about applications

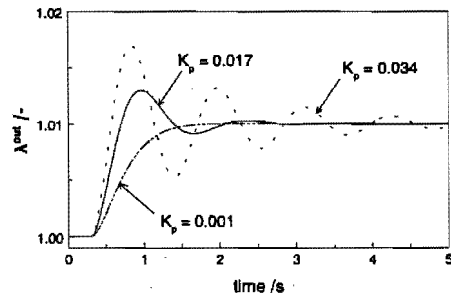


**Figure 7.26**  
Responses of the closed loop system with PI controller at three values of the proportional gain  $K_p$  due to step change of the setpoint.  $\tau_i = 0.7$  s.

of PI controllers in combination with chemical processes see Stephanopoulos (1984).

In Figure 7.26 the closed loop step response for three values of  $K_p$  is shown. The behaviour as a function of  $\tau_i^{-1}$  is similar. As can be seen from this figure, a value of 0.034 leads to oscillatory behaviour of  $\lambda^{out}$ , while a value of 0.001 results in slow relaxation behaviour. In the example discussed in this section  $K_p$  is set to 0.017 and  $\tau_i$  to 0.7 s. A large overshoot is accepted (see Figure 7.26) to ensure a relatively fast response of the closed loop system to setpoint changes and disturbances.

## 7.6.2 Model predictive controller

The behaviour of the process with MPC is calculated using routine SCMPC from the Matlab MPC toolbox (Morari and Ricker, 1994). Tuning parameters of the controller

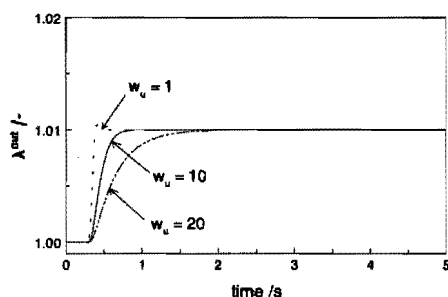


**Figure 7.27**  
**Response of the closed loop system with MPC at three values of the weights  $w_u$  due to step change of the setpoint. Prediction horizon: 0.5 s; control horizon: 0.25 s.**

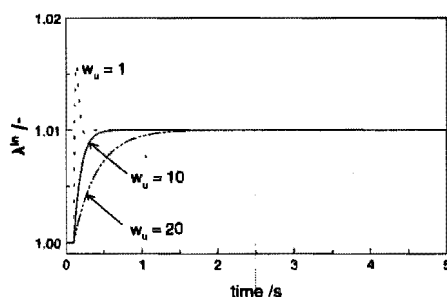


**Figure 7.28**  
**Manipulated variable  $\lambda^u$  of the closed loop system with MPC at three values of the weights  $w_u$  due to step change of the setpoint. Prediction horizon: 0.5 s; control horizon: 0.25 s.**

are the length of the prediction horizon, the numbers of control moves within one control cycle (see Figure 7.3), and the weights of the control moves. The latter limit the absolute values of the changes of the MV, see also Equation 7.1. Once again the response to a step change of the setpoint is used to determine the controller parameters by a 'trial and error' method. To allow the prediction to reach the steady state the prediction horizon should be longer than the largest time constant of the process ( $\tau = 0.4$  s). When the prediction horizon is too short the controller cannot correct for the last part of the response, which may lead to instabilities. Therefore, the prediction horizon is set to 0.5 s. The control horizon gives the number of moves the controller implements to reach the new setpoint, see also Figure 7.3, and is always

shorter than the prediction horizon. Small ratios of control horizon to prediction horizon result in a more aggressive control action, as the controller tries to move the CV to the setpoint within a shorter period of time. The control horizon is set to 0.25 s. In Figure 7.27 the step response at three values of the weight is depicted. A weight of 10 is chosen in the final tuning to obtain a compromise between a fast responding system and a not too aggressive control action, see Figure 7.28.

### 7.6.3 Comparison between the PI controller and the MPC

To demonstrate the advantages of a model predictive controller the response to a step setpoint change is compared with the response of the PI controller. In Figures 7.29 to 7.31 respectively the MV, CV and the  $O_2$  outlet concentration, are depicted for both the PI controller and MPC. As can be seen from Figure 7.29, the MPC control action is more aggressive than the PI control action. The PI controller cannot be tuned more aggressively since the delay time of the process leads to oscillatory behaviour of the closed loop system for large values of  $K_p$  and/or small values of  $\tau_i$ , see Figure 7.26. Since the MPC calculates the response to a setpoint change using its internal model it does not have to wait until the CV changes as in case of the PI controller. The latter uses the error between the setpoint and the CV to determine the moves of the MV, and hence can only respond adequately after detecting the process response. Compared to the PI-controller the MPC based system reaches the setpoint within a much shorter period of time and without overshoot (Figure 7.30). Due to the delay time the control actions of the PI controller lead to a damped oscillatory response of the CV. This is line with the behaviour of a real exhaust control system as reported in the literature (Taylor

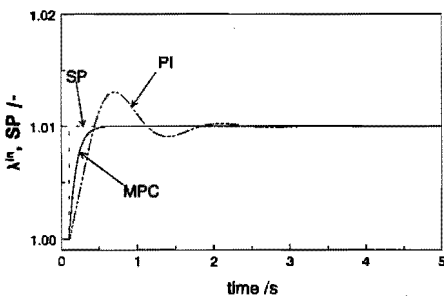


**Figure 7.29**  
*Manipulated variable  $\lambda^{in}$  for the closed loop system with MPC and PI controller due to step change of the setpoint.*

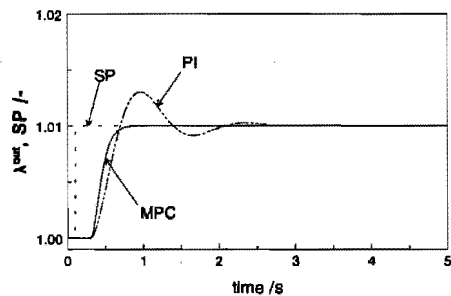


**Figure 7.30**  
*Responses of the closed loop system with MPC and PI controller due to step change of the setpoint.*

and Sinkevitch, 1983).

From these figures it is clear that the MPC keeps the CV close to the setpoint. This means that oscillations can be induced with an optimal frequency to increase the performance of the reactor as described in Chapter 6 of this thesis. In Figure 7.31 the  $O_2$  outlet concentration calculated using Equations 7.3 to 7.8 is shown after a step change of the setpoint. The outlet concentrations of CO, NO  $C_2H_4$  and  $C_2H_2$  show similar behaviour.

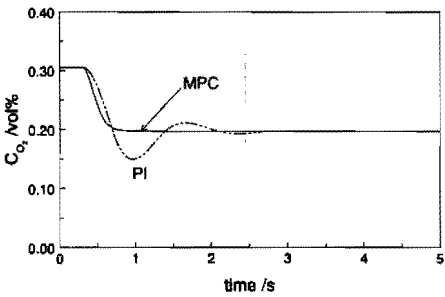


**Figure 7.31**  
*Responses of the  $O_2$  concentration of the closed loop system with MPC and PI controller due to step change of the setpoint.*

**7.6.4 Effects of model error on the performance of the MPC**

In the MPC design discussed in section 7.6.2 the controlled process and the internal model were the same and hence there is no model error. To show the effects of model errors on the performance of the MPC the steady state gain of the internal

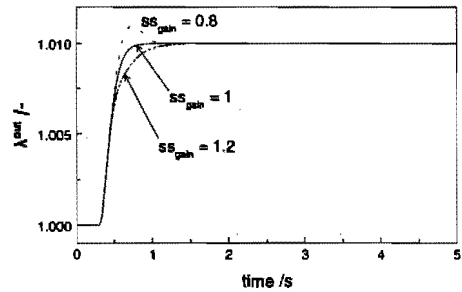


**Figure 7.32**  
*Effects of model error on the step response of a closed loop system with a MPC.*

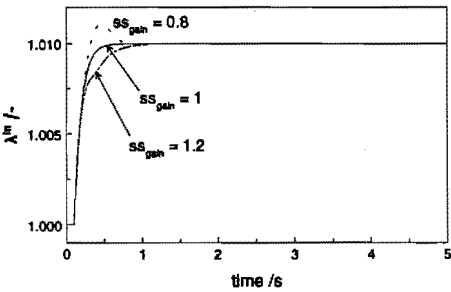


**Figure 7.33**  
*Effects of model error on the manipulated variable of a closed loop system with a MPC.*

model of the controller is changed  $\pm 20\%$  and the response of the closed loop system is compared with the response without modelling error. As shown in Figure 7.32, the performance of the MPC decreases by the introduction of the model error. However,



the time to steady state is still much shorter than the response of the closed loop system with the PI controller, see Figure 7.30. When the steady state gain of the internal model is smaller than the gain of the process, the calculated value of  $\lambda^{\text{in}}$  to reach the setpoint using the internal model is too large and consequently the value of controlled variable  $\lambda^{\text{out}}$  becomes too high. The correction by the feedback loop takes place after detecting the increasing CV and this leads to a lower performance, see Figure 7.33. When the gain of the model is larger than the process gain the calculated MV value is too small and the CV will not reach the setpoint. After the delay time the value of the MV is adapted and the output error becomes zero.

### 7.7 Steady state optimizer

The nonlinear steady state model given by Equations 7.3 to 7.8 is used to calculate the optimal setpoints of  $\lambda^{\text{out}}$  at a given temperature  $T_i^{\text{out}}$  by weighted quadratic minimization of the outlet concentrations of the pollutants with respect to the parameter  $\lambda^{\text{out}}$ . The weights  $w_i$  for component  $i$  are chosen to obtain an equal contribution of all pollutants CO, NO and hydrocarbons in the objective function. Since the CO concentration in the feed of the converter is about 10 times the concentration of NO and hydrocarbons ( $\text{C}_2\text{H}_4$  plus  $\text{C}_2\text{H}_2$ ) see Figure 7.5, the weights are set to:  $w_{\text{CO}} = 1$ ,  $w_{\text{NO}} = 10$  and  $w_{\text{HC}} = 10$ .

A cold start is simulated by inducing a step increase of  $T_i^{\text{in}}$  from 400 to 500 K. The optimal steady state setpoints of  $\lambda^{\text{out}}$  are calculated every second and sent to the MPC. Figure 7.34 shows the optimal setpoints as a function of time. The feed forward setpoints, based on the feed forward signals of the currently applied control system, are shown as well. These are constructed using the following assumption: When the engine's temperature is relatively low it is running on a rich mixture ( $\lambda < 1$ ). At a higher temperature the air-to-fuel ratio is increased to obtain the stoichiometric value at an elevated temperature. As shown in this figure the optimal air-to-fuel ratio fed to the engine is switched from rich to lean at  $t = 45$  s. This causes the oxidation reactions to proceed at a higher reaction rate leading to fast decreasing outlet concentrations of both CO and hydrocarbons, see also Figure 7.35. When comparing the outlet concentrations with feed forward and optimizer setpoints, Figures 7.35 and

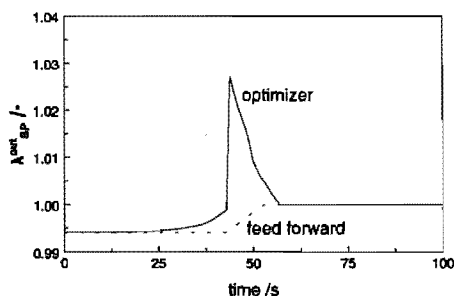


**Figure 7.34**  
*Optimal setpoints and the feed forward setpoints of  $\lambda^{\text{out}}$  versus time after a step change of  $T_i^{\text{in}}$  from 400 to 500 K.*

7.36, it is clear that switching the air-fuel mixture to lean for a short period ignites all oxidation reactions simultaneously whereas in case of the feed forward signal the pollutants are converted in the same sequence as discussed in Chapter 6. The reduction of NO proceeds at a relatively low rate for  $t > 45$  s since the reducing components are almost completely converted.

The performance improvement due to the optimizer is calculated by integrating the outlet concentrations in time and comparing the cumulative emissions of the pollutants in both cases. For CO and  $C_2H_4$  the relative improvement equals 15%, for  $C_2H_2$  5% and for NO 1%.

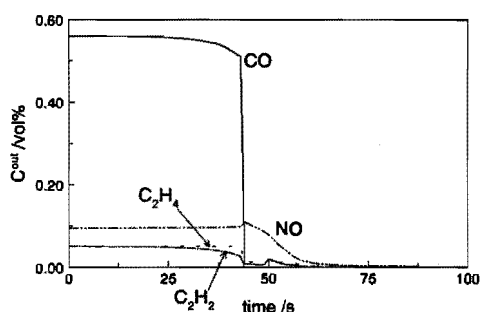


**Figure 7.35**  
Outlet concentrations versus time when applying the optimal setpoints after a step change of  $T_i^n$  from 400 to 500 K.

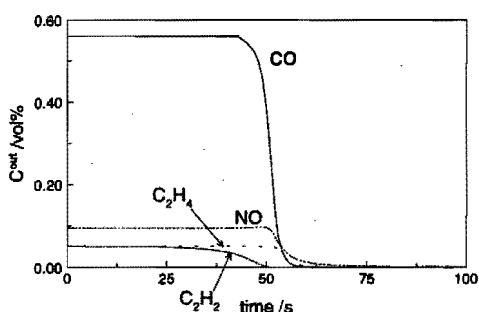


**Figure 7.36**  
Outlet concentrations versus time when applying the feed forward setpoints after a step change of  $T_i^n$  from 400 to 500 K.

## 7.8 Conclusions

In developing a model based controller of the exhaust gas converter nonlinear transformations can be applied to account for the nonlinear behaviour of the process. A linear model can then be used to control the process over a broad range of operating conditions in spite of the nonlinear behaviour.

The closed loop behaviour of the engine plus the exhaust gas converter in combination with a model based controller leads to a fast responding system to setpoint changes without causing any overshoot. A PI controller based system introduces oscillations as a result of the delay time present in the feedback loop. However, to obtain a fast responding closed loop behaviour to setpoint changes the internal model of the controller must describe the process adequately. But, a model error of 20% still leads to higher performance than a PI controller.

The steady state model of the converter can be used to calculate the optimal setpoints of the air-to-fuel ratio during a cold-start. By switching the feed mixture of the engine from rich to lean for a short period only, all oxidation reactions ignite simultaneously leading to lower emissions of the pollutants.

## References

- Backx, A.C.P.M., Identification of an industrial process: A Markov parameter approach, Ph.D. Thesis, Eindhoven University of Technology, 1987
- Backx, A.C.P.M., Damen, A.A.H., Identification of industrial MIMO processes for fixed controllers, Part 1 General theory and practice, *Journal A* **30**, 3-12, 1989
- Beck, D.D., Sommers, J.W., Impact of sulfur on three-way catalysts: comparison of commercially produced Pd and Pt-Rh monoliths, *Preprints of the Third International Congress on Catalysis and Automotive Pollution Control (CaPoC3)*, 147-159, 1994.
- Garcia, C.E., Pretti, D.M., Morari, M., Model predictive control: Theory and practice - a survey, *Automatica* **25(3)**, 335-348, 1989
- Ljung, L., System identification: Theory for the user, Prentice-Hall Information and system sciences series, 1987
- Matlab, High performance numeric computation and visualization software, Reference Guide, The Mathworks, 1992
- Morari, M., Ricker, N.L., Model predictive control toolbox, The Mathworks Inc., 1994
- Muske, K.R., Rawlings, J.B., Model predictive control with linear models, *AIChE J.*, **39(2)**, 262-287, 1993
- NAG Fortran Library Manual, mark 16, volume 1, 1995
- Oh, S.H., Bissett, E.J., Battison, P.A., Mathematical modeling of electrically heated monolith converters: Model formulation, numerical methods, and experimental verification, *Ind. Eng. Chem. Res.* **32**, 1560-1567, 1993
- Richalet, J., Rault, A., Testud, J.L., Papon, J., Model predictive heuristic control: Applications to industrial processes, *Automatica* **14**, 413-428, 1978
- Richalet, J., Industrial applications of model based predictive control, *Automatica*, **29(5)**, 1251-1274, 1993
- Stephanopoulos, G., Chemical process control: An introduction to theory and practice, Prentice-Hall International Editions, 1984
- Taylor, K.C., Sinkevitch, R.M., Behaviour of automotive exhaust catalyst with cyclic feed streams, *Ind. Eng. Chem. Prod. Res. Dev.* **22**, 45-51, 1983.
- Taylor, K.C., Nitric oxide catalysis in automotive exhaust systems, *Catal. Rev.-Sci. Eng.* **35(4)** 457-481, 1994



# 8

---

## GENERAL CONCLUSIONS

The work presented in this thesis focused on the transient kinetics of the catalytic oxidation of CO over supported platinum catalysts. Cyclic feeding experiments were carried out under conditions relevant for exhaust gas treatment in practice. Furthermore, the effects of cyclic feeding on the performance of the converter used for exhaust gas treatment were investigated and a model based controller of the converter was developed.

A frequency response analysis with respect to continuous flow reactors showed that cyclic reactor operation reveals more kinetic information than steady state operation. Due to the absence of mixing in the fluid phase the outlet concentration of a plug flow reactor contains more kinetic information than that of a continuous stirred tank reactor.

From cyclic feeding experiments with a Pt/ $\gamma$ -Al<sub>2</sub>O<sub>3</sub> catalyst it was found that O<sub>2</sub> adsorption is strongly inhibited by adsorbed CO. An elementary step model based on the assumption that molecular adsorption of oxygen is followed by instantaneous dissociation describes adequately the responses as a result of admitting oxygen to a CO covered catalytic surface. In contrast, CO was found to adsorb on a catalytic surface completely covered with oxygen adatoms. In order to describe the experimental data after admission of CO to an oxygen covered surface, CO adsorption on a catalytic site already occupied by an oxygen adatom was assumed. The experimentally found interaction of CO<sub>2</sub> with the support was accounted for by reversible adsorption. All kinetic parameters of the elementary step kinetic model were determined by means of nonlinear regression.

Cyclic feeding experiments using a commercial Pt/Rh/CeO<sub>2</sub>/ $\gamma$ -Al<sub>2</sub>O<sub>3</sub> catalyst suggest the existence of an another route converting CO into CO<sub>2</sub>: the bifunctional path.

Here oxygen on the ceria surface reacts with CO adsorbed on the metal-ceria interface. From the experiments it was also found that ceria acts as a storage component releasing oxygen under net reducing conditions and filling up with oxygen under net oxidizing conditions. Oxygen from the ceria bulk is involved in the reaction at higher temperatures only. The oxygen supplied by ceria leads to a higher time-average CO conversion compared to a Pt/ $\gamma$ - $\text{Al}_2\text{O}_3$  catalyst. Steam was found to enhance the  $\text{CO}_2$  production rate, whereas the presence of  $\text{CO}_2$  in the feed stream leads to a less pronounced contribution of the bifunctional path to the  $\text{CO}_2$  formation by blocking adsorption sites on the ceria surface. Based on the experimental results an elementary step reaction mechanism was introduced taking into account this bifunctional path.

In order to study the effects of cyclic feeding on the performance of a catalytic converter applied in exhaust gas treatment an adiabatic model considering the reduction of NO and the oxidation of CO,  $\text{C}_2\text{H}_4$  and  $\text{C}_2\text{H}_2$  by  $\text{O}_2$  was used. The simulations demonstrate that cyclic feeding leads to higher time-average conversions compared to the steady state conversions. However, the improved performance is a strong function of the operating conditions. Below the light-off temperature cyclic feeding leads to higher time-average conversions, while above the light-off temperature steady state operation leads to the highest reactor performance. Steady state simulations show that the pollutants are converted in the reactor in a fixed sequence: first ethyne, then carbon monoxide, and finally nitrogen oxide and ethene simultaneously.

A black-box model was developed for the combination of the engine and the converter. For the engine a model published in the literature was used, while for the converter the model developed in this study was utilized. The black-box model was used in a model predictive controller scheme. Since this controller is based on a linear model the nonlinear process behaviour was linearized by means of nonlinear transformations. The performance of the model predictive controller was compared with the performance of the usually applied proportional - integral controller. The model predictive controller enables a fast reacting closed loop response to setpoint changes without causing any overshoot, whereas the proportional - integral controller leads to oscillatory behaviour of the closed loop system. A steady state optimizer was used to calculate the optimal air-to-fuel ratio of the mixture fed to the engine during a cold-start. At low converter temperatures a slightly rich feed of the engine leads to the lowest emissions. Switching the feed of the engine to lean for a short period of time only is sufficient to ignite the oxidation reaction simultaneously leading to a reduction of the emissions of the pollutants.

---

## **DANKWOORD**

In tegenstelling tot de omslag doet vermoeden, is dit proefschrift niet het werk van één persoon. Ik wil dan ook iedereen die aan de totstandkoming hiervan heeft meegewerkt hartelijk danken.





---

## **CURRICULUM VITAE**

Arthur Nievergeld werd op 20 oktober 1964 geboren te Kelpen. In 1983 heeft hij het VWO diploma aan de Scholengemeenschap Sint Ursula te Horn gehaald. Hierna studeerde hij gedurende een jaar Werktuigbouwkunde aan de Technische Universiteit Eindhoven. In 1984 begon hij de studie Elektrotechniek aan dezelfde universiteit die in 1990 werd afgerond met een afstudeeronderwerp onder leiding van prof. ir. Kylstra. In 1992 begon hij met de Korte Onderzoekopleiding Scheikundige Technologie van het Instituut Vervolgopleidingen-TUE. Na afronding van deze opleiding in 1994 is hij met het promotieonderzoek begonnen in de groep van prof.dr.ir. G.B. Marin dat heeft geleid tot dit proefschrift. In januari 1997 is hij in dienst getreden van AspenTech Benelux b.v.



## Stellingen

Behorende bij het proefschrift

### **Automotive Exhaust Gas Conversion: Reaction Kinetics, Reactor Modelling and Control**

van Arthur Nievergeld

1. Indien Lynch en Graham tijdens hun transiënt kinetisch onderzoek een propstroomreactor hadden gebruikt in plaats van een CSTR, dan had hun kinetisch model er anders uitgezien.

Lynch D.T., Graham W.R.C., *AIChE* **36**, 1797-1806, 1990;

Hoofdstuk 3 van dit proefschrift.

2. Aangezien Cutlib *et al.* voor de beschrijving van hun dynamische experimenten een kinetisch model gebruiken dat is gebaseerd op de beschrijving van de CO oxidatie in het CO inhibitiegebied, is het voorspelde stationaire gedrag niet in overeenstemming met eerder gedane observaties.

Cutlib M.B., Hawkins C.J., Mukesh D., Morton W., Kenney C.N., *Chem. Eng. Commun.* **22**, 329-344, 1983;

Hoofdstuk 4 van dit proefschrift.

3. Door de wederzijdse beïnvloeding van schadelijke componenten in het uitlaatgas van benzinemotoren is voor een realistische simulatie een vrijwel complete uitlaatgassamenstelling noodzakelijk.

Hoofdstuk 6 van dit proefschrift.

4. De verklaring van Silveston dat de positieve effecten op de prestatie van een propstroomreactor met een oscillerende voedingssamenstelling afnemen met toenemende tijdgemiddelde CO conversie door een afname van de CO amplitude, is niet juist.

Silveston P.L., *Catal. Today* **25**, 175-195, 1995;

Hoofdstuk 6 van dit proefschrift.

5. Onderzoekers die een stationair kinetisch model gebruiken voor de simulatie van een drie-wegkatalysator met een oscillerende voedingssamenstelling, moeten het woord 'transiënt' weglaten uit de titel van hun artikel.

6. De straffen die een schuldige krijgt opgelegd zijn doorgaans minder zwaar dan de straffen op overtreding van de wetten die hem/haar beschermen.

7. Tegenwoordig is in de file staan niet meer zo erg, want je weet vrijwel zeker dat de reizigers met het openbaar vervoer nog later thuis zijn.
8. Het juist gebruik van de grammaticacontrole van een tekstverwerker vereist een behoorlijke kennis van grammatica.  
Onze Taal, 11, 1997.
9. De rechtvaardiging naar de buitenwereld, dat de overname van een bedrijf noodzakelijk is om tot de top twee te horen is vaak een kwestie van het juist definiëren van de markt; de werkelijke reden wordt echter vaak gevormd door opportunistische directies.
10. Biologische oorlogvoering spitst zich tegenwoordig toe op computers. Het grootste probleem bij het afslaan van een *cyber*-aanval is het beantwoorden van de vraag: Is de aanval een daad van oorlog ?
11. Dit zou een zin uit het Groot Dictee der *Nieuwe* Nederlandse Taal kunnen zijn: De hippo's die na de elandtest bevend naar een pinkelpaal rennen om vervolgens spontaan te stoppen met montignaccen en daardoor gaan jojoën, kunnen het best naar een zotel gaan om met een portie mediwiet tot rust te komen.

hippo's: *high potentials*; jojoën: extreme gewichtsschommelingen door schranspartij; zotel: hotel met *low care* medische voorzieningen; mediwiet: marihuana verstrekt op medische indicatie.